Probing weak ergodicity breaking in the one-dimensional Fermi-Hubbard model

Thomas Kohlert

SIGILL. UNIVERSITAT. LUDOVIC. MAXIM.

München 2021

Probing weak ergodicity breaking in the one-dimensional Fermi-Hubbard model

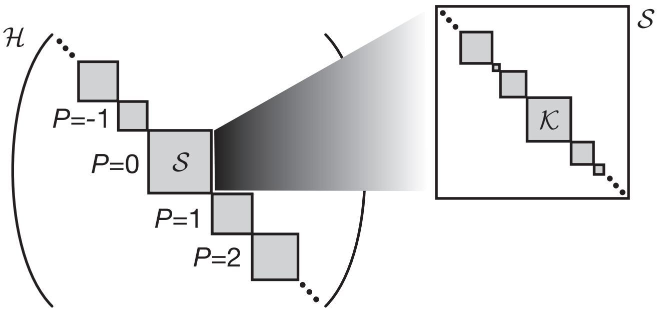

Dissertation an der Fakultät für Physik
Ludwig-Maximilians-Universität München

vorgelegt von

Thomas Kohlert

aus Gräfelfing

München, den 18. Mai 2021

Tag der mündlichen Prüfung: 30. Juni 2021
Erstgutachter: Prof. Immanuel Bloch
Zweitgutachter: Prof. Michael Knap
Weitere Prüfungskommissionsmitglieder: Prof. Thomas Udem und Prof. Jan Lipfert

Zusammenfassung

Wir benutzen einen analogen Quantensimulator mit ultrakalten fermionischen ^{40}K-Atomen in einem eindimensionalen optischen Gitter, um die Dynamik eines Anfangszustandes fernab des Gleichgewichts zu untersuchen. Während sich generische abgeschlossene Quantensysteme ergodisch verhalten und ihr thermisches Gleichgewicht erreichen - eine Vorhersage der Hypothese der Eigenzustandsthermalisierung - gibt es bekannte Ausnahmen von diesem Grundsatz. Insbesondere Integrabilität und Vielteilchenlokalisierung führen zu nicht-thermischem Verhalten aufgrund einer extensiven Zahl von Erhaltungsgrößen. Zuletzt sind hingegen weitere Systeme in den wissenschaftlichen Fokus gerückt, die weder eindeutig als thermisch noch als integrabel klassifiziert und typischerweise als schwach ergodizitätsverletzend zusammengefasst werden können. In dieser Doktorarbeit betrachten wir mit Vielteilchen-Mobilitätskanten und Hilbertraumfragmentierung zwei Vertreter dieser neuen Klassen von der experimentellen Seite und unterstützen die Ergebnisse mit komplementären theoretischen Resultaten.

Im ersten Projekt realisieren wir ein Gittermodell mit quasiperiodischer Unordnung und einer Einteilchen-Mobilitätskante. Dieses nicht-wechselwirkende System können wir dadurch in einer Koexistenz aus lokalisierten und ausgedehnten Zuständen präparieren. Die Einführung lokaler Wechselwirkungen motiviert in diesem Kontext zwei zentrale Fragen, die Gegenstand aktueller theoretischer Debatten sind: Kann Vielteilchenlokalisierung in einem System mit einer Mobilitätskante überhaupt vorkommen? Existiert dazwischen eine neue Vielteilchenphase, die durch eine Koexistenz lokalisierter und ausgedehnter Vielteilchenzustände definiert ist? In dieser Arbeit demonstrieren wir Vielteilchenlokalisierung in einem Parameterbereich, in dem alle zugehörigen Einteilchenzustände lokalisiert sind. Weiterhin beobachten wir, dass nicht-lokalisierte Zustände nicht zu einer beschleunigten Relaxation des Systems hin zu einem thermischen Zustand führen und somit kein effizientes Bad darstellen. Dies schließt die Möglichkeit einer neuen (intermediären) Vielteilchenphase nicht explizit aus.

Das zweite Projekt untersucht das eindimensionale Fermi-Hubbard-Modell in der Gegenwart eines starken linearen externen Potentials, des sogenannten Tilts. Dieses Modell dient als ideales Versuchsfeld, um die Physik fragmentierter Hilberträume zu untersuchen. Dabei handelt es sich um einen neu entdeckten Mechanismus, der in der Gegenwart nur weniger Erhaltungsgrößen zu nicht-thermischen Eigenschaften führt. Wir untersuchen die Dynamik verschiedener Anfangszustände, die sich durch den Anteil doppelt besetzter Gitterplätze unterscheiden. Dabei kommen neue experimentelle Methoden zur Charakterisierung des Anfangszustands mittels Mikrowellenspektroskopie und zur Kontrolle des spinabhängigen Tilts durch Radiofrequenz-Dressing zum Einsatz. Wir beobachten eine starke Abhängigkeit der Dynamik von den jeweiligen Anfangsbedingungen, was ein charakteristisches Merkmal schwacher Ergodizitätsverletzung darstellt. Zusammen mit numerischen Simulationen des effektiven Hamiltonians führender Ordnung in Störungstheorie können wir Beweise liefern, dass unsere experimentellen Befunde mit dieser effektiven Beschreibung übereinstimmen und wir daher ein fragmentiertes Modell in unserem System implementieren können.

Summary

We employ an analog quantum simulator with ultracold fermionic ^{40}K atoms in an optical lattice confined to one dimension to probe the dynamics of a given initial state far from equilibrium. While generic closed quantum systems are expected to behave ergodically and thus reach thermal equilibrium as predicted by the eigenstate thermalization hypothesis, there are well-known exceptions to this paradigm. Above all, integrability and many-body localization avoid thermalization through an extensive set of conserved quantities. However, recently new types of systems that can neither be classified uniquely as thermal or integrable and that are commonly summarized as weakly ergodicity breaking, attracted considerable interest. In this thesis we investigate two such classes, mobility edges and Hilbert space fragmentation, experimentally and support our findings with complementary theoretical insights.

In the first project we realize a lattice model with quasiperiodic on-site detuning with a single-particle mobility edge such that the non-interacting system can be prepared in a coexistence of localized and extended eigenstates. Upon the addition of local interactions two central questions that are in the focus of a current theoretical debate, arise: Does many-body localization occur in the presence of a single-particle mobility edge? Does a many-body intermediate phase characterized by a coexistence of localized and extended many-body states emerge? In our work we establish the existence of many-body localization in such a model in a regime where all single-particle states are localized. Further, we observe that the presence of extended states does not lead to a faster relaxation of the system to a thermal ensemble such that extended many-body states do not serve as an efficient heat bath. This does not explicitly exclude the existence of a many-body intermediate phase.

The second project is dedicated to the one-dimensional Fermi-Hubbard model in the presence of a strong linear external potential, the so-called tilt. This model is the ideal setting to probe the physics of Hilbert space fragmentation, a recently discovered mechanism that avoids thermalization with only few conserved quantities. We probe the dynamics of various initial states that differ by the fraction of doubly occupied sites. Herein we employ new experimental methods to characterize the initial state by means of microwave spectroscopy and to tune the spin-dependent tilt via radio-frequency dressing. We observe a strong dependence on the initial conditions, a characteristic property of weakly ergodicity-breaking systems. Together with numerical simulations of a leading-order effective Hamiltonian we can provide evidence that our experimental observations are in agreement with this effective description such that we can indeed implement a fragmented model in our system.

Publications

These projects reported in this theses were published in the following papers:

- **Thomas Kohlert**, Sebastian Scherg, Xiao Li, Henrik P. Lüschen, Sankar Das Sarma, Immanuel Bloch, Monika Aidelsburger. "Observation of Many-Body Localization in a One-Dimensional System with a Single-Particle Mobility Edge", *Phys. Rev. Lett.* **122**, 170403 (2019).
- **Thomas Kohlert**, Sebastian Scherg, Pablo Sala, Frank Pollmann, Bharath Hebbe Madhusudhana, Immanuel Bloch, Monika Aidelsburger. "Experimental realization of fragmented models in tilted Fermi-Hubbard chains", *arXiv:2106.15586* (2021)

Moreover, during the course of my PhD I contributed to the following publications which are partially covered in this thesis as they contain important concepts used in this work:

- Henrik P. Lüschen, Sebastian Scherg, **Thomas Kohlert**, Michael Schreiber, Pranjal Bordia, Xiao Li, Sankar Das Sarma, Immanuel Bloch. "Single-Particle Mobility Edge in a One-Dimensional Quasiperiodic Optical Lattice", *Phys. Rev. Lett.* **120**, 160404 (2018).
- Sebastian Scherg, **Thomas Kohlert**, Pablo Sala, Frank Pollmann, Bharath Hebbe Madhusudhana, Immanuel Bloch, Monika Aidelsburger. "Observing non-ergodicity due to kinetic constraints in tilted Fermi Hubbard chains", *arXiv:2010.12965* (2020)
- Bharath Hebbe Madhusudhana, Sebastian Scherg, **Thomas Kohlert**, Immanuel Bloch, Monika Aidelsburger. "Benchmarking a novel efficient numerical method for localized 1D Fermi-Hubbard systems on a quantum simulator", *arXiv:2105.06372* (2021)

Finally, I contributed to a publication which is not covered in this thesis:

- Sebastian Scherg, **Thomas Kohlert**, Jacek Herbrych, Jan Stolpp, Pranjal Bordia, Ulrich Schneider, Fabian Heidrich-Meisner, Immanuel Bloch, Monika Aidelsburger. "Nonequilibrium Mass Transport in the 1D Fermi-Hubbard Model", *Phys. Rev. Lett.* **121**, 130402 (2018).

Contents

List of Figures

Preface

The thermalization of classical systems is believed to be understood in terms of Boltzmann's ergodic hypothesis [1]. It states that during time evolution the system explores the full available phase space as allowed by global conservation laws. The time-averaged expectation value of physical observables is thus given the the microcanonical ensemble average. A quantum system on the other hand, thermalizes through the loss of coherence that has to be erased in the course of the dynamics [2]. This, however, is not obvious since time evolution is unitary and chaotic dynamics that drive thermalization in classical systems cannot occur. Instead, quantum thermalization happens on the level of individual eigenstates as predicted by the famous eigenstate thermalization hypothesis (ETH) [3, 4]. Every eigenstate itself behaves like a thermal ensemble and possesses thermal expectation values for a given physical observable.

Although the ETH is only a hypothesis without available formal proof, it is believed to hold for all thermalizing quantum many-body systems and numerical simulations support this conjecture by reproducing central claims of the ETH [5]. However, providing full evidence for a given system to be thermal is extremely difficult as it would require that every physical observable behaves thermally. While quantum thermalization is a ubiquitous phenomenon, there are few exceptions to this paradigm, which gather a lot of theoretical and experimental interest. The most prominent mechanism to break ergodicity is integrability that comes along with an extensive set of conserved quantities that limit the degrees of freedom and impede thermal dynamics. Integrable systems can be solved with the famous Bethe ansatz [6] and many popular models belong to this class such as the Fermi-Hubbard model [7], the Lieb-Liniger model [8], the antiferromagnetic Heisenberg spin chain [9] or the Anderson impurity model [10]. Integrable models, though, are very fine-tuned and small perturbations like non-local interactions or an external drive are sufficient to restore thermalization. A more robust exception to ETH are randomly disordered systems that feature localized eigenstates due quantum interference [11]. It was shown that this localization can persist forever in the presence of interactions giving rise to the phase of many-body localization (MBL) [12–17]. It is characterized by the absence of particle transport and thus vanishing conductivity [18–20] as well as logarithmically slow entanglement growth [21]. The MBL phase possesses an emergent integrability as the Hamiltonian can be expanded in terms of a complete set of conserved local operators in close analogy to integrable systems [22, 23]. The local integrals of motion (LIOMs) are able to explain the MBL phenomenology. Although the occurrence of localization was first predicted for systems with random disorder, the famous Aubry-André model [24] also features localized eigenstates with a quasiperiodic external potential. Later, numerical works provided evidence that MBL is equally expected there [25]. Due to the experimental relevance of this model localization was soon investigated experimentally in quasiperiodic systems.

Although Anderson's theory was originally formulated for electrons in disordered metals, localization cannot be observed in real solid state systems due to thermal phonons that serve as a heat bath and destroy localization phenomena. It required the development of synthetic systems until Anderson localization was first demonstrated about 60 years after its prediction with light in a disordered waveguide array [26, 27]. In the following, quantum simulators with ultracold atoms in optical lattices proved to be a successful platform, comprising the first demonstration of single-particle [28] and many-body localization [29] in the quasiperiodic Aubry-André model. In the following years MBL was then identified in many other experimental platforms ranging from quantum gas microscopes [30, 31], ion traps [32] and superconducting qubits [33, 34] to nuclear spins [35]. Subsequently, many further questions regarding the properties of the MBL phase attracted the attention of theoretical investigations, accompanied by complementary insights from experimental studies. These include localized systems subject to an external periodic modulation [36–40], the nature of the dynamical transition between the ergodic and localized phase [41–49] and the possibility of MBL in higher dimensions [50–54]. For real-life applications it is a particularly relevant question what happens to an MBL system when it is coupled to a thermal bath. Numerous theoretical studies [55–59] agree that for sufficiently strong coupling to the environment an MBL system restores thermalization and is driven to thermal equilibrium. This was also confirmed in dedicated experiments implementing the coupling to a bath [60, 61]. Along these lines an interesting question to explore is the coupling between localized and extended components as explored in [62]. This situation is different from coupling to a thermal bath due to the comparable number of degrees of freedom in the system and the bath. Those results take on significance when studying the role of many-body mobility edges [12, 63–66] and the resulting coexistence of localized and extended many-body states across the spectrum. The questions whether many-body mobility edges exist and whether MBL prevails in such systems is highly debated [67, 68] and its experimental exploration is part of this thesis.

In recent years the community redeployed interests towards other classes of systems that violate the ETH in the absence of disorder and in particular looked for MBL in disorder-free systems with translational invariance [69–75]. These studies typically identify trapped metastable states with exponentially long-lived localization owing to kinetic constraints due to strong interactions and frustration. In this context one can define a strong and a weak version of ETH: While all eigenstates within the spectrum need to have thermal expectation values in order to satisfy strong ETH, as obeyed by typical ergodic systems, the weak version tolerates a finite number of outlying states as long as their number vanishes in the thermodynamic limit. This distinction was motivated by the discovery of special long-lived initial states in a Rydberg tweezer experiment [76] that led to the theoretical discovery of quantum many-body scars [77–85], non-ergodic eigenstates within a thermal bulk that feature low entanglement and non-ergodic properties. Another important class in the context of weak and strong ergodicity breaking are fractonic systems [86] that exhibit constrained dynamics, either because they are explicitly included in the Hamiltonian or due to conservation laws. For the concrete case of charge and dipole moment conservation it was recently shown that the Hilbert space fragments into exponentially many dynamically disconnected subsectors and thereby provides an efficient method to prevent ergodicty as the dynamics are restricted to an exponentially small sector of the full Hilbert space [81, 87–91]. Consequently, this process is called Hilbert space fragmentation (HSF) and represents a new ergodicity-breaking phenomenon without the need of quenched disorder. This mechanism has to be properly distinguished from conventional MBL and a defining characteristic of HSF is a strong dependence of the dynamics on the initial conditions [87, 88] as opposed to thermal and MBL systems. Such models bear experimental significance as charge and dipole moment conservation naturally occur in the effective description of the Quantum Hall effect [92–94] and tilted lattice models [95, 96]. The latter case of a linearly tilted lattice potential has already been realized in multiple experimental platforms [97–100], although with a different research focus, until recent works discovered MBL-like properties in such a system including harmonic confinement [95] or weak disorder [96]. Thus, this newly discovered phase was dubbed Stark MBL. Though, a proper distinction between HSF and Stark MBL needs to be established. In this thesis we explore this model with the goal to detect experimental evidence for HSF via state-dependent dynamics in a strongly tilted optical lattice.

Exploring the intriguing non-equilibrium phenomena of closed quantum many-body systems in real experiments poses many challenges. First, any quantum system that seeks to explore non-ergodicty has to be sufficiently decoupled from its environment so as to properly probe its intrinsic unitary evolution. Any bath coupling typically serves as an efficient way to drive a system to thermal equilibrium as it was investigated for MBL [55–61] and HSF systems [101]. Second, it requires precise control over the experimental parameters, a capability that state of the art experiments satisfy to unprecedented accuracy. This includes for example control over the Hubbard parameters such as the interaction strength that can be set by means of a Feshbach resonance [102] and the precise shaping and control of optical potentials with optical deflectors and spatial light modulators [103]. Over the last decade the capabilities of quantum simulators with ultracold atoms on optical lattices [104] have been evolving considerably. Quantum gas microscopes [105–109] for instance provide single-site resolution of charge [106, 107] and even spin [110] in one- and two-dimensional geometries and allow for an efficient experimental implementation of bosonic and fermionic Hubbard models. In particular, the Fermi-Hubbard model [7], originally formulated as a tight-binding model for the dynamics of interacting electrons in a solid state, bears high relevance for the understanding of real-life metals and insulators. Studies in one dimension for example demonstrated the evolution of magnetic correlations [111] and spin-charge separation [112]. In two-dimensional Fermi-Hubbard systems a lot of effort has been put into the exploration of the rich cuprate phase diagram as a function of temperature and electron-hole doping. Recent advances in atom cooling have enabled the realization of long-range antiferromagnetic order [110, 113] that is expected at zero doping and temperatures below the superexchange energy. Upon the introduction of hole doping more exotic phases like the pseudogap phase, strange metals [114] (non Fermi liquid) and d-wave superconductors are expected to emerge. A long-term goal is the understanding of two-dimensional cuprates and the responsible mechanisms for superconductivity, which is still in the focus of current research. This knowledge could then be employed to foster high-temperature superconductivity [115, 116] beyond current limitations.

The experiments reported in this thesis were carried out on an analog quantum simulator with ultracold fermions in a three-dimensional optical lattice. Via dynamically decoupling the orthogonal lattice axes we restrict the dynamics to one dimension realizing the 1D Fermi-Hubbard model. We have access to large system sizes up to 300 lattice sites far beyond numerically traceable dimensions and coherence times in the order of hundreds of tunneling times before open system effects limit the evolution times. We can trace the dynamics locally by using a bichromatic superlattice setup and preparing a charge-density wave (CDW) initial state with every second lattice site occupied. Our imbalance observable that traces the time evolution of atom densities on even and odd sites hence does not rely on macroscopic particle transport, but resolves local density patterns and evolutions and can thus even resolve slow dynamics which would not be visible in global observables. The CDW state was soon applied in other experiments as well, either with the lowest periodicity [29, 48, 60, 117], but also in a more general version with variable wavelength [54, 99, 114, 118]. In our experiment we employ the density imbalance to detect the localization properties of the many-body system and to resolve real-time hopping processes in the optical lattice. In future applications it will be worthwhile to extend the number of available observables to include entropy and correlators in a large-scale system as current experiments with high spatial resolution are typically still limited to relatively small system sizes.

Structure of this thesis

The projects reported in this thesis focus on the emergence of non-ergodic dynamics in an optical lattice with ultracold fermionic atoms. In particular, we explore new concepts in the spectrum between thermal and integrable systems that violate at least the strong version of ETH and thus lead to weak ergodicity breaking. We realize a one-dimensional lattice geometry with an either quasiperiodic or linear external potential and investigate the system's out-of-equilibrium dynamics starting from a charge-density wave initial state. This thesis is divided into four main parts which are described here in some detail.

Part I reviews the important theoretical concepts covered in this thesis. We start with a brief treatise of the eigenstate thermalization hypothesis (ETH) and integrability in **chapter 1**. **Chapter 2** is then dedicated to many-body localization (MBL) and reviews the central concepts necessary to understand the first project in this thesis including the MBL phase transition and open system effects. Finally, **chapter 3** starts with an overview of recently developed concepts and systems that cannot be classified by the previous categories of thermal and integrable systems. Instead they exhibit weak ergodicity breaking that truly conforms with neither of the two classes. Among those we then emphasize mobility edges and Hilbert space fragmentation as they are covered in the following parts of this thesis. In particular, a connection between Stark MBL and Hilbert space fragmentation is established.

The experimental setup is thoroughly described in part II starting with a brief overview of the experimental sequence in **chapter 4** including the cooling procedure and lattice setup. We continue to explain the spectroscopic techniques using radio-frequency and microwave operations. At this point the newly developed Potassium microwave setup as well as the technique of RF dressing are explained in detail. **Chapter 5** continues with the observables we measure in the reported projects. These are the density imbalance already employed in many previous projects, but also introduces new techniques resolving imbalance and in-situ distributions of singlons and doublons separately.

Part III is dedicated to the exploration of a many-body intermediate phase with ultracold atoms in a quasiperiodic potential realizing the generalized Aubry-André (GAA) model. In **chapter 6** the non-interacting model is studied numerically to explore its properties and highlight differences to the Aubry-André model in the eigenstate characteristics and imbalance time evolution. We also briefly review the results from [119] that thoroughly demonstrated the single-particle mobility edge in our system. The corresponding interacting model is investigated in **chapter 7** where we provide evidence for an MBL phase in an interacting model with a single-particle mobility edge and explore the existence of a many-body intermediate phase. We discuss the conceivable interpretations of our results.

In part IV we investigate the Fermi-Hubbard model with a strong linear external potential. **Chapter 8** reviews the properties of the non-interacting system, the Wannier-Stark ladder, and explains the experimental implementation and its importance for calibration measurements. As this model serves as an ideal platform to investigate the recently established mechanism of Hilbert space fragmentation, **chapter 9** is dedicated to the theoretical description and experimental exploration of the tilted Fermi-Hubbard model. We explain our observations, in particular a strong dependence of the dynamics on the initial conditions and the resolution of microscopic processes, in terms of a leading-order effective Hamiltonian. This is an indication that we indeed realize a model featuring Hilbert space fragmentation.

Part I.

Introduction to theoretical concepts

When a quantum many-body system is prepared in an initial state far from equilibrium, there are multiple possible outcomes regarding the steady-state conditions. While generic quantum systems obey the eigenstate thermalization hypothesis (ETH) and relax to thermal equilibrium, there are many prominent exceptions to this paradigm, especially in one spatial dimension. These include many-body localized systems, which retain memories of the initial state up to infinite times and fail to thermalize due to emergent integrability in terms of local integrals of motion. Recently, many new models have been developed that cannot be classified into either of the preceding classes (thermal and integrable) and require a more sophisticated distinction of strong and weak ergodicity breaking. In this part we review the important concepts of thermalization and many-body localization before focusing on intermediate classes that are also explored experimentally in this thesis, namely many-body mobility edges and Hilbert space fragmentation.

1. Thermalization and integrability in quantum systems

The term thermalization describes the relaxation of a many-body system to an equilibrium state that can be described by few thermodynamic quantities. This notion especially holds for arbitrary initial states and applies to most generic systems in nature. Important properties of classical and quantum thermalization are reviewed in previous works [120, 121]. Here, we give a brief review of thermalization in quantum systems and the powerful eigenstate thermalization hypothesis (ETH) as well as on integrable systems that represent an important exception to this concept.

1.1. Quantum thermalization and the Eigenstate Thermalization Hypothesis

A quantum system, in close analogy to classical thermodynamics, is viewed to be in thermal equilibrium if its state can be fully characterized by few extensive quantities such as particle number or energy. Local degrees of freedom become fully entangled with the rest of the system and it can be described by classical methods such as hydrodynamics [122].

This fact means that any memory of the details of an initial state must be erased during the process of thermlization and, above all, this equally applies to all states of a quantum many-body system in the thermodynamic limit, irrespective of their energy. This intuition, however, must be flawed as unitary time evolution of a closed quantum system cannot erase information given that time evolution is linear and chaotic dynamics are absent [123]. The resolution to this paradox is that the memory is not destroyed, but hidden non-locally. The entanglement spreading over time distributes the information and makes it inaccessible when measuring local properties of the system. This process of "information loss" is called decoherence [2]. In quantum thermodynamics a closed quantum system can reach thermal equilibrium under its own unitary dynamics because the whole system can act as a heat bath for a small subsystem. A closed quantum system is fully decoupled from its environment, in particular there is no energy exchange with a quantum heat bath. In nature and any realistic experiment though, there is always some finite coupling between a system and its environment with a strength Γ_b. However, as long as the inverse of this coupling is much larger than characteristic timescales of the system ($\tau_{sys} \ll 1/\Gamma_b$), it can be assumed to be closed. Only on longer times it will reach thermal equilibrium due to coupling to a bath.

The classical definition of ergodicity requires that all available microstates of a system allowed by global conservation laws are occupied with equal probability over a long period of time [124]. A direct adaption of this notion to the quantum world, however, is not straightforward. Consider a generic non-equilibrium quantum state $|\psi(0)\rangle = \sum_\alpha c_\alpha |\alpha\rangle$ expanded in the basis of eigenstates $|\alpha\rangle$ that evolves under unitary time evolution governed by a Hamiltonian H as

$$|\psi(t)\rangle = e^{-iHt/\hbar} |\psi(0)\rangle = \sum_\alpha c_\alpha e^{-iE_\alpha t/\hbar} |\alpha\rangle . \tag{1.1}$$

Every coefficient acquires a phase determined by the eigenstate energy E_α, but the probability to find the system in a certain eigenstate is given by $p_\alpha = |\langle\alpha|\psi(t)\rangle|^2 = |c_\alpha|^2$ and is therefore time-independent and only depends on the choice of initial conditions. This is in contradiction to the classical definition where the whole phase space is explored and therefore quantum ergodicity must have a different origin.

One way to resolve this paradox is to consider the infinite-time average of a physical observable $\hat{\mathcal{O}}$ [16] given by

$$\langle\hat{\mathcal{O}}\rangle_\infty = \lim_{t\to\infty} \frac{1}{t} \int_0^t dt' \, \langle\psi(t')| \hat{\mathcal{O}} |\psi(t')\rangle = \sum_\alpha p_\alpha \langle\alpha| \hat{\mathcal{O}} |\alpha\rangle , \tag{1.2}$$

assuming that there are no degeneracies in the Hamiltonian. As can be directly seen, it depends on the occupation probabilities p_α and the respective expectation value of the observable. Off-diagonal elements of $\langle\hat{\mathcal{O}}\rangle_\infty$ average out because they oscillate at different frequencies. Now, if $\langle\hat{\mathcal{O}}\rangle_\infty$ displays a thermal quantity, this implies that the expectation values of every individual eigenstate agree with the microcanonical ensemble that only depends on the energy E: $\langle\alpha| \hat{\mathcal{O}} |\alpha\rangle = \langle\hat{\mathcal{O}}\rangle_{mc}(E)$. This defines the main statement of the Eigenstate Thermalization Hypothesis (ETH) [3, 4], which relates the thermal behavior of a quantum system to the expectation value of individual eigenstates. Equally put, this further implies that systems obeying the ETH have thermal observables. Quantum thermalization happens on the level of individual eigenstates which are thermal by themselves. Starting from a certain initial state, thermalization removes coherences that are initially present and reveals the thermal nature of the system. Another consequence is a volume-law scaling of the entanglement entropy of the system that is defined as the von Neumann entropy $S = -\,\mathrm{tr}(\rho_A \ln(\rho_A))$ of subsystem A. For a strictly thermal and thus maximally entangled state $\rho_A \simeq \dim(A)^{-1}\mathbb{1}$ the entanglement entropy indeed becomes $S = \log(\dim(A)) \propto \mathrm{vol}(A)$.

As the name already suggests, the ETH is a hypothesis and no formal proof exists. Though, all known thermalizing systems obey the ETH as proven by numerical investigations [5], such that it is suggestive that this assumption can explain the generic process of thermalization of isolated quantum systems. Whether ETH is a necessary condition for a given system to thermalize is still an open question. On the other hand, systems that explicitly violate the ETH such as many-body localization (see chapter 2) have attracted considerable interest and some classes of such systems are covered in this thesis.

1.2. Integrable systems

One example of systems violating the ETH are integrable quantum systems. They possess an extensive number of conserved quantities that commute with the Hamiltonian and restrict the system dynamics providing a mechanism to elude thermalization. Another definition of integrability is that the system can be solved with the Bethe ansatz [6]. Characteristic properties of interacting systems can encompass long-lasting oscillations or relaxation to an equilibrium state described by a generalized Gibbs ensemble where at least some observables exhibit a non-thermal equilibrium state. Though, this may in general be hard to distinguish from a thermal system such that experimentally one is rather interested in the former case as an indicator of integrability.

There are are many models in condensed matter physics that are integrable, the most prominent ones being all non-interacting systems, but also the Lieb-Liniger model [8], the XXZ model and the Heisenberg spin chain [9], all in one dimension. Further, the one-dimensional Fermi-Hubbard model is integrable for all interaction strengths [125]. Its integrability and connection to non-equilibrium transport properties was studied at our experiment and published in [126]. The Fermi-Hubbard model is also integrable in the limit of infinite tilt (see chapter 9), where it is known that non-thermal properties emerge. However, integrability is in general a fine-tuned effect and even small perturbations like an external potential or weak long-range interactions break the integrability and restore thermalization.

Integrability as a mechanism to avoid thermalization and thus violate the ETH can also occur in a different context. In the following chapters we will explore the role of integrability emerging in many-body localized systems that are an established class of ergodicity-breaking ensembles and usually insensitive to small perturbations.

2. The Anderson insulator and many-body localization

In this chapter the most important properties of the many-body localized phase are only reviewed briefly to an extent that is necessary for the project in part III. They are mainly described in the previous doctoral theses at this experiment [120, 121]. In short, MBL denotes the persistence of Anderson localization in the presence of interactions. Unlike generic systems, a many-body localized ensemble does not thermalize under unitary dynamics which means that it cannot serve as its own heat bath. This violates the eigenstate thermalization hypothesis (ETH) [3, 4] and therefore attracted a lot of theoretical and experimental interest (see reviews [15, 17, 127] and references therein).

2.1. Single-particle localization in random and quasi-periodic potentials

2.1.1. Anderson localization in real-random disorder

A spatially localized particle in a homogeneous lattice potential is a superposition of Bloch waves. Its wavefront traveling with the fastest velocity allowed by the dispersion relation consequently spreads ballistically with time. This is in contrast to a localized system. The discovery of localization dates back to the famous work of Phil W. Anderson in 1958 [11], who predicted the absence of diffusion in certain random lattices.

For the special case of spinful fermions (spin-1/2) with two spin components σ in a one-dimensional lattice the Hamiltonian reads

$$\hat{H}_A = -J \sum_{i,\sigma} (\hat{c}^\dagger_{i+1,\sigma} \hat{c}_{i,\sigma} + \text{h.c.}) + \Delta \sum_{i,\sigma} V_i \hat{n}_{i,\sigma}, \tag{2.1}$$

where the first term describes the hopping between neighboring lattice sites with amplitude J. The operators $\hat{c}_i$ ($\hat{c}^\dagger_i$) are the fermionic annihilation (creation) operators destroying (creating) a particle with spin $\sigma \in \{\uparrow, \downarrow\}$ on lattice site i. The second term represents the disorder part where Δ denotes the amplitude and $V_i \in [-1, 1]$ is the on-site disorder value, typically randomly chosen from a box-shaped distribution. According to Bloch's theorem, the eigenstates of particles in a regular lattice are given by Bloch waves, that represent a plane wave modulated by a periodic function $\phi(x)$ with the same periodicity as the lattice. The wavefunction can be written as $\psi(x) \propto e^{-ikx}\phi(x)$ and is fully delocalized in real space. Conversely, in the presence of disorder it can be shown that the wavefunctions become exponentially localized as a consequence of quantum mechanical interference. The parts of the wavefunction reflected from the potential wells interfere constructively, while wavepackets transmitted in forward direction interfere destructively. The eigenstates of the Anderson model in Eq. (2.1) are exponentially localized for any finite value of the disorder $\Delta > 0$ and for all energies in one and two dimensions. Given that Anderson localization is a wave phenomenon analogues were found in optics and acoustics [128].

The direct observation of localization in a physical experiment was difficult to achieve because it requires a time-independent potential. This condition is not fulfilled in usual atomic crystals due to thermal excitations and Coulomb interactions. This requires the realization of artificial potentials with controlled disorder and was first observed experimentally in two different kinds of systems. The first was realized with a Bose-Einstein Condensate (BEC) expanding in a one-dimensional waveguide in the presence of a disorder potential created by laser speckles [26]. The second type of experiment demonstrated the transverse localization of light in a two-dimensional photonic lattice with random fluctuations [27]. Anderson localization can also be observed in three dimensions [129, 130], although the system possesses a localization transition at finite disorder that is further energy-dependent (see sec. 3.1.1). Whether localization can also persist in an interacting system remained an open question for many decades until theoretical works were able to provide an answer to this question. We will discuss this in sec. 2.2.

2.1.2. Localization in quasiperiodic potentials

In 1980 Aubry and André [24] discovered that randomness is not a prerequisite to have localization in one dimension. Instead, they introduced a quasiperiodic potential with perfect correlation, but whose pattern never repeats itself in any finite system. This characteristic is revealed when looking at the continuum Hamiltonian ("incommensurate lattice model") in Eq. (2.2):

$$H = -\frac{\hbar^2}{2m}\frac{d^2}{dx^2} + V_p \cos^2(2k_p x) + V_d \cos^2(2k_d x + \phi). \tag{2.2}$$

Herein, V_p and V_d denote the strength of the primary and detuning potential respectively and ϕ is the relative phase between them. Besides the kinetic part it contains two periodic potential terms with with a wavenumber ratio $\beta = k_d/k_p$. This quantity β will be referred to as the incommensurability in the following. The pattern repeats itself if the wavenumber ratio can be written as $k_d/k_p = p/q$ with $p, q \in \mathbb{N}$, hence the wavelength ratio is rational. It can be shown that the eigenstates of such a system are extended Bloch waves (modulated plane waves) such that this is not relevant in the context of localization. On the other hand, if β is irrational, it does feature localization. In an experimental setup with finite size this conditions is always satisfied since the laser wavelength is an irrational quantity by itself. Moreover, in finite systems it is considered a sufficient condition to have $\beta > 1/L$.

The continuum model in Eq. (2.2) is barely used in theory and is instead mapped to lattice models in a tight-binding description, where the dynamics are restricted to the lowest band. These systems are easier to simulate and established methods are available. This mapping is performed in previous works [120, 131] and it ultimately results in the celebrated Aubry-André model in Eq. (2.3)

$$\hat{H}_{AA} = -J \sum_{i,\sigma} (\hat{c}^{\dagger}_{i+1,\sigma} \hat{c}_{i,\sigma} + \text{h.c.}) + \Delta \sum_{i,\sigma} \cos(2\pi\beta i + \phi) \hat{n}_{i,\sigma}. \tag{2.3}$$

It is the primarily employed model for localization in quasiperiodic systems both in theory and experiment. Unlike the Anderson model which localizes the wavefunction already at infinitesimal disorder, the Aubry-André model has a localization transition at $\Delta/J = 2$. This follows from the self-duality at this point of the model between real and momentum space [25]. Moreover, it is possible to give an analytic expression for the single-particle wavefunction as a function of the detuning strength. It is given by $|\psi(x)|^2 \propto \exp(-|x - x_0|/\zeta)$, where x_0 is the center position of the particle and $\zeta = 1/\ln(\Delta/2J)$ is the localization length which diverges at the transition point. The localization mechanism in the quasiperiodic case is different from the real-random case. In the latter it is an interference phenomenon while in the quasiperiodic case the localization emerges from the spectral properties of the Schrödinger equation [132]. The different origins of localization are further highlighted in the actual non-interacting time evolution under the Hamiltonians in Eqs. (2.1) and (2.3). Starting from a single particle localized in the center of a homogeneous lattice we observe the characteristic ballistic expansion with the average group velocity of $v_{av} = \sqrt{2}d/\tau$ in Fig. 2.1a [133] with the tunneling time $\tau = \hbar/J$. Upon the addition of disorder with amplitude $\Delta/J = 2.5$, the particle in the Anderson model is clearly confined to a small spatial region, an obvious hallmark for localization (Fig. 2.1b). In the AA model the dynamics are very similar although confined to a narrower spatial region. The analytical localization length of this model is indicated by the dashed vertical lines (Fig. 2.1c). In both cases the expansion dynamics are shown for a single realization of the disorder pattern or detuning phase. In order to properly distinguish the different disorder types and the underlying localization mechanism, we refer to the external potential in the Anderson model as *disorder* and in the AA case as

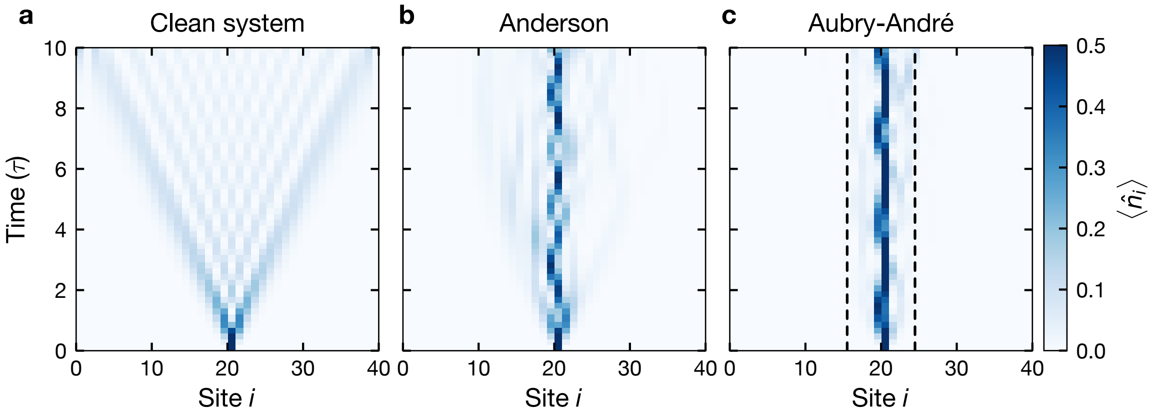

Figure 2.1.: Expansion dynamics in a disordered lattice: Time evolution of the occupation density of a single particle initialized in the center of the lattice. **a** The dynamics in a clean lattice reveals the typical ballistic expansion. **b** Time evolution in the Anderson model in the presence of random disorder. **c** At the same detuning strength the dynamics are more confined in the AA model. The dashed lines indicate the analytical localization length. In the last two panels a disorder / detuning strength of $\Delta/J = 2.5$ was considered and the data is obtained for a single realization of the disorder pattern or detuning phase ϕ. For a better visualization the maximum density shown is 0.5 and the initial state is fully localized on a single lattice site with the initial density 1.

detuning.

One of the main reasons for the success of the AA model is the direct relevance in experimental applications. The Hamiltonian in Eq. (2.2) can be implemented relatively straightforwardly by superimposing two lattices with incommensurate wavelength ratio. Exactly this approach was taken in the first demonstration of single-particle localization in a quasiperiodic potential with a non-interacting Potassium BEC [28]. In a subsequent study with a fermionic quantum gas the transition in the AA model was observed equally [29]. While the former experiment measured the cloud size of the expanding BEC as global observable, the latter made use of a local observable. Fig. 2.2 shows the density imbalance (see sec. 5.1) as a function of the detuning Δ/J together with exact diagonalization (ED) simulations matching the experimental setup as closely as possible. The simulation of the ideal model (Eq. 2.3) clearly shows the sharp localization transition at $\Delta/J = 2$ while the experimental data rather suggests a smooth crossover and good agreement is only established for strong detuning. It can be confirmed convincingly that this crossover traces back to the harmonic confinement which leads to a finite localization length even in the absence of disorder/detuning. The confinement present in the experiment is determined in an independent measurement and including the additional term $\frac{1}{2}m\omega^2(x-x_0)^2$ with trap frequency ω, atomic mass m and center position x_0 in the simulations matches the

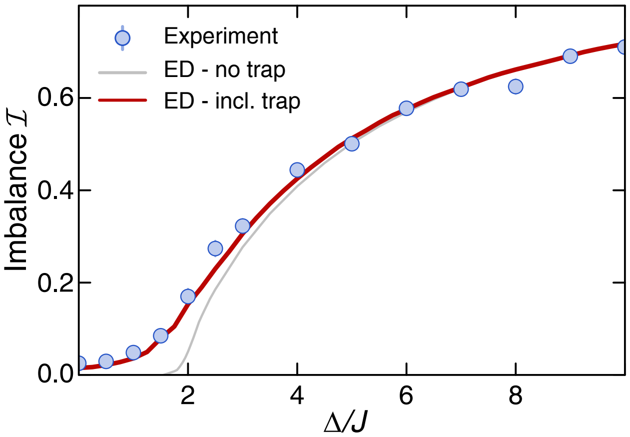

Figure 2.2.: Localization in the AA model: Steady-state imbalance as a function of the detuning strength Δ/J averaged over three points in time between 13 and 20τ and four different phases ϕ. The blue points represent the experimental data with the error bars showing the standard error of the mean. Numerical results are obtained from ED on a system as large as the experimental one ($\approx$ 200 lattice sites). While the gray line reflects the ideal system, the red solid line taking into account the external harmonic potential matches the data very well. Figure taken from [29] with permission.

experimental data impeccably. Moreover, it proves that the AA model is very reliably realized in our system, which serves as an important reference for the project reported in part III.

2.2. Many-body localization

The term many-body localization defines the persistence of localization in an interacting many-body system and can be understood as a generalization of Anderson localization. This phase of matter eludes thermalization because the disorder prevents an efficient energy exchange between different degrees of freedom and the quantum system can no longer serve as a heat bath for itself. Hence, MBL represents a violation of the eigenstate thermalization hypothesis. The existence of an MBL phase is not at all a straightforward conclusion from the localization in single-particle systems because one could imagine that interactions open up new transport channels. For instance, a particle may expand via an avalanche of excitations from a high-energy initial state to a low energy final state and restore transport via this channel [134]. An important step was the seminal work by Basko et al. [12] that predicted localization below a critical temperature based on a perturbative analysis and they were thus the first to establish a non-thermal phase in an interacting quantum system. This view was later corrected in [13] where the authors stated that MBL can even exist at infinite temperature in a disordered lattice model with spinless fermions and nearest-neighbor interactions. Similar works on the Heisenberg spin chain confirmed this result [14, 135]. Unlike integrable systems the MBL dynamical phase of matter is insensitive to small changes in the microscopic Hamiltonian. Central properties of the MBL phase are nicely reviewed [15–17] as well as in previous theses conducted at this experiment [120, 121] and in the following we will only highlight the aspects that are particularly relevant for the project reported in part III.

2.2.1. Phenomenology of MBL

Throughout the theoretical and numerical studies of many-body localization a couple of spectral and dynamical observables have been employed to characterize the new emergent phase of matter and investigate the transition from an ergodic phase to MBL. A few of those observables are briefly reviewed here without giving a complete list of available diagnostics.

Eigenstate entanglement entropy

The entanglement entropy scaling of eigenstates can distinguish between a thermal and an MBL system [136]. The von Neumann entropy $S = -\mathrm{Tr}(\rho \ln(\rho))$ for a density operator ρ scales with the dimension for a thermal system and implies that eigenstate entanglement can span the entire system, it is therefore referred to as volume-law scaling and the corresponding states are maximally entangled. Conversely, many-body localized systems exhibit an area-law scaling that is constant in one dimension. The low eigenstate entanglement of MBL states is explained by the toy model introduced in [137]. It considers two subsystems A and B that are connected along the boundary ∂A. Without interactions the eigenstates of the system are simple product states of both subsystems with zero entropy. Interactions coupling both subsystems act locally at the boundary within the localization length and longer-range couplings are exponentially suppressed in agreement with the notion of localization. Thus, spins are only entangled between A and B close to the boundary, yielding an area-law scaling of the entanglement entropy $S \propto \mathrm{vol}(\partial A)$. The area-law scaling was confirmed numerically [63, 138, 139] and also served as an observable across the transition from a thermal to an MBL system.

Level spacing statistics

Spectral statistics of adjacent energy levels of a many-body Hamiltonian are capable of capturing the transition from a diffusive to an insulating phase. To understand this behavior we consider the gap between adjacent energy levels $\delta_n = E_{n+1} - E_n$. Dynamical timescales t_{dyn} of a system, in particular on the context of thermalization described by Eq. (1.2), are governed by the transition between neighboring states and can be approximated as $t_{\text{dyn}} \propto 1/\delta_n$. The contribution of small δ_n leads to long characteristic timescales which are suppressed in a thermal system. Hence, they exhibit level repulsion and obey a Wigner-Dyson distribution with the probability density vanishing as $p(\delta_n = 0) = 0$. This was first confirmed in [13]. Contrarily, in a many-body insulating phase such as MBL the eigenstates are localized in the many-body Fock basis. States nearby in energy do not interact and instead show a Poissonian distribution with $p(\delta_n = 0) = 1$. The phase transition can then be captured by a change of the energy level distribution. In order to obtain a dimensionless parameter in analogy to local order parameters one typically considers the gaps between adjacent energy levels and defines the ratio

$$r_n = \min\{\delta_n, \delta_{n-1}\} / \max\{\delta_n, \delta_{n-1}\}. \tag{2.4}$$

As long as there is no mobility edge, this quantity is typically averaged across large parts of the spectrum to obtain the mean spacing parameter $\bar{r}$. In the case of a Poissonian distribution, i.e. for an integrable or localized many-body phase, the mean value $\bar{r}_P \simeq 0.386$ while for the Wigner-Dyson distribution for a thermal system the mean value was determined numerically to be $\bar{r}_{WD} \simeq 0.530$. It should be noted that for a finite-size system the statistics change smoothly across the transition such that a proper finite-size scaling analysis is required to obtain conclusive results. Note that the level statistics are a more versatile tool and can be applied to many classes of many-body systems. While generic chaotic systems obey Wigner-Dyson statistics, integrable and other non-ergodic systems exhibit Poisson statistics, so this tool is very common for other types of ergodicity breaking as well.

Dynamical evolution

While the diagnostics above are rather the result of numerical analyses, one can further gain an analytical understanding of the physics in the MBL phase. It is now believed to be well understood based on a phenomenological description via local integrals of motion. This notion originates from integrable systems, which inherit their non-ergodicity from an extensive number of conserved quantities. Given the low entanglement in MBL systems, the starting point are product states. Together with quasilocal unitary transformations one obtains local integrals of motion τ_i^z that are exponentially localized around their carrier as opposed to the situation in a thermal system. The localization length of the operators can be interpreted as the many-body localization length. These local operators form a complete set of local integrals of motion and are often referred to as LIOMs or l-bits [23, 137]. The MBL Hamiltonian can be expressed in terms of LIOMs and becomes

$$H = \sum_i \tilde{h}_i \tau_i^z + \sum_{i,j} J_{ij} \tau_i^z \tau_j^z + \sum_{i,j,k} J_{ijk} \tau_i^z \tau_j^z \tau_k^z + \cdots \tag{2.5}$$

The couplings between remote operators, also called non-local interactions, decay exponentially with distance according to $J_{ij} \propto J_0 \exp(-|i-j|/\lambda)$ with a characteristic length scale λ. Given that this effective MBL Hamiltonian commutes with an exponentially large number of integrals of motion τ_i^z, this description proves an emergent integrability in the MBL phase in close analogy to common integrable systems. It further directly explains the Poissonian level statistics as well as the absence of particle transport.

In order for two distant spins to become entangled with each other, the time grows exponentially with the distance and thus correlations propagate logarithmically in time. While the logarithmic entanglement growth mentioned above was first discovered numerically [21], the picture of local integrals of motion can readily explain this behavior. Indeed, starting from a system in a product state, the entanglement entropy in response to a quantum quench evolves according to [21, 22, 135]

$$S(t) \propto \xi \ln(J_0 t/\hbar) \tag{2.6}$$

where ξ can be interpreted as the many-body localization length. The characteristic time evolution of the entanglement in an MBL system comprises three stages. In the beginning the entropy quickly rises to the value of the single-particle system on the order of few tunneling times. Subsequently, the entropy grows logarithmically in time with the slope depending on the localization length, as predicted by Eq. (2.6). This logarithmic evolution is one of the central defining features of the MBL phase [21]. At exponentially long times the entropy saturates to a volume-law steady-state value that is subthermal and thus smaller than the Page value [140], which would be attained in a thermal system. Conversely, entanglement in a thermal system spreads ballistically ($S(t) \propto t$) [135, 141]. An MBL system, despite the absence of particle transport and therefore being a perfect insulator with vanishing conductivity, equilibrates. Though, the "equilibrium state" is a highly non-thermal state with a certain memory of the initial conditions, which distinguishes it fundamentally from a thermal phase. It is worth mentioning that a recent study [142] observed that while the entanglement entropy grows logarithmically, the number entropy, expected to obey an area-law, actually grows as $S_N \propto \ln(\ln(t))$ in a one-dimensional system. This would indicate ongoing subdiffusive dynamics that would ultimately thermalize the system. Though, the authors cannot exclude that the slow increase ceases at long times such that the established MBL phenomenology would not be challenged.

2.2.2. Previous theory and experiments

Theoretical tools

As complementary works to the perturbative studies introduced above, extensive numerical simulations have been carried out to further investigate the phase of many-body localization and the transition to the thermal phase (see sec. 2.3). The primary challenge when simulating an interacting quantum many-body system is the size of the Hilbert space that grows exponentially with the system size. This mostly affects exact diagonalization (ED) simulations, which are typically limited to about 20 lattice sites due to memory limitations on a classical computer. Larger systems are accessible to time-dependent density-matrix renormalization group (tDMRG) approaches [143–145]. Though, these are only applicable in the strongly localized regime, otherwise the growth of entanglement entropy limits the accessible time due to an increasing cumulative error rate. These limitations highlight the need for experiments, which typically provide larger system sizes and thereby circumvent the problems of ED. Given these limitations, theory works typically reside to spin models instead of Hubbard models. They qualitatively exhibit the same physics with the main advantage that the local Hilbert space is smaller such that larger systems with weaker finite-size limitations can be explored. In a spin chain every lattice site is occupied by a spin that either points up or down. Conversely, a spin-1/2 Hubbard model has four allowed configurations per site (spin up, spin down, doublon or hole). In the context of many-body localization the primarily employed model is the XXZ spin chain

$$\hat{H}_{\mathrm{XXZ}} = \frac{J}{2}\sum_i (S_i^x S_{i+1}^x + S_i^y S_{i+1}^y) + V\sum_i S_i^z S_{i+1}^z + \sum_i h_i S_i^z. \tag{2.7}$$

The first term induces the swapping of neighboring spins with rate J and the second term denotes the interaction adding energy V if adjacent spins have the same direction. The last term represents an additional field along the z-direction realizing e.g. a random or quasiperiodic potential. This model can be mapped to a one-dimensional system of spinless fermions with nearest-neighbor interactions under the Jordan-Wigner transformation:

$$\hat{H}_{sf} = -J\sum_i (\hat{c}_i^\dagger \hat{c}_{i+1} + \text{h.c.}) + V\sum_i \hat{n}_i \hat{n}_{i+1} + \sum_i h_i \hat{n}_i. \tag{2.8}$$

This readily explains why most publications focus on these two models since they are related by a transformation. The main differences between the spin and Hubbard models is the type of interactions and the fact that the spin degree of freedom is not respected. They therefore describe qualitatively the same physical processes, but quantitative agreement is not necessarily satisfied. For example the precise value of the critical point of the thermal-MBL transition might be slightly model-dependent. In the projects reported in this thesis the simulations reproducing our experimental results are performed for the full

Hubbard model (Eq. 4.2) exclusively and we employ both techniques, ED and tDMRG (or time-evolving block decimation, TEBD).

Experiment

After the early theoretical works on many-body localization the issue soon took on experimental significance with the emergence of quantum simulators that provide a high level of control and tunability while satisfying the necessity of a closed quantum system over sufficiently long times. These experimental platforms currently encompass cold atom experiments, ion traps and superconducting qubits although the future may bring about further types of quantum systems. This section is supposed to give a short overview of the current status of experiments on MBL and closely related topics.

The first experiments focusing on MBL were quantum simulators based on ultracold atoms as they provide good isolation from the environment on at least intermediate timescales. They typically prepare out-of equilibrium initial states with high energy density in order to examine the MBL phase and the transition which distinguishes it fundamentally from known quantum phase transitions at zero temperature. Schreiber at al. [29] simulated the Aubry-André model (Eq. 2.3) with fermions in two spin states realizing the Hamiltonian

$$\hat{H}_{\text{exp}} = \hat{H}_{AA} + U \sum_i \hat{n}_{i,\uparrow} \hat{n}_{i,\downarrow} \tag{2.9}$$

with on-site interactions of strength U. From recorded time traces of the imbalance starting from a charge-density wave initial state they inferred dynamical properties of the system as a function if the Hubbard parameters Δ and U. In the absence of detuning ($\Delta = 0$) the imbalance shows a fast decrease and settles to zero. This is in agreement with a thermal system since an equal occupation of even and odd lattice sites is expected. Adversely, for stronger detuning above the critical detuning strength a finite steady-state value is observed, indicating certain memory of the initial state and thus the presence of MBL in a system with quasiperiodic detuning. This statement was justified for a large range of interaction strength as well as multiple energy densities of the initial state.

The development of quantum gas microscopes with single-site resolution made new observables such as entanglement entropy and correlations experimentally accessible. This was the direction taken by [30, 31] who basically confirmed the expected behavior of the entanglement entropy in the thermal and many-body localized phase, including the logarithmic growth in time, area-law scaling of the number entropy and the non-thermal volume-law saturation value which further distinguishes it from a thermal system. The accessibility of on-site densities further enables the investigation of correlations. Such an experiment was reported in [49], where the authors studied the many-body entanglement in the quantum critical regime and across the MBL transition and revealed the structure of sparse resonances across the transition in the Aubry-André model.

While MBL is well-established in one dimension, for both random and quasiperiodic disorder, the situation is less clear in higher dimensions. This issue is a topic of ongoing theoretical debate without an evident conclusion. While earlier works [50, 146, 147] argued that no MBL exists in higher dimensions due to to an avalanche effect of thermal bubbles caused by regions of weak disorder, more recent works with thorough numerical methods conclude that they find signatures of MBL in two [51] and even three dimensions [52] for specific models without being able to make more general statements though. These recent findings are supported by experiments studying the fate of MBL in a two-dimensional system, either in a 2D quasiperiodic lattice setup [53] or in a quantum gas microscope with random disorder created by a speckle pattern [54, 62]. Both experiments find clear indications of MBL in two dimensions although these results are limited to a finite observation time.

Another relevant platform are chains of ions trapped in a one-dimensional Paul trap, recently employed to realize the disordered transverse field Ising chain

$$\hat{H} = \sum_{i<j} J_{i,j}\sigma_i^x\sigma_j^x + \frac{B}{2}\sum_i \sigma_i^z + \frac{1}{2}\sum_i D_i\sigma_i^z \tag{2.10}$$

with the Pauli matrices σ_i acting on spin i, long-range couplings $J_{i,j}$, homogeneous magnetic field B and random on-site disorder D_i [32]. Monitoring the time evolution of the magnetization $\langle\sigma_i^z\rangle$ the authors identified the onset of localization for sufficiently strong disorder, a hallmark of MBL. They further confirm the logarithmic entanglement entropy growth as well as Poissonian level statistics directly. This platform is particularly interesting because it integrates tunable long-range interactions via the Coulomb force as opposed to on-site interactions in cold atom experiments. Whether MBL can persist for non-local interactions is still an open question [148] and these experiment can potentially shed light on this issue.

Finally, superconducting qubits are another promising platform, both for quantum computation (see e.g. Google's publication [149] on a quantum computer with 53 qubits demonstrating quantum supremacy) as well as for the simulation of quantum many-body systems with programmable potentials. For instance, in [33, 150] the authors observe MBL and an energy-dependent transition point (i.e. a many-body mobility edge, see sec. 3.1.2) and in a recent work [151] the non-local interactions of the LIOM picture (Eq. 2.5) were even addressed directly. Though, these platforms are still limited to small system sizes and relatively short evolution times such that the results are not fully conclusive.

2.3. The many-body localization transition

2.3.1. General

Classical phase transitions are characterized by a discontinuity in the first or higher derivative of a thermodynamic function of the physical system. Phase transitions are described by Landau's theory [152] that further predict spontaneous symmetry breaking at the critical point. Prominent examples for classical phase transitions are the transition from a ferro- to a paramagnet at the Curie temperature or the melting of ice. Conversely, quantum phase transitions [153] only happen at zero temperature such that transitions cannot be driven by thermal fluctuations. Instead, the absolute ground state as a function of a non-thermal parameter can be influenced giving rise to a transition due to quantum fluctuations originating from Heisenberg's uncertainty principle. A typical example appears in the Bose-Hubbard model. The ground state phase diagram exhibits a superfluid and a Mott-insulating phase and the transition is driven by the ratio between the kinetic and the interaction energy.

The transition between the thermal and many-body localized phase, however, does not fit into the framework of quantum phase transitions within quantum statistical mechanics as described above. First, the MBL transition is a dynamical transition that has no manifestation in static thermodynamic quantities. Moreover, it is typically referred to as an eigenstate transition because the entanglement entropy scaling changes from volume-law to area-law when crossing the MBL transition. Second, the MBL transition is not restricted to the absolute ground state, corresponding to a zero temperature state, of the system. It was found that all states throughout the spectrum undergo the transition independent of their energy. These findings are reviewed in [45–47] and references therein. In the following, we will summarize the most important dynamical properties of the MBL transition and highlight their relevance for the work presented in part III of this thesis.

Most papers studying dynamics at the MBL transition consider the Heisenberg or XXZ spin chain with random disorder [14, 41, 42, 139, 154]. The main characteristic of this quantum critical phase are slow dynamics in terms of a sub-ballistic entanglement growth $S(t) \propto t^{1/z}$ with $z \geq 1$ and a power-law decay of the spin-density imbalance $\mathcal{I}(t) \propto t^{-\xi}$. These exponents $1/z$ and ξ depend on the disorder strength and vanish upon approaching the transition point from the thermal side. This scaling also applies to other observables such as the optical density or the return probability as studied in [42] and consequently this regime is referred to as subdiffusive as opposed to the usual diffusive behavior in thermal systems. This characteristic was explained by a sparse backbone of resonances [139] that provides long-range entanglement sufficient to thermalize the system on the thermal side of the transition. A physical picture of the transition was developed in the framework renormalization group (RG) approaches [43, 44]. It is based on the occurrence of rare regions, local subsystems that are in a different phase than the surrounding system. These rare regions serve as a bottleneck for transport and in particular close to the MBL transition they can impede thermalization on long timescales. It can be shown that the subdiffusive scaling given above can be explained by this Griffiths picture [120, 155] where the balance between finding such a rare region and the induced transport is considered. RG simulations confirm the results previously obtained with exact diagonalization. Conversely, it is natural to consider the occurrence of rare thermal regions in the MBL phase [156], but at this point relaxation within the MBL phase is not well understood. Whether this mechanism equally applies to quasiperiodic systems is still under debate. Given the correlation and periodicity of the detuning potential, rare regions that are induced by small areas with weak or large disorder, cannot exist. Instead, randomness in the initial state might lead to similar dynamics although such regions would ultimately be removed in the thermalization process. See [120] for a more detailed discussion.

2.3.2. Previous experimental results

In a previous project at our experiment the authors studied the dynamics across the MBL transition in a one-dimensional Fermi-Hubbard model with quasiperiodic detuning [48]. From imbalance time traces recorded for multiple detuning strengths they analyzed the decay dynamics and compared them to numerical results obtained with ED on 20 lattice sites. Fig. 2.3a shows three exemplary traces for different detuning strengths on a doubly logarithmic scale, exhibiting a certain imbalance decay during time evolution. This decay becomes weaker upon reaching stronger detunings. The experimental points are in good agreement with the numerics and can seemingly be described by a power-law as indicated by the yellow lines. In order to get more quantitative insights into the decay dynamics, the traces are fitted with a power-law $\mathcal{I}(t) \propto t^{-\alpha}$ and the resulting exponents are plotted in Fig. 2.3b as a function of the detuning strength. They continuously decrease upon approaching the transition point until it is supposed to vanish in the MBL phase. The finite plateau α_0 can be attributed to open system effects (see sec. 2.4) and our system is assumed to be many-body localized when the relaxation exponent reaches its plateau value. This method can further be used to extract an experimental lower bound for the MBL transition point, in this case it is located at $\Delta_c = (3.8 \pm 0.5)J$. We will use this knowledge about the AA model for the experiment on the many-body intermediate phase reported in chapter 7.

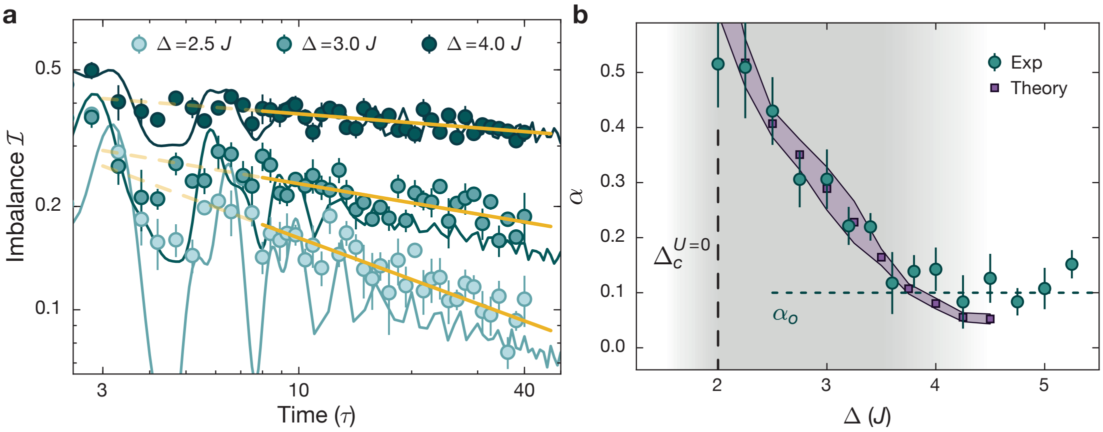

Figure 2.3.: Experimental results on the MBL transition in the Aubry-André model: All results are obtained for the interaction strength $U/J = 4$ and numerical simulations were performed on a system with 20 lattice sites. **a** Imbalance time traces taken at detuning strengths below the MBL transition. Solid lines are ED simulations and yellow lines are power-law fits between 8 and 40 tunneling times. **b** Dynamical relaxation exponents as a function of the detuning strength Δ/J starting from the single-particle localization transition at $\Delta/J = 2$. The experimental data points settle to a positive plateau value α_0 due to open system effects and the resulting finite lifetime (see sec. 2.4). The gray shaded area represents the determined regime of slow dynamics. Purple squares indicate numerical results including the uncertainty estimate from a finite-size analysis. Figure adapted from [48] with permission.

2.4. Open system effects

The considerations in the previous sections are only precisely valid in a closed quantum system that is perfectly isolated from its environment for infinite times. In an experiment, although tremendous progress has been made in this respect which finally enabled the studies of MBL, the isolation can only be established over finite times before bath coupling will finally set in. The fate of MBL in a quantum system coupled to an external bath soon attracted considerable theoretical interest [55–59]. The common result of these studies reads that the coherent nature of the localized phase gets ultimately destroyed, restoring quantum thermalization. Hence, in order to interpret realistic experimental data it is essential to qualitatively understand the impact of such open system effects. A quantitative analysis of this question was studied experimentally on our system for two different cases of couplings to the environment. Since these mechanisms also affect the conclusions drawn for the project in chapter 7, the findings are briefly reviewed at this point.

The dominant decay mechanism present in our experiment is the residual coupling between neighboring one-dimensional systems along the orthogonal directions in our optical lattice setup, that was studied in detail in [60] for the case of quasiperiodic detuning. On short timescales the dynamics are restricted to the one-dimensional tubes along the primary lattice axis, but on longer timescales the particles can also hop along the orthogonal axes. The detuning pattern is identical in all tubes such that inter-tube tunneling is resonant. In the non-interacting case the system is exposed to external noise and photon scattering (see below), limiting the lifetime of atom numbers to a few thousand tunneling times. The imbalance remains virtually unchanged because the system is separable and both directions can be decoupled. In the presence of interactions, however, this separability is broken and dynamics along the transverse axis affect the localization properties of the system. Therefore, coupled tubes serve as an efficient channel to thermalize the entire ensemble because they act as a bath for each other.

The second important mechanism is the scattering of off-resonant photons from the lattice and dipole trap beams. In order to perform a quantitative investigation of the role of photon scattering, the authors of [61] implemented a highly controllable measure for the scattering rate. This represents an effective implementation of dephasing due to coupling to an external bath. Concretely, photon scattering results in two processes. First, the scattering event effectively measures the position of an atom within the photon wavelength λ and therefore projects the wavefunction onto the respective lattice site with a new localization length $\lambda/2\pi$. Not only does this destroy the coherence of the many-body wavefuntion resulting in an incoherent mixture of Wannier states, it can also lead to excitations into higher bands. Due to a larger tunneling rate, atoms localized in the ground band are extended in higher-lying bands. In addition, these higher bands are typically not trapped by the external harmonic confinement and thus lead to particle loss. Moreover, in an interacting system these excitations can lead to delocalization mechanisms due to interactions between ground band and excited band atoms. Theory and experiment identify that the imbalance evolution of an open quantum system can be modeled by a stretched exponential decay $\mathcal{I} \propto e^{-(\Gamma t)^{\beta}}$ with a coupling constant Γ that depends on the photon scattering rate and a stretching exponent β [55, 57, 61].

Both effects discussed here are unavoidable in the experiment and therefore challenge some conclusions. In particular, these decay mechanisms yield a stretched exponential imbalance decay even in the many-body localized phase. The resulting finite imbalance lifetime, is recorded as a positive decay constant such that we do not expect a vanishing exponent (see sec. 2.3) in the MBL phase. Further, across the MBL phase transition the coupling effects accelerate the recorded relaxation dynamics masking potential characteristics in the subdiffusive phase. An independent study of the discussed effects is not simple since inter-tube coupling and photon scattering are strongly correlated. One may potentially reduce the coupling between the tubes by deeper orthogonal lattices, but this comes along with a larger photon scattering rate. Thus, such open system effects represent two of the main limitations of our quantum gas experiment.

2.5. MBL in systems without disorder

The preceding discussion about many-body localization and ergodicity breaking applies exclusively to systems with quenched disorder (or detuning) that explicitly break translational invariance. Hence, soon the question was considered whether robust non-ergodic phases can also exist in models without quenched disorder. In general, translational invariance in a finite system requires that any inhomogeneity with finite wavelength reminiscent of the initial state must eventually decay to zero. This is apparently in contradiction to disordered MBL systems where non-equilibrium patterns survive for infinite times. However, the characteristic decay time may potentially diverge with system size, leading to an intuitive definition of translation invariant many-body localization [69]. In a two-leg spin system composed of light and heavy spins the authors find an exponentially long decay time of an initial finite-wavelength spin modulation before ultimately diffusion sets in. The observed exponentially long sub-diffusive dynamical regime is called quasi many-body localization that is considered an intermediate regime between full MBL and diffusion. While this phase shares some common features with disordered MBL such as logarithmic entanglement growth on transient timescales, the authors cannot provide evidence that the lifetime of quasi-MBL diverges in the thermodynamic limit. Similar observations, in particular the exponentially diverging relaxation timescale, were reported in a polar Bose-Hubbard model [72].

Other works on comparable setups study localization in disorder-free systems driven by interactions and dynamical constraints due to frustration [70, 71, 73, 75]. These constraints can trap the evolution into a metastable state under certain conditions. This behavior was recently observed in an experimental study of the mass-imbalanced Fermi-Hubbard model [157] where the authors found the onset of a metastable regime for large interactions and mass imbalances. These results can also be interpreted in terms of quantum glasses [74] that exhibit self-induced localization due to dynamical constraints. Though, the respective phase does not possess an extensive set of conserved quantities which fundamentally distinguishes it from true many-body localization.

A different approach to search for non-ergodicity in systems without quenched disorder is pursued in recent studies that investigated the localization in tilted lattice models. Since the seminal work by Wannier [158] it is known that a single particle in a linear external potential exhibits Wannier-Stark localization resulting in wavefunctions with an exponential envelope (see sec. 8.1). Thus, the non-interacting conditions are comparable to disordered settings. However, in the interacting case the situation is less obvious since the potential is regular and the resulting many-body spectrum possesses many degeneracies which may prevent the emergence of stable localization. For this reason two works independently considered a modification of the purely linear potential, either a parabolic term modeling a harmonic confinement [89, 95] or a weak random disorder [96]. In the cited literature the authors investigated a model of spinless fermions with the additional type of external potential. The models are represented by the following Hamiltonians

$$\hat{H}_1 = \frac{J}{2}\sum_{i=0}^{L-2}\left(\hat{c}_i^\dagger \hat{c}_{i+1} + \text{h.c.}\right) + \sum_{i=0}^{L-1} W_i \left(\hat{n}_i - \frac{1}{2}\right) + U\sum_{i=0}^{L-2}\left(\hat{n}_i - \frac{1}{2}\right)\left(\hat{n}_{i+1} - \frac{1}{2}\right), \quad (2.11)$$

$$\hat{H}_2 = \sum_i \left[\frac{J}{2}\left(\hat{c}_i^\dagger \hat{c}_{i+1} + \text{h.c.}\right) + i \cdot \Delta \hat{n}_i + h_i \hat{n}_i + U \hat{n}_i \hat{n}_{i+1}\right]. \quad (2.12)$$

The external potential in $\hat{H}_1$ comprises the linear and parabolic part according to $W_i = -\gamma i + \alpha i^2/L^2$ with system size L and h_i in $\hat{H}_2$ denotes the random on-site disorder. Both works independently find characteristic MBL features in the respective system. This includes Poissonian level statistics, logarithmic entanglement entropy growth and a stable density imbalance plateau over long times. For historic reasons this newly discovered phase is dubbed Stark-MBL in reference to the Stark effect in an external electric field. Though, the nature of the observed non-ergodicity in the tilted models is still under active debate and the relation to traditional disorder-induced MBL is under investigation. Moreover, the behavior of the clean system without harmonic confinement or disorder raises further questions. The inconclusive scaling of level statistics or entanglement entropy is no direct evidence of ergodicity and recent developments in this field suggest that even such a system exhibits non-ergodic properties on transient timescales. The common explanation is the newly found mechanism of Hilbert space fragmentation. We revisit this field in more detail in sec. 3.2 as well as its relation to Stark MBL in secs. 3.2.3 and 9.3.1.

3. Weak ergodicity breaking: From mobility edges to Hilbert space fragmentation

As outlined in the preceding chapters, integrability and many-body localization are established ways to avoid ultimate thermalization of a closed quantum system. Though, recent advances in the field of quantum many-body systems revealed more classes of systems that cannot be allocated unequivocally to thermal or non-ergodic ensembles. Instead, they exhibit non-ergodic properties that do not originate from the established disorder-driven localization or evade thermalization on intermediate timescales due to quasiconserved quantities. Further, there are systems where it is still unknown whether they will ultimately thermalize, for example dynamically constrained systems as presented in sec. 2.5. These studies are mainly limited by finite time and system size in the underlying theory works. Fig. 3.1 summarizes a couple of currently known concepts and how they can be classified with respect to thermal, integrable and many-body localized systems. The classes covered in this thesis are highlighted in bold. In this context it is central to define the notion of weak and strong ETH as introduced in the literature. The strong version of the ETH is defined such that all eigenstates within the spectrum become thermal in the thermodynamic limit. Most generic quantum systems satisfy this condition. Contrarily, the weak version of the ETH allows for a finite number of non-thermal states throughout the spectrum as long as their ratio vanishes in the thermodynamic limit. Consequently, we consider it as weak ergodicity breaking when the strong version of ETH is violated and as strong ergodicity breaking in case even the weak version of the Eigenstate Thermalization Hypothesis no longer applies.

In the following we will discuss two of these intermediate phenomena, namely mobility edges and Hilbert space fragmentation, in more detail as they will be central for the experimental studies reported in parts III and IV. We thereby give a general review of the fundamental concepts in this chapter and go into more specific details in the respective part of this thesis.

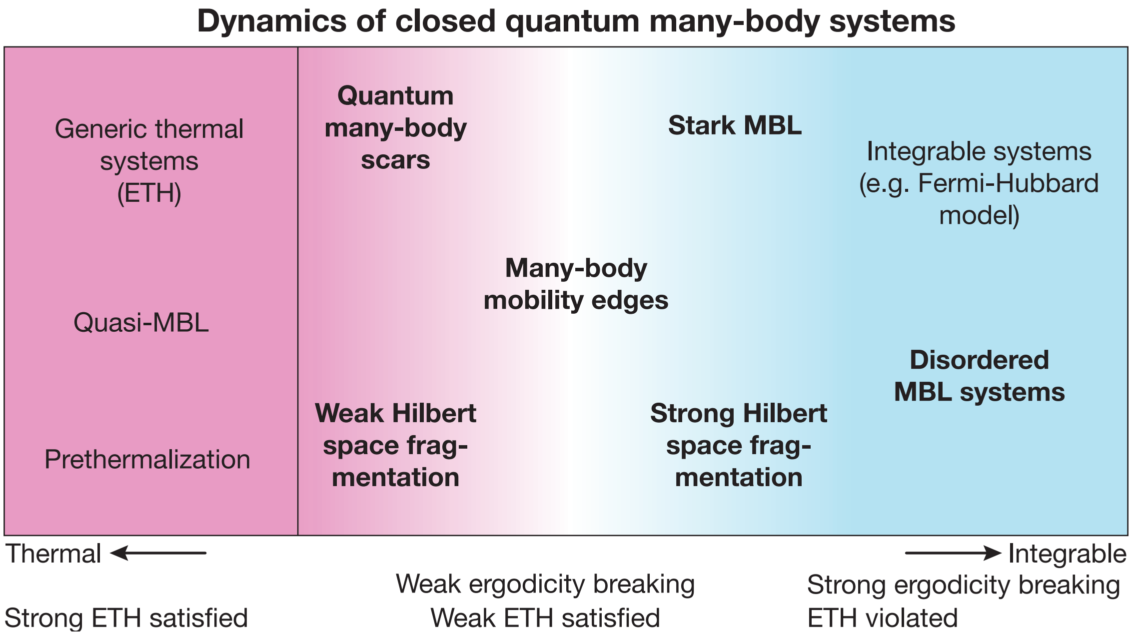

Figure 3.1.: Overview of theoretical concepts and phases: Besides thermalizing and non-ergodic localized quantum many-body systems more concepts and phases have been discovered whose behavior cannot be directly allocated to one of the preceding classes, but belong to the spectrum between these extreme cases. Concepts at least partially covered in this thesis are highlighted in bold.

3.1. Mobility edges

3.1.1. Single-particle mobility edge (SPME)

As stated previously, all eigenstates throughout the spectrum in the one-dimensional Anderson and Aubry-André model localize at a common critical disorder strength independent of their energy. However, there exists a class of models, which feature a coexistence of localized and extended eigenstates in different regions of the spectrum. The energy separating these kinds of states is called a *mobility edge*. One of the most famous models featuring a mobility edge is the three-dimensional Anderson model and this was already predicted by Anderson himself in [11]. Its phases as well as the mobility edge were even observed and characterized experimentally in [159] with a BEC near the ground state in a speckle laser field. Controlled excitations from a periodic modulation of the disorder pattern added energy to the system and lifted the BEC above the mobility edge where the extended nature of the eigenstates was detected via expansion measurements. A similar approach studied the expansion of an atomic cloud in the presence of a speckle potential and recorded localized and diffusive components belonging to states below and above the single-particle mobility edge [129, 130] without concrete energy resolution, but clearly demonstrating the presence of localized and extended components at different energies.

It should be noted that an intermediate phase with a mobility edge is expected in a generic system with quasiperiodic disorder as well as higher-dimensional systems. In the case of quasiperiodic detuning it is possible to construct one-dimensional systems with a single-particle mobility edge [160–165] that are commonly summarized under the term *generalized Aubry-André model* since they have a deterministic on-site potential, typically of the general form given by

$$\hat{V} = 2\Delta \sum_i \frac{\cos(2\pi q i + \phi)}{1 - \alpha \cos(2\pi q i + \phi)} \hat{n}_i, \tag{3.1}$$

or

$$\hat{V} = \Delta \sum_i \cos(2\pi \alpha i^n + \phi) \hat{n}_i \quad \text{with} \quad 0 < n < 1 \quad \text{and} \quad \alpha \in \mathbb{R} \setminus \mathbb{Q}. \tag{3.2}$$

Note that both models reduce to the AA model, either for $\alpha = 0$ or $n = 1$ and have a mobility edge otherwise. Though, these models are beyond direct potential experimental realizations. In [132] the authors then suggested a model with a shallow primary lattice superimposed with the quasiperiodic detuning lattice. The term shallow implies that, unlike in the AA model, the tight-binding description is not appropriate and terms of higher orders such as next-nearest neighbor hoppings have to be taken into account. This model can indeed be implemented in our experiment and is introduced in more details in sec. 6.1. Single-particle mobility edges can also be observed in other systems such as a synthetic momentum-space lattice with artificial gauge fields and engineered disorder [166].

3.1.2. Many-body mobility edge (MBME)

Much like in the single-particle case, the many-body equivalent of a mobility edge defines a critical energy separating localized and extended states in the many-body spectrum. In the canonical ensemble description this corresponds to a critical temperature of the system separating an insulating from a conducting phase. This concept was already introduced in [12] and implies that states above the critical energy are thermal and obey ETH while states below the mobility edge can be written in the LIOM framework and are close to product states. The presence of a many-body mobility edge underlines that the MBL transition is a dynamical phase transition with the eigenstate properties changing across the critical point as a function of the control parameter. In the case of disordered systems, this includes both the disorder strength as well as the energy.

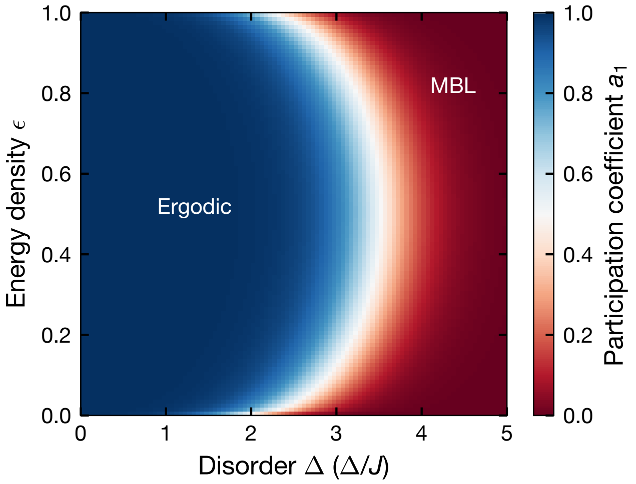

Figure 3.2.: Many-body mobility edge in the spin-1/2 Heisenberg chain: The model exhibits an ergodic and a many-body localized phase discriminated by the participation entropy volume law coefficient a_1. For intermediate disorder strengths $2 \leq h \leq 3.5$ the transition depends on the energy which is clear evidence for a mobility edge. Note that this is a schematic representation of the findings of [63] and not the result of a numerical simulation. Figure adapted from [63].

The most studied model in the context of an MBME is the isotropic spin-$1/2$ Heisenberg ladder subject to a random magnetic field [63–66] described by the Hamiltonian

$$\hat{H}_{HB} = J \sum_i \left(S_i^x S_{i+1}^x + S_i^y S_{i+1}^y + S_i^z S_{i+1}^z - h_i S_i^z \right) \tag{3.3}$$

although similar works on a transverse field quantum Ising chain [138, 167, 168] yield the same qualitative results. Note that the mobility edge found in these systems is purely induced by interactions since the corresponding non-interacting system is known to be fully localized at infinitesimal disorder strength due to Anderson localization, excluding the possibility of a single-particle mobility edge. The phase diagram of the disordered Heisenberg chain as a function of the disorder strength and eigenstate energy is illustrated in Fig. 3.2 and based on the results of [63]. This is a schematic representation of those results and not an actual computation. The numerical observable used in this case is the participation coefficient a_1 that is related to the entanglement entropy S and Hilbert space dimension $\dim \mathcal{H}$ via $S \propto a_1 \ln(\dim \mathcal{H})$. For low disorder the eigenstates are extended and thermal as reflected by the volume-law entropy scaling $S \propto \dim \mathcal{H}$ with $a_1 = 1$, conversely, all eigenstates are localized (and $a_1 \ll 1$ in accordance with an area-law) above the critical disorder strength of $h_c \geq 3.5$. Note that this is the critical point also cited in [14, 41] where a mobility edge is no longer present and the full system is supposedly many-body localized. At intermediate disorder strengths the eigentate phase transition is visibly energy-dependent with the band edges localizing at a lower critical point.

Similar works were also performed for a deterministic quasiperiodic potential of the type in Eq. (3.1) [169–173]. A major difference in this case is that the corresponding non-interacting model possesses a single-particle mobility edge. These works hence aim to explore the question whether the interacting system with an MBME can remain localized, i.e. an MBL phase can exist at infinite temperature when equally averaging over localized and extended contributions or if all states get hybridized such that the full system thermalizes. In the project reported in part III we approach this question experimentally and more details on the related theory works are given in sec. 7.1.

Note that a many-body mobility edge is not a generic feature in disordered quantum many-body systems. For instance, the Aubry-André model with on-site interactions shows no signs of an energy-dependent phase transition, neither in the single-particle model due to the self-duality, nor in the interacting case.

3.2. Hilbert space fragmentation

Another exception to strong ETH was found in kinetically constrained fracton systems. These possess elementary excitations that exhibit restricted mobility, either because they can only move in certain directions (subdimensional particles) or because their motion necessarily creates additional excitations [86]. Originally studied in three-dimensional lattice models [174, 175], and models with kinetic constraints directly imposed on the Hamiltonian [176, 177], different approaches to fractonic systems equipped with the conservation $U(1)$-charge (e.g. total magnetization) and its associated dipole moment demonstrated the localization of charge excitations. These types of systems were then studied in the context of random unitary circuits [81]. In such systems every discrete time step is governed by a local unitary gate equipped with the imposed conservation laws. In subsequent studies it was shown that three-site gates lead to long-lived localization, while longer-range interactions tend to thermalize the system [87, 88]. This observation motivated the definition of strong and weak Hilbert space fragmentation as explained in the following.

The phenomenon of Hilbert space fragmentation is illustrated in Fig. 3.3. In the presence of conservation laws the Hilbert space splits into a block-diagonal structure where every symmetry sector $\mathcal{S}$ is labeled according to the conserved quantity, in this example the dipole moment P. In a generic system all states within this sector are dynamically connected by the Hamiltonian and the system relaxes to an infinite temperature state within each symmetry sector $\mathcal{S}$ in the thermodynamic limit, provided that the available states are degenerate. However, dipole moment conservation in combination with strictly local interactions leads to further fragmentation of the symmetry sector into exponentially

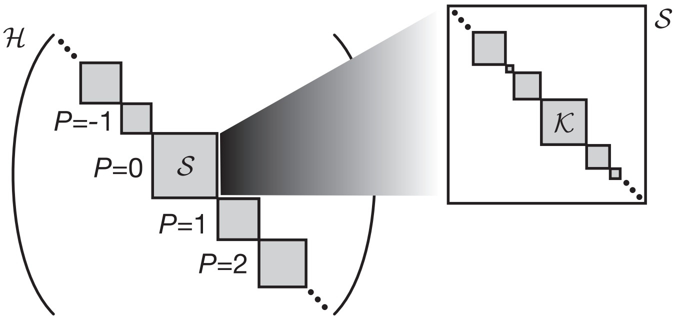

Figure 3.3.: Schematic illustration of Hilbert space fragmentation: Due to conservation laws the Hamiltonian splits into a block-diagonal structure of symmetry sectors $\mathcal{S}$. In this example $\mathcal{S}$ is uniquely defined by the dipole moment P. In the case of Hilbert space fragmentation the symmetry sectors further shatter into exponentially many dynamically disconnected fragments called Krylov sectors $\mathcal{K}$.

many subspaces that are closed under the action of the Hamiltonian and cannot be directly identified with an underlying symmetry or conserved quantity. Those Krylov subspaces $\mathcal{K}$ are defined as the set of states that are coupled under repeated action of the Hamiltonian $\hat{H}$ on the initial state $|\psi_0\rangle$: $\mathcal{K} = \text{span}\{|\psi_0\rangle, \hat{H}|\psi_0\rangle, \hat{H}^2|\psi_0\rangle, \dots\}$. Therefore, a given initial state only lives within an exponentially small section of the Hilbert space, yielding an intuitive picture for the violation of ETH and ergodicity breaking in such settings with only few conserved quantities. The conservation of dipole moment takes on experimental significance because it naturally occurs in realizable settings such as the quantum Hall effect [94, 178, 179] or a tilted optical lattice [89, 95, 96]. In these systems a leading-order effective Hamiltonian can be derived that preserves the total dipole moment exactly in the limit of infinite tilt. For the situation of finite tilt, however, the conservation laws are approximate and apply on a transient timescale where the system exhibits fragmentation before it ultimately reaches thermal equilibrium [88, 180, 181].

Another striking characteristic of fragmented systems is the strong dependence of the dynamics on the initial conditions. Consider different localized product states with the same dipole moment, thus living in the same symmetry sector, but not in the same Krylov subspace. It is now intuitive to imagine that the dynamics reflect the dimension of the sector they live in. In the most extreme case one can have a frozen state (a product eigenstate of the Hamiltonian) on one side which lives in a fully disconnected subspace with dimension one and shows no dynamical evolution. On the other side, one can start from a state living in a subspace that is almost as large as its symmetry sector leading to nearly thermal behavior. It is this smoking-gun characteristic of initial state-dependence in systems exhibiting Hilbert space fragmentation that we seek to explore experimentally in part IV. Note that this is a major difference to thermal systems where every initial state, with the exception of low-energy eigenstates, relaxes to the same equilibrium state. Further, such a behavior does not occur in MBL systems either where localization persists for all typical initial states throughout the energy spectrum. We also comment on this important distinction between fragmentation and MBL in sec. 3.2.3.

In the literature there are two distinct types of Hilbert space fragmentation, the strong and weak version [87, 88]. Their definition is based on the scaling of the fragment dimension with system size as will be explained below. The distinction of strong and weak fragmentation goes along with the violation of weak and strong ETH as defined above.

3.2.1. Strong fragmentation and violation of weak ETH

In the strongly fragmented case the system does not thermalize for any initial state and hence represents an example of strong ergodicity breaking. This violation of the weak version of ETH was studied numerically for a spin-1 chain [87] that obeys the three-site Hamiltonian

$$\hat{H}_3 = -\sum_i \left(S_i^+ (S_{i+1}^-)^2 S_{i+2}^+ + \text{h.c.}\right) \tag{3.4}$$

(in the spin-1/2 framework this can equally be formulated as $\hat{H}_{ph} = \sum_i (\hat{c}_i^\dagger \hat{c}_{i+3}^\dagger \hat{c}_{i+2} \hat{c}_{i+1} + \text{h.c.})$, typically referred to a the pair hopping or minimal model and introduced in this context by [90]). The Hamiltonian conserves the $U(1)$ charge $\hat{Q} = \sum_i S_i^z$ and its associated dipole moment $\hat{P} = \sum_i i S_i^z$. A numerical analysis of this Hamiltonian reveals non-ergodic characteristics represented by a non-thermal saturation value of the autocorrelation function, a non-thermal distribution of expectation values as well as eigenstate entanglement entropies much smaller than in an infinite temperature system.

The ergodicity-breaking behavior is referred to the dimensions of connected subspaces in a certain symmetry sector defined by the charge q and dipole moment p. The dimension of the largest connected subsector only attains an exponentially small weight compared to the full symmetry sector

$$\max_i \left(\dim(\mathcal{K}_i)\right) / \dim(\mathcal{S}_{(q,p)}) \propto \exp\left(-N\right) \tag{3.5}$$

with system size N. This exponential scaling defining strong Hilbert space fragmentation is supposed to explain the absence of thermalization in such systems and occurs, for example, in a lattice in the limit of infinite tilt. After all, strong Hilbert space fragmentation is a novel type of robust ergodicity breaking in a translation-invariant system without disorder.

3.2.2. Weak fragmentation, quantum scars and violation of strong ETH

Ergodicity can be restored when longer-range interactions are added to the original Hamiltonian. This context is investigated in the Hamiltonian

$$\hat{H} = \hat{H}_3 + \hat{H}_4 = \hat{H}_3 - \sum_i \left(S_i^+ S_{i+1}^- S_{i+2}^- S_{i+3}^+ + \text{h.c.} \right). \tag{3.6}$$

which involves four-site processes. This Hamiltonian has the same conservation laws as Eq. (3.4) and equally preserves charge and dipole moment. Like in the previous case the Hilbert space has exponentially many invariant subspaces, though the authors of [87] confirm that it exhibits dynamics in agreement with at least weak ETH. The observations include a decay of the autocorrelation function to zero in the thermodynamic limit and most eigenstates from the bulk of the distribution have a thermal entanglement entropy.

This drastic change of the system's properties upon the addition of longer-range interactions is related to the statistics of fragment dimensions. As opposed to strong fragmentation, in the weak case, the largest sector dimension approaches the size of the respective symmetry sector in the thermodynamic limit

$$\max_i \left(\dim(\mathcal{K}_i) \right) / \dim(\mathcal{S}_{(q,p)}) \xrightarrow[N \to \infty]{} 1. \tag{3.7}$$

Therefore, almost all states belong to the same subspace such that the system can thermalize within the symmetry sectors for typical initial states. There is, however, a small number of outlying eigenstates with low entanglement entropy that can evade thermalization. This is precisely the definition of weak ETH. These special states also occur in other models in the context of scarred states and are explored below.

The original incentive to study the thermalization dynamics of kinetically constrained models was triggered by the observation of unexpected, non-thermal behavior in a one-dimensional Rydberg quantum simulator [76]. It consists of an array of 51 atoms that can either be in the ground state $|g\rangle$ or excited Rydberg state $|r\rangle$ and the distance between the atoms can be freely tuned. However, Rydberg atoms interact strongly via van der Waals interactions. Consequently, two neighboring atoms cannot be in the excited state, a consequence of the well-known Rydberg blockade. This restriction makes the model kinetically constrained. When initiating the system in the high-energy state $|Z_2\rangle = |\ldots grgrg \ldots\rangle$, long-lived oscillations of the domain wall density were observed, which is in contradiction to the expected thermal relaxation. This response could not be explained in the beginning because it cannot be related to any conservation law in the system or the Rabi frequency. In order to explain this unexpected observation, the PXP-model [77, 78, 182] describing a chain of Rydberg atoms including the blockade was developed. It is described by the Hamiltonian

$$\hat{H}_{PXP} = \sum_{n=1}^{L} P_{n-1} X_n P_{n+1} \tag{3.8}$$

with the Pauli operator $X_n = |g\rangle_n \langle r|_n + |r\rangle_n \langle g|_n$ and the projectors $P_n = |g\rangle_n \langle g|_n$ which enforce the Rydberg blockade and make the model interacting. This model possesses a finite number of eigenstates that have a large overlap with the Z_2-state and can explain the observed oscillations this way. This number of special states is small such that the model belongs to a class of models with weak ergocity breaking. Those special eigenstates are also referred to as quantum scars, a description that is motivated from a classical stadium billard. There, a quantum scar has a large density in the vicinity of a classically stable orbit [182]. Up to now there have been numerous studies of quantum scars, highly-excited eigenstates with low entanglement, in various systems ranging from constrained spin chains to the tilted Fermi-Hubbard model in a special regime [79–85, 183]. Note that weak fragmentation and quantum scars are intertwined, but not the same. The occurrence of scars does not require a fragmented Hilbert space, but inversely, weakly fragmented systems exhibit such special states that belong to the context of quantum scars as reported in [87].

Overall, a prominent hallmark of weak ergodicity breaking is a strong dependence of the system's dynamics on the initial configuration [88]. While some atypical states feature a certain longevity like oscillations or transient non-thermal plateaus, most physical states are thermal and exhibit fast relaxation towards thermal equilibrium. Weak fragmentation is reminiscent of quantum scarring because there is a number of non-thermal eigenstates with low entanglement entropy in an otherwise thermal bulk such that the systems fails to thermalize for special initial states. Though, this is not too obvious, because, while the number of scar state in the PXP-model scales linearly with system size, the model in Eq. (3.6) possesses exponentially many outlying states.

3.2.3. Fragmentation and Stark MBL

The concept of MBL was originally studied for quantum many-body systems with random or quasiperiodic disorder. In this case non-thermal properties were identified resulting in a memory of the initial conditions up to infinite times. This new phase of matter is stable to small perturbations such as an external drive as well as mostly insensitive to the initial conditions. Recent work investigated a lattice model with a linear external potential (tilt) in the presence of interactions. When adding an additional term that lifts the perfectly linear tilt, either a harmonic potential [89, 95] with curvature α or weak random disorder [96], the authors identify characteristics that are identical with the typical

MBL signatures in the case of weak interactions. These include Poissonian level statistics, logarithmic growth of the entanglement entropy with time and a non-zero steady-state value of the imbalance or comparable observables. Therefore, this phase was dubbed Stark MBL. Though, a fundamental difference to common MBL systems is the absence of quenched disorder. However, the situation is less conclusive when studied for a purely linear tilt. In this case the level statistics exhibit an intermediate scaling between Poissonian and the Gaussian Orthogonal Ensemble and equally the entanglement entropy scaling neither shows thermal nor localized characteristics. Its origin can be explained by the model of two particles in a strongly tilted lattice with slope Δ much larger than the on-site interaction U. While direct hops of a single particle are suppressed due to the energy difference Δ between initial and final state, pairwise hops of two particles forming a doublon that preserve the dipole moment $P = (x_1 + x_2)/2$, where x_1 and x_2 denote the position of the particles in the lattice, are allowed given a smaller energy penalty of only $U \ll \Delta$. The effective hopping rate for this process is

$$J' \propto \frac{|J|^2}{\Delta - U} - \frac{|J|^2}{\Delta + U} = \frac{2|J|^2 U}{\Delta^2 - U^2} \approx \frac{2|J|^2 U}{\Delta^2}. \tag{3.9}$$

The two terms represent both ways to reach the final state via different virtual intermediate states and the hopping amplitudes of both processes add up. We immediately see that without interactions the amplitudes cancel and that the effective hopping amplitude is small for large tilts. Consequently, in order to cause delocalization, the weak off-diagonal hopping J' has to compete with the on-site interaction U and requires an intricate analysis of the diagonal and off-diagonal matrix elements of the Hamiltonian at higher orders in perturbation theory. Additional on-site terms such as disorder or curvature equally have to compete with the weak hopping, such that localization can be induced easily and this was observed numerically as Stark MBL. In this case the eigenstates only have a low entanglement entropy suggesting that the many-body states are a superposition of localized single-particle states reconciling with the LIOM picture constructed for disorder-induced MBL [89]. Hence, the other observations of logarithmic entanglement entropy growth or Poissonian level statistics can equally be explained this way. A recent publication [184] investigated the entanglement entropy in more detail. For a purely linear potential they find a linear growth in time and subsequent saturation to a tilt-dependent value, a clear distinction from MBL-like behavior. The linear growth is attributed to a fast resonant spread of the wavefuntion within the respective available subspace. In contrast, upon the addition of a harmonic confinement, the authors recover logarithmic entanglement growth like in disordered MBL systems and attribute this change of behavior to the removal of degeneracies in the respective sector and the breaking of dipole moment conservation.

The physics of the pure Stark model ($\alpha = 0$) can be connected to Hilbert space fragmentation. In the limit of large tilt the Stark Hamiltonian is dominated by the term $\Delta \sum_i i\hat{n}_i$, which denotes the dipole moment of the system. Hence, dipole moment is conserved and the Hilbert space is strongly fragmented according to [87, 88, 90] leading to a violation of weak ETH. In the spin language this corresponds to the minimal model referred to as the lowest order Hamiltonian $\hat{H}_3 = -J \sum_i \left(S_i^+ (S_{i+1}^-)^2 S_{i+2}^+ + \text{h.c.} \right)$ involving three consecutive sites. In the case of finite tilt, it requires higher orders in perturbation theory like $\hat{H}_4$ (Eq. 3.6) involving longer-range hopping processes. This addition was found to restore thermalization for sufficiently large admixtures of the higher-order terms. Recent numerical work even suggests [89] that the spin model $\hat{H}_3 + \epsilon \hat{H}_4$ for arbitrarily small ϵ as well as the Stark model with $\alpha = 0$ thermalize in the thermodynamic limit. Though, future work will be required to resolve this fundamental question.

The additional higher-order couplings make the system only weakly fragmented [88] where it was found that generic states exhibit thermal properties and only a vanishingly small fraction of states behave non-ergodically. Thus, localization can only persist on timescales $t_* \propto \exp\left(\Delta / J\right)$ when the leading order term applies. This behavior can be unified with the theory of prethermalization. The central theorem of this approach states that a system on intermediate times is governed by an effective Hamiltonian with approximate conservation laws that lead to restricted dynamics and temporary equilibration to a generalized Gibbs ensemble. At exponentially long times it finally relaxes to full equilibrium. Although this concept was previously studied for periodically driven Floquet systems in theory [180, 181] and experiment [185, 186], it can also be applied to static many-body systems [88]. On intermediate timescales the dynamics in the tilted lattice model are well described by the effective Hamiltonian $\hat{H}_3$ and ultimately higher orders will lead to relaxation on exponentially long times. Though, one has to discriminate this behavior carefully from thermal systems because weak fragmentation violates the strong version of ETH, but any typical state with a narrow energy distribution will ultimately thermalize.

Another striking difference between Stark MBL and conventional MBL is the strong dependence of the dynamics on the initial conditions, which suggest that the underlying mechanism leading to non-ergodicity is inherently different. In disordered systems localization comes about due to exponentially many local integrals of motion for a typical initial state and nearly independent of its energy. As observed in [29] there might occur a different energy-dependent final state, but localization prevails throughout the spectrum as long as there is no mobility edge. Conversely, in Stark MBL the behavior can be related to the fragmented Hilbert space and the domination of on-site energies over the effective hopping rate. It typically shows a strong dependence on the initial conditions that is most prominent in the case of weak fragmentation and can be related to the shattered Hilbert space structure and fragment dimensions. Finally, recent numerics suggest that there are no signs of a phase transition from an ergodic to a localized phase [91]. These insights are based on the fact that the Hilbert space is fragmented such that strong ETH is never satisfied. Instead, the authors introduce a quasi-ergodic phase that possesses large ergodic grains with ETH-like observables that can exceed the system size in numerical works, but this argument does not apply to the thermodynamic limit. Moreover, the late time dynamics depend on the initial state given the existence of outlying non-thermal states. This is in contradiction to the statement of ETH. Earlier works suggested the existence of a phase transition at finite tilt [96], but the authors admit that they cannot disprove a potential nonergodic phase at lower tilt. Most likely they were unable to distinguish the quasiergodic phase from true ergodic characteristics. The prerequisites of a model exhibiting Hilbert space fragmentation can be implemented in our fermionic quantum gas experiment. All details will be explained in part IV.

Part II.

Experimental setup and techniques

Quantum simulators with ultracold atoms in optical lattices are nowadays a ubiquitous experimental platform to implement lattice models like the Bose- or Fermi-Hubbard model and to explore quantum systems far from equilibrium in one, two or three dimensions. These setups have been constantly evolving and even enable real-time investigations of dynamical processes in solid state and condensed matter systems with access to global and local observables including entanglement entropy, n-point correlators or the resolution of many-body level statistics. In this part we introduce our experimental system that employs ultracold ^{40}K-atoms cooled to quantum degeneracy in an optical lattice to realize the 1D Fermi-Hubbard model. Further, we explain our experimental techniques and observables used to explore non-ergodic dynamics in disordered and tilted optical lattices.

4. Experimental setup

In this chapter the experimental system with the cooling scheme and lattice setup is briefly described in the beginning before reviewing the central properties of the one-dimensional Fermi-Hubbard model. Finally, the technique of RF and microwave spectroscopy, employed in the second thesis project, are introduced, in particular the newly developed Potassium-microwave device.

4.1. A degenerate gas of ^{40}K

All experiments reported in this thesis are performed with the fermionic Potassium isotope ^{40}K cooled to quantum degeneracy and loaded into a three-dimensional optical lattice. In this chapter only a brief overview of the experimental setup and techniques is given while more detailed information can be found in preceding PhD theses carried out at this experiment [187–189].

The cooling sequence begins with capturing ^{40}K and bosonic ^{87}Rb in a dual-species magneto-optical trap (MOT) followed by Doppler cooling in an optical molasses. After magnetic transport from the MOT chamber to the science cell through a differential pumping section, the sample is forcedly RF-evaporated in a plugged quadrupole trap. This process mostly evaporates Rb while the K-atoms are primarily cooled sympathetically. At this stage of the sequence we have about 2×10^5 K and 2×10^6 Rb atoms at temperatures of few microkelvin. After this intermediate step the atoms are loaded into a three-dimensional crossed dipole trap where the evaporation process continues. At low temperatures the s-wave scattering cross section of fermions in the same state tends to zero, but evaporative cooling requires thermalization of the sample by energy exchange via scattering processes between the particles. Hence, fermions cannot be cooled efficiently to ultracold temperatures. Instead, we cool it sympathetically via the Rb. This way we can simultaneously cool K to quantum degeneracy and Rb well below the critical temperature such that it forms a Bose-Einstein condensate with a negligible thermal fraction below the detection limit. At the end of the sequence the Rb is removed from the trap by lowering the trap bottom such that the Rb atoms, which have about twice the mass of K, can no longer be held against gravity. The Potassium atoms are prepared in the lowest magnetic hyperfine state $m_F = -9/2$ of the ground state hyperfine manifold $F = 9/2$ (see [190] for a full documentation of the relevant Potassium properties). Unwanted components are removed via interspecies Feshbach resonances between K and Rb during the cooling process, inducing strong losses via three-body interactions. In order to generate an interacting ensemble, a second component is required. This additional $m_F = -7/2$-component is generated from the spin-polarized sample by a Landau-Zener sweep (see sec. 4.4.1). This way we can generate arbitrary mixing ratios although we typically use an equal mixture of both states. At the end of the sequence we obtain about 60×10^3 atoms with a temperature around $0.15 T_F$, where T_F denotes the Fermi temperature. It is determined via a Fermi-Dirac fit to the cloud density profile after time-of-flight.

The dipole trap beams at a wavelength of 1064 nm generate a trapping potential wherein the evaporation is performed by sequentially lowering the trap depth and thereby losing the most energetic atoms. The geometry of the horizontal traps is elliptical with a horizontal elongation of about 300 µm and a vertical diameter of 30 µm. The horizontal confinement is thus much stronger such that the atoms are supported against gravity while the density of the cloud is set by the weaker vertical confinement so as to avoid losses from three-body collisions. The horizontal confinement is instead dominated by the vertical trapping beam with circular shape and a diameter of 150 µm.

4.2. Optical lattices

4.2.1. General setup

Since the projects described in this thesis are realized in different lattice setups, their commonalities are presented here, while the individual details of the experimental realization are addressed in the respective chapter describing the particular project.

All experiments of this thesis are carried out in a three-dimensional lattice geometry generated by three orthogonal retro-reflected laser beams. This results in a standing wave pattern along all three axes and the atoms are attracted to the intensity minima or maxima of the standing wave, depending on the detuning with respect to the atomic transition. All laser beams forming the optical lattices have roughly the same geometry, the atoms are located in the focus of a Gaussian laser beam with a diameter of about 150 µm. The primary lattice along the x-axis with the wavelength $\lambda_p = 532\,\mathrm{nm}$ is generated by a Verdi V18, a frequency-doubled diode-pumped YAG laser with an output power of 18 W. All one-dimensional experiments in this thesis are conducted along this lattice axis. The orthogonal lattices along y and z with $\lambda_\perp = 738\,\mathrm{nm}$ are generated by a Titanium-Sapphire laser with a maximum output power above 4 W pumped by a Verdi V18. The polarization of the orthogonal lattice beams are chosen perpendicular to each other and in addition to a frequency offset of about 160 MHz such that the lattices do not interfere and the lattice is purely rectangular. The models simulated in this experimental setup and reported in this thesis are one-dimensional. In order to realize this condition, the tunneling element along the primary axis has to be much larger than along the vertical directions, such that the dynamics are confined to the primary lattice over a certain timescale. This goal is achieved by employing very deep orthogonal lattices between $40E_r$ and $55E_r$ such that the tunneling time ratio between primary and orthogonal lattice ranges from about 5×10^{-4} to 2×10^{-3}, dependent on the particular choice of primary lattice depth. Thus, our system consists of one-dimensional tubes that are dynamically decoupled on a timescale of few hundred tunneling times according to the given tunneling ratios.

We further have a long lattice along the x-axis at twice the wavelength of the primary lattice, so $\lambda_l = 1064\,\mathrm{nm}$. Superimposed with the primary lattice this results in double-wells whose relative phase sets the energy difference between the left and right site. Given the boundary condition of having a node at the retro-reflecting mirror, the phase between both lattices is set by the wavelength and hence small changes in the frequency of one of the lattices enable an arbitrary control of the relative phase. The Nufern, a fiber laser with an output power on the order of 10 W is referenced to a temperature-stabilized Fabry-Pérot cavity and the Verdi generating the primary lattice is stabilized to that reference via a beat-offset lock. Together these two lattices form the superlattice which is employed in the initial state preparation and final state readout. The high controllability of the superlattice phase thereby plays a crucial role for the fidelity of the initial state as well as for the imbalance readout (see sec. 5.1). Further, a strongly tilted superlattice freezes the dynamics before and after time evolution because the achievable inter- and intrawell couplings get much smaller than what could be reached with a deep primary lattice alone.

Except of the long lattice required for the superlattice, all lattices are blue-detuned with respect to the atomic transition at 766.7 nm. This is advantageous because it can compensate for the harmonic confinement induced by the dipole traps. In particular, along the vertical z-axis the red-detuned dipole trap and the blue-detuned lattice have approximately the same geometry such that the confinement can be nearly compensated and a homogeneous potential landscape can be created up to leading order. This is an experimentally relevant factor and was successfully employed in [117, 119, 126]. Moreover, the confinement during lattice loading is tunable via the dipole trap intensity, which is important for the atomic density distribution in the lattice (see sec. 9.2.2).

Along the primary lattice axis we employ a quasiperiodic potential generated by an additional lattice with incommensurate wavelength ratio or a linear tilt. Details on the precise realization can be found in the respective part of this thesis reporting on the related experimental projects in secs. 7.2.2 and 8.2.

4.2.2. Lattice loading

After evaporative cooling to quantum degeneracy the degenerate Fermi gas is loaded into the three-dimensional lattice in a series of linear ramps. The goal of the procedure is to be as adiabatic as possible in order to avoid heating the gas during the loading process and thus achieve lowest entropies in the lattice. Entropy and temperature define the density and particle distribution in the initial state. In an independent measurement we verified that upon non-interacting loading the temperature only changes slightly such that the final temperature in the dipole trap corresponds closely to the temperature in the lattice. While holding the gas in the dipole trap, the long lattice along the primary axis and the orthogonal lattices are ramped to a depth of $1E_r$, here $E_{ri} = \hbar^2/(2m\lambda_i^2)$ defines the recoil energy of the respective lattice $i \in \{s, l, \perp\}$ with wavelength λ and m denotes the atomic mass of ^{40}K. At this depth the lattice is held for 100 ms while the horizontal confinement is linearly increased via the vertical dipole trap. Since the tunneling element in such a shallow lattice is still large, the atoms can react to the changing external confinement such that the final particle distribution can be controlled in this step. After the wait time, the lattices are ramped in two linear steps of 75 ms and 20 ms to their final values ($20E_{rl}$ for the long lattice and between $36E_{r\perp}$ and $55E_{r\perp}$ in case of the orthogonal lattices) freezing the dynamics on timescales of the experiment and thereby fixing the initial state for the subsequent dynamical studies. After another wait time of 6 ms the primary lattice is switched on fast to its maximal depth of $18E_{rs}$ within 100 µs with a fixed superlattice phase such that strongly tilted double wells are generated. The strong potential offset between the left and right well ensures that the particles are exclusively located in the lower well. When the long lattice if finally ramped off before time evolution, every second site of the primary lattice is occupied. This is the charge-density wave initial state used in most of the experiments reported here.

In particular for the project on Hilbert space fragmentation the initial state distribution plays an important role for the observability of the expected signal. Therefore a detailed investigation was conducted which is presented in sec. 9.2.2 and the experimental techniques are elaborated in 5.3.

4.3. Fermi-Hubbard model and interactions

Due to the Pauli blockade, fermions have a vanishing s-wave scattering cross section at ultracold temperatures such that two atoms in the same state cannot interact. In order to enable interactions in the optical lattices, at least two different spin components are necessary. We realize this by preparing the atoms in two magnetic hyperfine states of the lowest hyperfine manifold that will be referred to as $|\downarrow\rangle \equiv |F = 9/2, m_F = -9/2\rangle$ and $|\uparrow\rangle \equiv |F = 9/2, m_F = -7/2\rangle$. This setting is described by the following Hamiltonian in second quantization [191]

$$\hat{H}_F = \int \sum_\sigma \hat{\psi}_\sigma^\dagger \left(-\frac{\hbar^2}{2m}\nabla^2 + V(\vec{r}) \right) \hat{\psi}_\sigma d\vec{r} + g \int (\hat{\psi}_\downarrow^\dagger \hat{\psi}_\uparrow^\dagger \hat{\psi}_\uparrow \hat{\psi}_\downarrow) d\vec{r} \tag{4.1}$$

in terms of the fermionic field annihilation (and creation) operators $\hat{\psi}^{(\dagger)}$. Herein $\sigma \in \{\downarrow, \uparrow\}$ denotes the spin, V is a generic external potential such as harmonic confinement or a lattice and the interaction parameter $g = 4\pi\hbar^2 a/m$. m is the mass of the atoms and a is the s-wave scattering length between opposite spins. In a lattice setup the Hamiltonian in Eq. (4.1) can be transformed in terms of the tight-binding approximation, i.e. only taking the lowest band into consideration and expanding the Bloch functions in terms of localized Wannier functions. The transformed Hamiltonian results in the well-known Fermi-Hubbard model

$$\hat{H}_{FH} = -J \sum_{i,\sigma} (\hat{c}_{i,\sigma}^\dagger \hat{c}_{i+1,\sigma} + \text{h.c.}) + U \sum_i \hat{n}_{i,\uparrow} \hat{n}_{i,\downarrow} + \sum_{i,\sigma} \mu_{i,\sigma} \hat{n}_{i,\sigma} \tag{4.2}$$

with the sum running over all lattice sites i and spins σ. The important Hubbard parameters are the tunneling element J between neighboring lattice sites and the interaction strength

$$U = \frac{4\pi\hbar^2 a}{m} \int |w(\vec{r})|^4 d\vec{r}. \tag{4.3}$$

Herein, $w(\vec{r})$ is the Wannier function centered around position $\vec{r}$. $\mu_{i,\sigma}$ denotes the external chemical potential from above. It can be of general form such as a harmonic confinement due to an external trapping potential, but also disorder or a linear tilt. The latter two cases are realized and investigated in the projects reported in this thesis.

This is the most commonly used model in the context of condensed matter physics and also applies to our experiment with ultracold fermions in optical lattices. Originally formulated by Hubbard [7] in the 1960s to describe electrons in transition metals, it soon gained major significance in the context of condensed matter physics and quantum simulation. One such development was the demonstration that the Hubbard model can be employed to explain the emergence of high-T_c superconductivity in cuprate materials [192]. Current

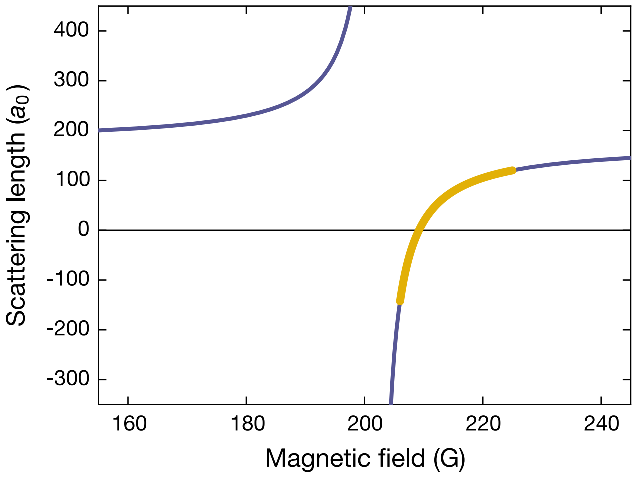

Figure 4.1.: Feshbach resonance in ^{40}K: Scattering length between the spin components $|\uparrow\rangle$ and $|\downarrow\rangle$ as a function of the magnetic field. The Feshbach resonance is centered around 202.1 G. The highlighted region marks the regular range of operation, accessing attractive and repulsive scattering lengths and in particular the non-interacting point at 209.2 G.

progress includes the exploration of the cuprate phase diagram including bad metals [114] and the pseudogap phase.

The interaction strength in the Fermi-Hubbard model can be tuned experimentally via a Feshbach resonance [102] between the spin states $|\uparrow\rangle$ and $|\downarrow\rangle$ given by the characteristic dependence of the scattering length a in units of the Bohr radius a_0 on the magnetic field amplitude B

$$a(B) = a_{bg}\left(1 - \frac{\Delta B}{B - B_0}\right). \tag{4.4}$$

The resonance is centered around $B_0 = 202.1\,\mathrm{G}$, has a width of $\Delta B = 7.1(1)\,\mathrm{G}$ and a background scattering length $a_{bg} = 174a_0$ [193, 194], the functional form is plotted in Fig. 4.1. We typically operate in the highlighted region of the magnetic field above the resonance because on this arm we have a zero-crossing point where the sample can be made non-interacting and further we can access attractive and repulsive interactions. Dependent on the primary lattice depth, we can access the range $-20J \leq U \leq 20J$. If we move too close to the resonance, strong interactions lead to atom number losses due to inelastic collisions, however, the available range is typically sufficient to realize the hard-core limit. In this limit ($U \to \pm\infty$) no higher occupancies can be formed due to an infinite energy cost and conversely, no dynamical decay of a doublon is allowed. The resulting Hilbert space without doublons is thus closed under time evolution. In the case of an initial state without doublons, this setting maps to a model of spinless fermions such that there is an exact symmetry between $U = 0$ and $U = \pm\infty$ [133]. Contrarily, in the presence of doublons such a mapping does not exist lifting this symmetry. Moreover, the

Fermi-Hubbard model possesses a dynamical symmetry between attractive and repulsive interactions [195] that also holds in the presence of a tilt or disorder as well as for the Bose-Hubbard model.

4.4. Radio-frequency (RF) and microwave (MW) operations

In our experiment we have excellent control over the Hubbard parameters in the Hamiltonian in Eq. (4.2). While the tunneling J is defined by the primary lattice depth, the on-site interaction strength U is set by the scattering length via the Feshbach resonance and the chemical potential comprises the external trap as well as other potential sources. Moreover, we are in the position to manipulate the internal electronic states of the atoms via RF and microwave operations. These enable us to retrieve state-selective information of a given quantum many-body state in the optical lattice as will be explained in sec. 5.3. In the following we explain the methods behind these state manipulations that employ spectroscopic techniques.

4.4.1. RF spectroscopy

State manipulations between different magnetic hyperfine states m_F within the same hyperfine manifold F are driven by RF-transitions with typical frequencies ranging from 1 MHz to 60 MHz in our experiment. We have two methods available to drive the respective transition, which differ in the available resolution and fidelity.

Landau-Zener sweeps

In a Landau-Zener sweep, the frequency is continuously tuned across the resonance and hence across the avoided crossing between two energy levels. In this case the probability of excitation is given by the celebrated Landau-Zener equation

$$P_e = 1 - e^{-2\Omega^2/\dot{\Delta}} \tag{4.5}$$

with the Rabi frequency Ω and the Landau velocity $\dot{\Delta}$, which defines the rate of change of the detuning across the resonance. If the time scale is sufficiently adiabatic with respect to the coupling strength, one can obtain almost perfect state transfer. In the experiment we typically remain with the unwanted spin state component below the resolution limit such that the transfer efficiency is above 98 %. The main advantage of a Landau-Zener sweep is the nearly perfect fidelity and its insensitivity to external noise sources due to the wide range of the frequency sweep. On the other hand, for high-resolution spectroscopy, sweeps are unsuited due to their comparatively large spectral width (typically 100 kHz to 1 MHz).

Rabi pulses

The second option to change the internal state is via Rabi oscillations in a resonant RF-field. After the duration of a π-pulse $T_\pi = \pi/\Omega$ the state is entirely transferred in theory. We employ this method due to the high frequency resolution given by $1/T_\pi$, which is the main advantage over a Landau-Zener sweep. On the other hand this method is very sensitive to external noise sources such as magnetic field fluctuations since this moves the transition temporarily out of resonance and reduces the excitation probability. In our experiment we can observe coherent Rabi oscillations on timescales up to 300 µs before they dephase, setting an upper limit for applicable pulse durations. In order to be most insensitive to fluctuations in the excitation probability, we employ π-pulses with about 60 µs duration such that our spectral resolution is on the order of 17 kHz.

4.4.2. The Potassium microwave setup

As a part of this thesis project, a new Potassium microwave setup was developed and this section is supposed to give a detailed sketch of the electronics and physical setup. The device is designed to induce transitions between the $F = 9/2$ and $F = 7/2$ ground state hyperfine manifolds in the presence of a magnetic field in the region of 209 G, the usual working point near the Feshbach resonance of the mainly employed spin components $|\uparrow\rangle$ and $|\downarrow\rangle$. Fig. 4.2a depicts the level structure in the ground state in the presence of a magnetic field and Fig. 4.2b displays the transition frequency between the most relevant states. Transitions that can be induced require that $\Delta m_F = +1$ (σ^+) due to the dipole selection rules. In the Paschen-Back regime at strong magnetic fields dipolar transitions strictly require that $\Delta m_J = \pm 1$ and $\Delta m_I = 0$. Although a magnetic field around 209 G does not yet define the Paschen-Back regime, we clearly note that only the σ^+-transitions plotted in Fig. 4.2b can be excited with high fidelity while π- and σ^--transitions are strongly suppressed.

The microwave setup can take up to four different MW input signals and corresponding TTL triggers. The MW channels are switched by a broadband RF-switch (ZSWA-4-30DR+ from Mini Circuits) and the related designed logic electronic circuit. In order to achieve sufficient isolation between the input and final output, another switch (SR-V800-2S, UMCC) is inserted before the first amplifier, suppressing the signal at least by another 50 dB when

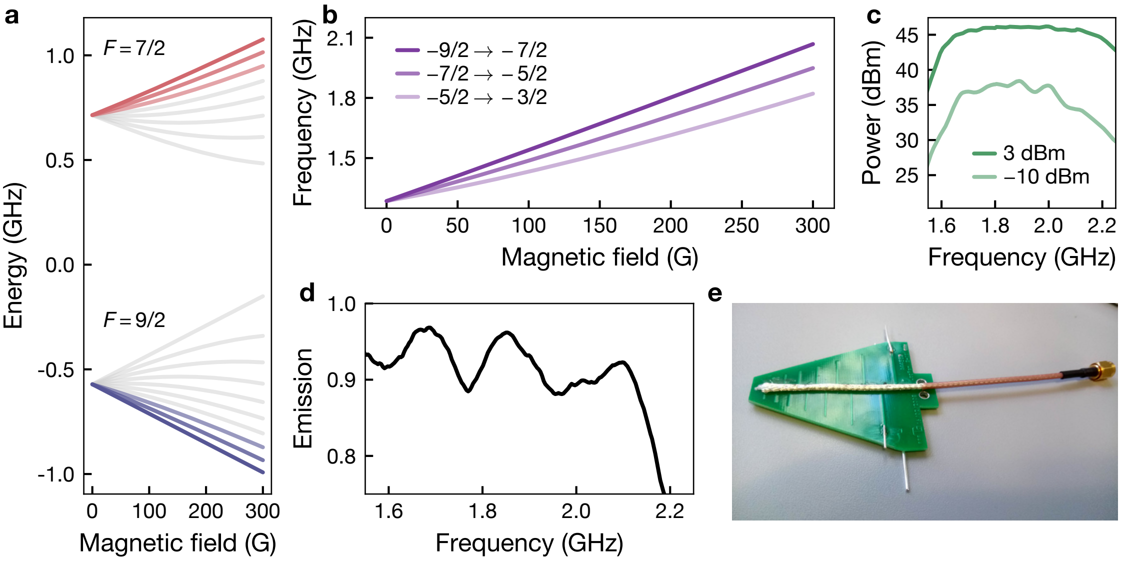

Figure 4.2.: Properties of the K-Microwave setup: a Level spectrum of ^{40}K in the ground state with two hyperfine manifolds. The relevant magnetic hyperfine states for the experiment are highlighted in color while the other states are shaded in gray. **b** Transition frequencies between the indicated states as a function of the external magnetic field. We typically operate around 209 G. **c** Power emission of the MW setup for two different input power levels. The maximal output power clearly saturates around 46 dBm. **d** Emission spectrum of the antenna across the anticipated frequency range. **e** Photograph of the log-periodic MW-antenna.

the switch is closed such that unwanted signals are suppressed below the detectable noise level. Otherwise transitions could be induced accidentally. The MW signal then proceeds to the pre-amplifier (KU LNA BB 1522 A, Kuhne Electronic) which amplifies the signal to a maximal power of 20 dBm. Afterwards, the main amplifier (KUPA 170220-30A, Kuhne Electronic) further amplifies to a maximal power level of 48 dBm within the specified frequency range. Finally, a circulator (E10-1FFF, Aerotek) protects the main amplifier from damage due to back reflections. This is very likely to happen when the antenna is not perfectly impedance matched. The maximum MW power measured at the output of the device was 46 dBm corresponding to about 40 W. Given the maximum power ratings of the RF components, the input power level should not exceed 3 dBm. A detailed study of the power ratings is depicted in Fig. 4.2c for two different input power levels. Below the saturation of the amplifiers, the maximal total amplification of the device is about 47 dB. The frequency range is primarily limited by the main amplifier, which is rated between 1.7 GHz and 2.2 GHz. Outside this range lower peak powers and perhaps other limitations have to be tolerated.

The antenna is based on a log-periodic design with manual modifications, the longest rods are elongated in order the extend the emission spectrum to lower frequencies. Its performance was quantified by measuring the reflections as a function of the frequency with a network analyzer. This data is shown in Fig. 4.2d together with a photo of the antenna in Fig. 4.2e as implemented in the experiment. Over the aspired frequency range the antenna emits at least 90 % of the power and is therefore well suited for this application.

As mentioned above, we can observe coherent Rabi oscillations on RF transitions for few hundred microseconds before external noise sources decohere the dynamics. In order to induce the oscillations for our microwave transitions, the magnetic field stability of our power supply is insufficient though. The reason lies in the sensitivity of the transition frequency to magnetic field fluctuations, i.e. the shift of the resonance as a function of the magnetic field strength. In [196] an equation for the decoherence time of Rabi oscillations was derived based on the coupling strength (or Rabi frequency) Ω_0 and the detuning induced by the magnetic field fluctuations Δ_N and it scales approximately as $t_{dec} \approx 4\pi\Omega_0/\Delta_N^2$. The RF transition $|\uparrow\rangle \leftrightarrow |\downarrow\rangle$ has a sensitivity of 153 Hz/mG, while the MW-transition $|F = 9/2, m_F = -9/2\rangle \rightarrow |F = 7/2, m_F = -7/2\rangle$ is almost twenty times more sensitive with 2.6 kHz/mG. This results in coherence times which are about 100 times shorter than for RF transition and this is indeed observed experimentally. Thus, we can only induce sweeps with the microwave setup, but this is sufficient for our purposes, although it requires more sophisticated designs of the respective sequence.

4.4.3. RF dressing

Not only can we use RF spectroscopy to induce transitions between different spin states, we further employ a new technique exploiting a resonant field to manipulate the dynamics in the optical lattice. Due to our generation of the tilt via a magnetic field gradient (see sec. 8.2), the spin states encoded in different magnetic hyperfine states see a state-dependent potential with slopes $\Delta_\downarrow$ and $\Delta_\uparrow$. This can have drastic consequences for the dynamics in the lattice since there are no proper resonances given a ubiquitous energy mismatch $|\Delta_\downarrow - \Delta_\uparrow|$. However, we can use a resonant RF field coupling the states to compensate this tilt difference as previously demonstrated in [197]. We consider the atoms as two-level systems described by the Hamiltonian $\hat{H}_A$ and with the ground state $|\downarrow\rangle$ and excited state $|\uparrow\rangle$. In the presence of an external field $\hat{H}_R$ coupling the states, the system's eigenstates can be recast in terms of the dressed states, the eigenstates of the new Hamiltonian $\hat{H} = \hat{H}_A + \hat{H}_R + \hat{H}_I$, wherein the last term describes the atom-light interaction. The central parameters of the coupled system are the resonant Rabi frequency Ω_0, the detuning δ from resonance as well as the generalized Rabi frequency

$\Omega = \sqrt{\Omega_0^2 + \delta^2}$. The dressed creation operators are defined as

$$\begin{aligned}\hat{\hat{c}}^\dagger_{i,\uparrow} &= \cos\left(\frac{\theta}{2}\right) e^{i\phi/2}\hat{c}^\dagger_{i,\uparrow} - \sin\left(\frac{\theta}{2}\right) e^{i\phi/2}\hat{c}^\dagger_{i,\downarrow} \\ \hat{\hat{c}}^\dagger_{i,\downarrow} &= \sin\left(\frac{\theta}{2}\right) e^{-i\phi/2}\hat{c}^\dagger_{i,\uparrow} + \cos\left(\frac{\theta}{2}\right) e^{-i\phi/2}\hat{c}^\dagger_{i,\downarrow}\end{aligned} \tag{4.6}$$

where $\tan(\theta) = \Omega_0/\delta$ and ϕ is the phase of the driving field. Similarly, one can express the time evolution of the original creation operators by applying the unitary operator and obtains

$$\begin{aligned}\hat{c}^\dagger_{i,\uparrow}(t) =& e^{i\Omega t/2}\cos\left(\frac{\theta}{2}\right) e^{-i\phi/2}\hat{\hat{c}}^\dagger_{i,\uparrow} + e^{-i\Omega t/2}\sin\left(\frac{\theta}{2}\right) e^{i\phi/2}\hat{\hat{c}}^\dagger_{i,\downarrow} \\ \hat{c}^\dagger_{i,\downarrow}(t) =& -e^{i\Omega t/2}\sin\left(\frac{\theta}{2}\right) e^{-i\phi/2}\hat{\hat{c}}^\dagger_{i,\uparrow} + e^{-i\Omega t/2}\cos\left(\frac{\theta}{2}\right) e^{i\phi/2}\hat{\hat{c}}^\dagger_{i,\downarrow}.\end{aligned} \tag{4.7}$$

The technique of RF dressing is employed to compensate the tilt difference induced by the magnetic field gradient in the project on Hilbert space fragmentation reported in part IV. Therein we study the tilted Fermi-Hubbard model (see chapter 8 for a detailed discussion of the model) described by the Hamiltonian

$$\hat{H} = -J\sum_{i,\sigma}(\hat{c}^\dagger_{i+1,\sigma}\hat{c}_{i,\sigma} + \text{h.c.}) + U\sum_i \hat{n}_{i,\uparrow}\hat{n}_{i,\downarrow} + \sum_{i,\sigma}\Delta_\sigma i\hat{n}_{i,\sigma} \tag{4.8}$$

with the spin-dependent tilt Δ_σ and the number operators $\hat{n}_i = \hat{c}^\dagger_i\hat{c}_i$. In order to compute the transformation of this Hamiltonian in the basis of the dressed states, the new creation and annihilation operators according to Eq. (4.7) have to be inserted into the Fermi-Hubbard Hamiltonian (Eq. 4.8). One finds that the kinetic and interacting part are invariant under this transformation. In particular the latter is useful in the experiment as it allows us to use the Feshbach resonance (see sec. 4.3) between the states $|\downarrow\rangle$ and $|\uparrow\rangle$ to set the interactions between dressed states [198]. The last term including the spin-dependent tilt transforms as

$$\begin{aligned}\Delta_\uparrow\hat{c}^\dagger_{i,\uparrow}(t)\hat{c}_{i,\uparrow}(t) + \Delta_\downarrow\hat{c}^\dagger_{i,\downarrow}(t)\hat{c}_{i,\downarrow}(t) =& \left(\Delta_\uparrow\cos^2(\theta/2) + \Delta_\downarrow\sin^2(\theta/2)\right)\hat{\hat{c}}^\dagger_{i,\uparrow}\hat{\hat{c}}_{i,\uparrow} \\ &+ \left(\Delta_\downarrow\cos^2(\theta/2) + \Delta_\uparrow\sin^2(\theta/2)\right)\hat{\hat{c}}^\dagger_{i,\downarrow}\hat{\hat{c}}_{i,\downarrow} \\ &+ (\Delta_\uparrow - \Delta_\downarrow)\cos(\theta/2)\sin(\theta/2)e^{i(\Omega t-\phi)}\hat{\hat{c}}^\dagger_{i,\uparrow}\hat{\hat{c}}_{i,\downarrow} \\ &+ (\Delta_\uparrow - \Delta_\downarrow)\cos(\theta/2)\sin(\theta/2)e^{-i(\Omega t-\phi)}\hat{\hat{c}}^\dagger_{i,\downarrow}\hat{\hat{c}}_{i,\uparrow}.\end{aligned} \tag{4.9}$$

The last two terms of Eq. (4.9) are time-dependent, but due to magnetic field fluctuations the generalized Rabi frequency Ω varies and those terms vanish for $\Omega \gg \Delta_\downarrow, \Delta_\uparrow$. The tilts seen by the dressed states can be directly identified from the first two terms. From this insight we can readily compute the tilt difference in the dressed basis to become

$$\begin{aligned}
\tilde{\Delta}_\downarrow - \tilde{\Delta}_\uparrow &= \Delta_\uparrow \left(\sin^2(\theta/2) - \cos^2(\theta/2)\right) - \Delta_\downarrow \left(\sin^2(\theta/2) - \cos^2(\theta/2)\right) && (4.10)\\
&= -\Delta_\uparrow \cos(\theta) + \Delta_\downarrow \cos(\theta) && (4.11)\\
&= \begin{cases} -\Delta_\uparrow \dfrac{1}{\sqrt{1+\tan^2(\theta)}} + \Delta_\downarrow \dfrac{1}{\sqrt{1+\tan^2(\theta)}} & (\delta > 0) \\ \Delta_\uparrow \dfrac{1}{\sqrt{1+\tan^2(\theta)}} - \Delta_\downarrow \dfrac{1}{\sqrt{1+\tan^2(\theta)}} & (\delta < 0) \end{cases} && (4.12)\\
&= (\Delta_\downarrow - \Delta_\uparrow) \frac{|\delta|}{\sqrt{\delta^2 + \Omega_0^2}}. && (4.13)
\end{aligned}$$

In order to measure the resonant Rabi frequency Ω_0 we record Rabi oscillations between the spin states and extract the frequency as a function of the applied RF power. The measured excitation fraction is fitted with the equation $|c_\uparrow(t)|^2 = \sin^2(\Omega_0 t/2)$ and an exemplary data set is shown in the inset of Fig. 4.3c together with the analytical fit. Due to the mentioned magnetic field fluctuations the Rabi oscillations dephase on timescales on the order of 500 µs.

We directly measure the tilt seen by the dressed states recording Bloch oscillations of the imbalance (see secs. 5.1 and 8.1) in the absence of interactions, which can be seen in a linearly tilted optical lattice at early times before they dephase due to inhomogeneities in the potential [117]. The frequency of these oscillations directly represents the tilt. Extracting the time evolution of the spin-resolved imbalance (see sec. 5.1.2) we obtain the oscillation frequencies from an analytical fit to the data points with the function

$$\mathcal{I}_\sigma(t) = \exp\left(-t/\tau\right) \cdot \mathcal{J}_0 \left(\frac{8J}{\tilde{\Delta}_\sigma} \cdot \sin\bigl(\pi \tilde{\Delta}_\sigma t/h\bigr) \right) \qquad (4.14)$$

based on the results presented in [117]. The first part is an exponential envelope with decay time τ mimicking the dephasing while the Bessel function of the first kind $\mathcal{J}_0$ represents the analytical equation for an ideal system. The recorded oscillations are presented in Fig. 4.3. Without RF dressing the spin components clearly exhibit a notable tilt difference (see Fig. 4.3b) originating from the different magnetic moments of the two spin states. Conversely, this difference can be almost perfectly compensated with the maximal dressing power corresponding to a Rabi frequency of $\Omega_0 = 85(1)$ kHz as shown in Fig. 4.3a.

Due to the magnetic field gradient the resonance frequency is spatially dependent inducing a detuning δ that varies across the lattice. We find that we can describe the experimentally obtained relative tilt difference $\delta\Delta = (\tilde{\Delta}_\downarrow - \tilde{\Delta}_\uparrow)/\tilde{\Delta}_\downarrow$ as a function of the Rabi frequency with a single average detuning as illustrated in Fig. 4.3c. From a fit of Eq. (4.13) to the data points we extract an average detuning of $\delta = 6.5(2)$ kHz. One can develop an intuitive

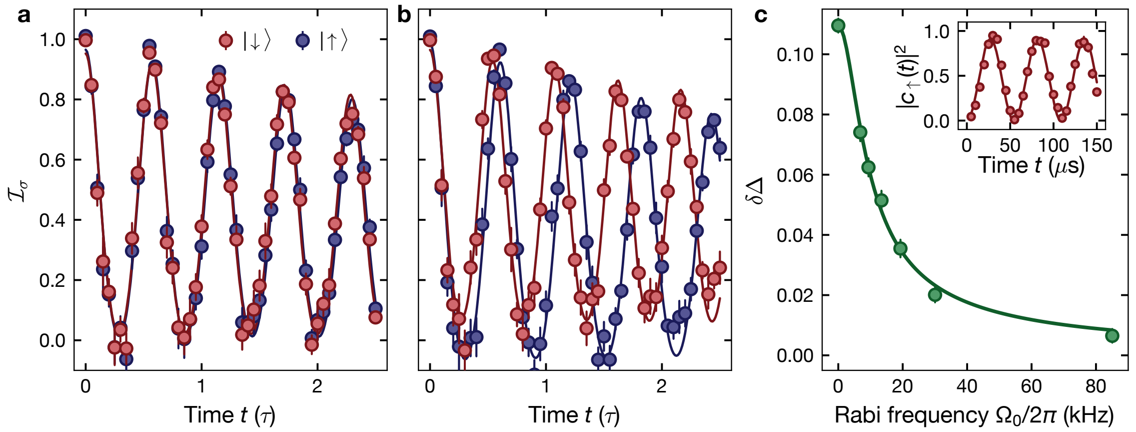

Figure 4.3.: RF dressing and tilt difference: **a** Bloch oscillations with maximal dressing power ($\Omega_0 = 85(1)$ kHz) resolved by the spin component. **b** Bloch oscillations without RF dressing. The frequency difference is explained by the natural difference in the magnetic moment of the spin states. The solid lines are analytical fits to extract the oscillation frequency (see text) and the error bars denote the standard error of the mean obtained from four averages. **c** Tilt difference $\delta\Delta$ as a function of the Rabi frequency Ω_0. We can tune it continuously between about 11.0(2) % and 0.6(2) %. The solid line is a fit to the data points with only one free parameter according to Eq. (4.13). The inset shows a sample data set we extract the Rabi frequency from, as fit parameters for the solid line we use the frequency and amplitude. The vertical axis is the excitation probability from $|\downarrow\rangle$ to $|\uparrow\rangle$.

picture for the origin of the detuning. Given the space-dependent detuning across the lattice, the tilts seen by the dressed states $|\tilde\downarrow\rangle$ and $|\tilde\uparrow\rangle$ following Eq. (4.13) are given by

$$\tilde\Delta_{\uparrow,\downarrow} = \frac{\Delta_\uparrow + \Delta_\downarrow}{2} \pm \frac{\Delta_\uparrow - \Delta_\downarrow}{2}\frac{|\delta|}{\sqrt{\Omega_0^2 + \delta^2}}. \tag{4.15}$$

In the experiment we automatically average across all possible values of the tilts throughout the atomic cloud. This averaging effect can be imitated numerically by computing the resulting superposition of Bloch oscillations with the respective frequency $\tilde\Delta_{\uparrow,\downarrow}$ and weighing their contribution with a Gaussian distribution representing the density distribution of the atomic cloud. For large tilts we expand the Bessel function in the analytical description for Bloch oscillations according to Eq. (4.14) to second order yielding a cosine-function. Hence, we obtain the imbalance resulting from this superposition as

$$\begin{aligned}\mathcal{I}_{\tilde\uparrow,\tilde\downarrow}(t) &= \frac{1}{\eta}\sum_{i=-L/2}^{L/2} \mathcal{J}_0\left(\frac{8J}{\tilde\Delta_{\uparrow,\downarrow}(\delta_i)}\sin\left(\pi\tilde\Delta_{\uparrow,\downarrow}(\delta_i)t/h\right)\right)\cdot\exp\left(-\delta_i^2/(2\sigma^2)\right)\\ &\approx \frac{1}{\eta}\sum_{i=-L/2}^{L/2}\left[1-\frac{1}{2}\left(\frac{4J}{\tilde\Delta_{\uparrow,\downarrow}(\delta_i)}\right)^2\left(1-\cos\left(\tilde\Delta_{\uparrow,\downarrow}(\delta_i)t/\hbar\right)\right)\right]\cdot\exp\left(-\delta_i^2/(2\sigma^2)\right)\end{aligned} \tag{4.16}$$

with the normalization constant $\eta = \sum_i \exp\left(-\delta_i^2/(2\sigma^2)\right)$ and the standard deviation of the detuning distribution across the atomic ensemble $\sigma = 14.5\,\mathrm{kHz}$. We fit this superposition in Eq. (4.16) with a single oscillation frequency and extract the tilt difference $\tilde{\Delta}_{\downarrow}^{\mathrm{eff}} - \tilde{\Delta}_{\uparrow}^{\mathrm{eff}}$ of the dressed states for multiple Rabi frequencies Ω_0. This results in a distribution of the tilt difference as a function of the Rabi frequency similar to the one shown in Fig. 4.3c. Fitting the model in Eq. (4.13) we retrieve an effective detuning of $\delta^{\mathrm{eff}} = 9.8(1)\,\mathrm{kHz}$. This value is reasonably close to the experimental value and confirms our intuitive explanation. In summary, the technique of RF dressing represents an effective tool to control the dynamics of the tilted Fermi-Hubbard model in terms of the dressed states. The tilt difference between them can be tuned continuously from the natural value of $\delta\Delta = 11.0(2)\%$ to the best possible compensation $\delta\Delta = 0.6(2)\%$ at our maximal Rabi frequency of $\Omega_0 = 85(1)\,\mathrm{kHz}$. Moreover, the kinetic and interaction part of the Hamiltonian are invariant under the transformation to the dressed basis, which largely simplifies the experiment as we can immediately employ the existing Feshbach resonance between the undressed states. Note that this fact is related to the SU(2)-invariance of the Fermi-Hubbard model.

The implementation of the RF dressing field required a few changes to the experimental setup because it is a high-power RF application as opposed to the hitherto state manipulations in the dipole trap and the lattice. First, an additional helical RF antenna had to be installed in the vicinity of the science cell. It is mounted along the x-axis and the dipole and lattice beams propagate through the center of the antenna. The RF signal with a frequency around 46 MHz is produced by an Agilent E4431B programmable digital signal generator. An RF-switch (ZX80-DR230-S+, Mini-Circuits) controlled by the TTL signal from the timing computer timely switches the RF field. The signal is then amplified up to 40 W by a high-power RF-amplifier (LZY-22+, Mini-Circuits) and directly guided to the antenna. In the experimental sequence we switch on the RF dressing in the deep lattice 1 ms before the time evolution starts. This time was found to be sufficient to reach steady conditions and Rabi oscillations between the original states have dephased due to magnetic field fluctuations. The subsequent time evolution in the lattice then takes place in terms of the dressed states. Immediately after time evolution we switch off the dressing field abruptly such that the states get projected back on the undressed eigenstates $|{\downarrow}\rangle$ and $|{\uparrow}\rangle$. This step is essential as we extract our observables in this basis. We also tested a slow decrease of the dressing power to probe the adiabatic limit, but did not measure any difference in the subsequent imbalance readout.

5. Observables

The experimental observables employed in the thesis projects give information about localization properties of the system and global charge distributions in the lattice. We primarily resort to the density imbalance when investigating the dynamics of the many-body system and deciding if it exhibits localization. Moreover, we record density distributions of singly and doubly occupied sites in the lattice and infer global information on the system's response to external impacts such as harmonic confinement.

5.1. Density imbalance

The initial state in most of our experiments is a charge-density wave (CDW) with every second lattice site occupied. Those are referred to as even sites while the initial empty ones are referred to as odd. In a thermalizing system every memory of the initial state is erased in the course of time evolution, reaching an equilibrium state with all sites equally occupied (or rather obeying the chemical potential, but within a local density approximation the sites can be regarded as equally occupied in thermal equilibrium). If remnants of the highly non-thermal initial state persist after time evolution, this is a clear signature of non-ergodicity, indicating the presence of localized states. The density imbalance is defined as the occupation difference between even N_e and odd N_o lattice sites normalized to the total atom number

$$\mathcal{I} = \frac{N_e - N_o}{N_e + N_o}. \tag{5.1}$$

Hence, the initial state has an imbalance of one and the equilibrium state with an equal population on all lattice sites has a vanishing imbalance. Imperfections in the experiment in the initial state preparation or readout lead to a slightly reduced initial imbalance around $\mathcal{I}_0 = 0.90(2)$, but this is compensated by a proper calibration method [117] such that the experimental data should range from 0 to 1. This way it is easier to compare to numerical simulations, which typically assume perfect initial state preparation.

One major advantage of the imbalance in connection with our CDW initial state is the access to local microscopic properties of the final state although the experiment is not equipped with high-resolution tools such as single-site resolution in quantum-gas microscopes. Given our ability to distinguish even and odd lattice sites no long-range particle transport is required for a significant change of the observable. It can therefore give information both on fast short-range processes as well as intrinsically slow dynamics. Note that while the imbalance can clearly indicate localization in the case of a finite value, a vanishing imbalance is no evidence for ergodicity. The non-interacting Stark model, for instance, possesses distinct points where the imbalance is exactly zero, but the eigenstates are localized for any finite tilt. Instead, this result is related to the particular functional form of the eigenstates at this point in parameter space (see sec. 8.1 and [117]).

5.1.1. General method of initial state preparation and final state readout

As introduced in sec. 4.2, we have a short primary lattice and a long lattice with twice the wavelength. Together they form the superlattice setup with a freely tunable phase between both lattices. This is used to prepare the initial CDW ordered state as well as to read out the imbalance of the final state after time evolution.

Initial steps of the lattice loading procedure are already explained above. After preparing the atoms in the long lattice, the short lattice is ramped to $18E_{r,s}$ with a phase of 0.44π such that one obtains strongly tilted double wells and thereby ensures that only the lower energy site is occupied. When the long lattice is ramped down, one ends up with the CDW state in the short lattice. These steps are illustrated in Fig. 5.1a. The scattering length during the loading sequence sets the number of doubly occupied sites (doublons). While the formation of doublons is favored for attractive interactions, repulsive loading can suppress their formation below the detection limit [126]. The sequence applies equally to doublons such that doubly occupied sites in the long lattice are preserved in the final CDW state.

The final state detection and imbalance extraction equally make use of the superlattice setup, as depicted in Fig. 5.1b. Details on the bandmapping technique can be found in [199, 200] and the full calculations for our system are performed in [201], such that only the most important points are briefly reviewed here. After freezing the dynamics at the end of the time evolution by ramping up the primary lattice, the long lattice is added with the same superlattice phase as before. Then, we increase the depth of the long lattice to $50E_{r,l}$. In the band structure we thereby ramp across an avoided crossing of the second and third band of the superlattice fast such that the atoms on odd sites are excited to the third band. When the short lattice is now switched off, those atoms are projected onto the third band of the long lattice while atoms on even sites remain in the ground band. In the end, all lattices are switched off adiabatically and time-of-flight images reveal the momentum space distribution in the lattice as shown in Fig. 5.2a. Counting the population in the

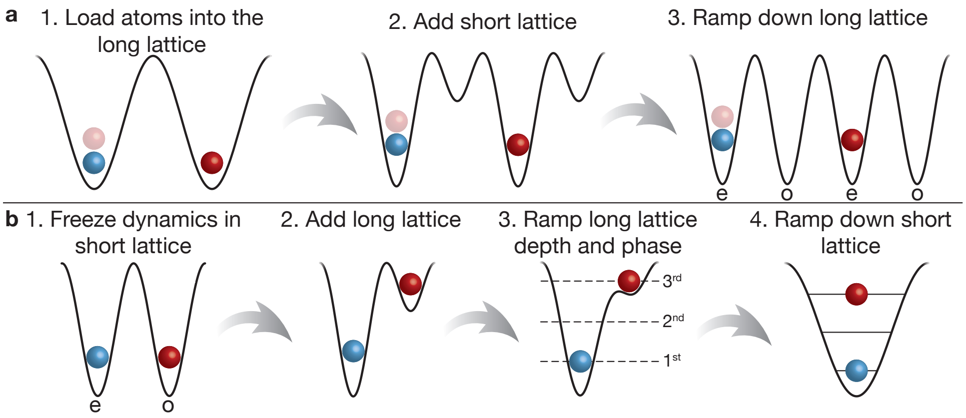

Figure 5.1.: Schematic representation of the CDW preparation and imbalance readout: a Lattice sequence for the creation of a CDW initial state in the short (primary) lattice. **b** State transfer and bandmapping after time evolution to extract the density imbalance as explained in the text. Colors indicate different spin components. The more transparent atom illustrates that the scheme equally works with doublons in the initial state. They are preserved in both sequences.

different bands of the lattice then finally yields the imbalance in Eq. (5.1). The transfer to the third band is necessary in order to spatially separate the bands in the raw images.

5.1.2. Spin-resolved readout

The imbalance returns information about the microscopic density distribution of the entire atomic sample in the lattice. However, in particular when investigating spin-dependent dynamics, it is advantageous to be capable to access the different spins separately. Typical setups with spin-dependent dynamics include alkaline-earth systems in state-dependent optical lattices. These are for example investigated in the context of optical lattice clocks [202] or quantum computation with optical qubits [203]. In our experiment we can induce a spin-dependent tilt generated by an inhomogeneous magnetic field (see sec. 8.2). The spins encoded in the magnetic hyperfine states thus experience a different strength of the magnetic field gradient resulting in spin-dependent dynamical properties.

While the bandmapping sequence is explained in the previous section, measuring the spin-resolved imbalance requires two changes to the procedure. First, an inhomogeneous magnetic field is applied during time of flight. The spins have different magnetic moments $\mu = \mathrm{d}E(B)/\mathrm{d}B$, where $E(B)$ is the state energy in the external magnetic field. In the case of atoms in the ground state manifold $4^2S_{1/2}$ it can be computed analytically via the Breit-Rabi equation. The resulting force $\vec{F} = -\nabla(\vec{\mu} \cdot \vec{B})$ is therefore also spin-dependent

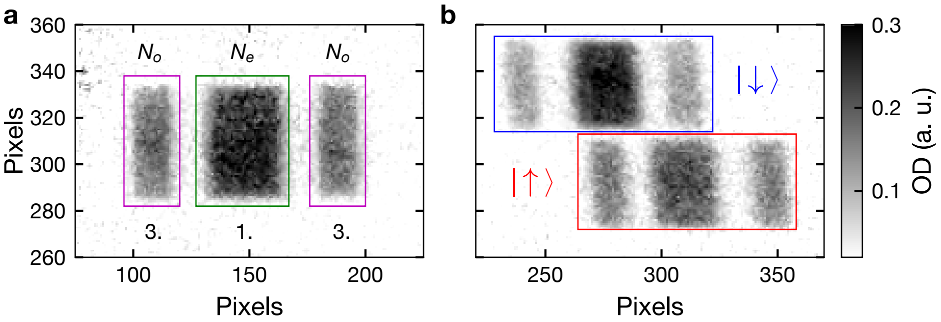

Figure 5.2.: Raw images for imbalance measurement: a Bandmapping image after 8 ms time of flight. The rectangles indicate the first and third band, the respective populations represent the final distribution of particles among even and odd lattice sites (N_e and N_o) and yield the density imbalance $\mathcal{I}$. **b** Spin-resolved bandmapping images after spatial separation with the Stern-Gerlach technique in an inhomogeneous magnetic field and 6.4 ms time-of-flight. The identification of both spin components is represented by the rectangles. The individual imbalances are extracted in the same manner as in **a**.

such that the two states separate spatially during time-of-flight. This is the famous Stern-Gerlach technique. However, the difference in the magnetic moments of the states $|\uparrow\rangle$ and $|\downarrow\rangle$ is insufficient to generate a large enough spatial separation in the imaging area. Therefore, we transfer the atoms in $|\uparrow\rangle$ to the state $|\rightarrow\rangle \equiv |F = 9/2, m_F = -5/2\rangle$ with a radio-frequency Landau-Zener sweep prior to the band transfer and bandmapping. In this context we make use of the Feshbach resonance between the states $|\downarrow\rangle$ and $|\rightarrow\rangle$ centered around 224.2 G. Its non-interacting point is located at 231.6 G. We thus ramp the field to this point and then exert the aforementioned sweep. Performing the bandmapping in the absence of interactions is important to avoid interband oscillations after the band transfer. Moreover, we found empirically that the data accuracy improves, primarily due to a better quality of the raw images. With this additional state manipulation the spin states can be separated spatially on the CCD camera as illustrated in the sample raw image in Fig. 5.2b. The individual imbalance of both spins is then obtained in the same manner as in the regular readout sequence.

5.2. Singlon and doublon imbalance

Not only can we modify the experimental sequence in order to gain information about the spin-dependent dynamics, but it is also possible to separately access the imbalance, and thus dynamical information, of singlons and doublons. This capability enables us to measure a local observable to characterize the dynamics of singly and doubly occupied sites and thus resolve physical hopping processes predicted by the respective Hamiltonian. For the project presented in part IV this information is essential so as to gain precious complementary insights on the state-dependent dynamics.

In the experiment we employ a subtractive method, similar to what was realized in a previous project on non-equilibrium mass transport [126], to separate the singlon and doublon imbalance. Note that in this case we do not rely on a spin-resolved readout. In a first shot we take a regular image and detect the density imbalance $\mathcal{I}$ and total atom number N. In a second shot with the same experimental settings we remove the doublons with the doublon blast right before the band transfer and final state readout (see sec. 5.1). This blast is a near-resonant light pulse that induces strong light-assisted collisions on doubly occupied sites thus removing all doublons and keeping the singlons virtually unaffected [126]. Hence, the second image contains information about the singlon number N_S (in the following we will use the singlon density $n_S = N_S/N$) and readily represents the singlon imbalance $\mathcal{I}_S$. By subtracting the second from the first image we directly retrieve the doublon density $n_D = 1 - n_S$. Our definition of the doublon number N_D is such that it denotes the number of atoms bound in doublons, hence a single doublon means that $N_D = 2$. From there it is straightforward to show that the imbalance obeys the simple relation

$$\mathcal{I} = n_S \mathcal{I}_S + n_D \mathcal{I}_D, \tag{5.2}$$

which applies when the variation in the total atom number from shot to shot is small. In the experiment those variations are typically on the order of 10 %, but by averaging over multiple instances we justify this technique. The expression in Eq. (5.2) can be solved for the doublon imbalance $\mathcal{I}_D$ and its uncertainty $\Delta\mathcal{I}_D$ is computed via Gaussian error propagation:

$$\begin{aligned}
\mathcal{I}_D &= \frac{\mathcal{I} - (1 - n_D)\mathcal{I}_S}{n_D} \\
\Delta\mathcal{I}_D &= \Bigg(\left(\frac{\Delta\mathcal{I}}{n_D}\right)^2 + \left(\frac{n_D - 1}{n_D}\Delta\mathcal{I}_S\right)^2 \\
&\quad + \left[\left(\frac{\mathcal{I}_S}{n_D} - \frac{\mathcal{I} - (1 - n_D)\mathcal{I}_S}{n_D^2}\right) \left(\left(\frac{N_S}{N^2}\Delta N\right)^2 + \left(\frac{\Delta N_S}{N}\right)^2 \right)^{1/2} \right]^2 \Bigg)^{1/2}
\end{aligned} \tag{5.3}$$

Although it is rather uncommon in numerical works to extract the singlon and doublon imbalance, these observables can readily be implemented in the numerical simulations we employ in the respective project. For a given state they follow from the densities on a given lattice site i and are given by

$$\begin{aligned}
\mathcal{I} &= \langle \hat{\mathcal{I}} \rangle = \frac{1}{N} \sum_i (-1)^i \langle \hat{n}_i \rangle \\
\mathcal{I}_S &= \langle \hat{\mathcal{I}}_S \rangle = \frac{\sum_i (-1)^i \left(\langle \hat{n}_{i,\uparrow}(1-\hat{n}_{i,\downarrow}) \rangle + \langle \hat{n}_{i,\downarrow}(1-\hat{n}_{i,\uparrow}) \rangle \right)}{\sum_i \left(\langle \hat{n}_{i,\uparrow}(1-\hat{n}_{i,\downarrow}) \rangle + \langle \hat{n}_{i,\downarrow}(1-\hat{n}_{i,\uparrow}) \rangle \right)} \\
\mathcal{I}_D &= \langle \hat{\mathcal{I}}_D \rangle = \frac{\sum_i (-1)^i \langle \hat{n}_{i,\uparrow} \hat{n}_{i,\downarrow} \rangle}{\sum_i \langle \hat{n}_{i,\uparrow} \hat{n}_{i,\downarrow} \rangle \rangle}
\end{aligned} \tag{5.4}$$

with the sum running over all lattice sites.

This newly developed technique within the framework of this thesis represents one key ingredient for the investigations of part IV without the need for single-site resolution or other means of access to local observables such as correlation functions. Moreover, it provides additional information on the dynamics governed by a given Hamiltonian depending on the charge density of a given state.

5.3. In-situ density distributions

Contrary to the imbalance, which is a local observable, we also access global density distributions in the lattice via in-situ absorption imaging. These are used to characterize the distributions of singlons and doublons in the initial state as a function of various loading parameters. Given that our imaging resolution is limited to about 2.2 µm $\simeq$ 8.3 primary lattice sites per pixel on the CCD chip [126], we are at least able to investigate global particle distributions, though without access to local density patterns. Instead, it is possible to separate singly from doubly occupied lattice sites via a series of state manipulations with RF and MW operations. The newly developed scheme is carried out at the non-interacting point of the Feshbach resonance between the states $|\uparrow\rangle$ and $|\downarrow\rangle$ and comprises eight steps in total including the imaging sequence. The entire procedure is also represented schematically in Fig. 5.3 highlighting the relevant atomic states in the ground state hyperfine manifolds. The operations are exclusively performed on the singlons since we found that changing the doublon interaction diabatically can lead to unwanted losses.

In the scheme we exploit that singlons and doublons can be distinguished spectroscopically via an interaction shift. Take for instance a doublon $|\uparrow\downarrow\rangle$ which is non-interacting at the set magnetic field. When sending a pulse exciting the state $|\uparrow\rangle$ to $|\rightarrow\rangle$ the new interaction strength is governed by the Feshbach resonance for the states $|\downarrow\rangle \leftrightarrow |\rightarrow\rangle$. With these particular settings the doublon is now strongly repulsively interacting with a scattering length of $262a_0$ such that one has to overcome the interaction shift in addition to the

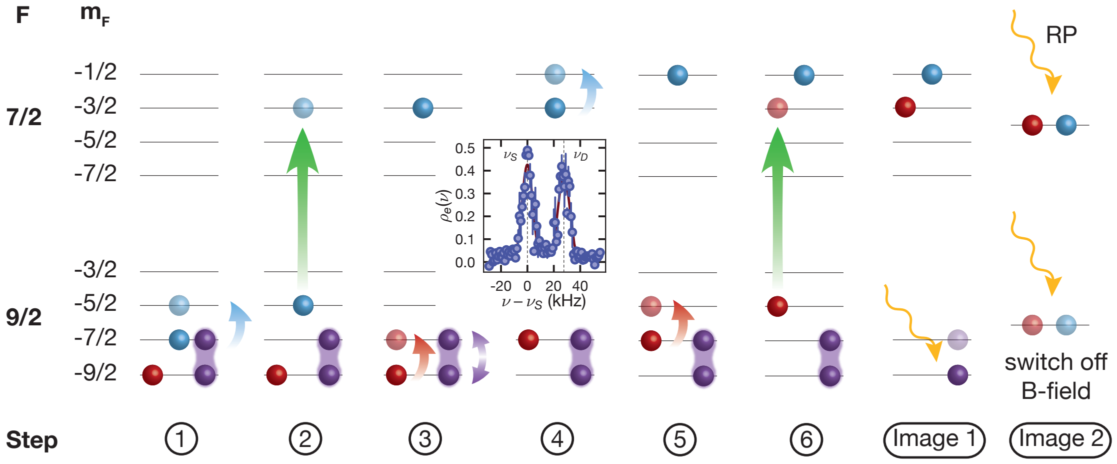

Figure 5.3.: Singlon and doublon imaging scheme: This schematic figure illustrates the state operations with RF (red and blue arrows) and MW (green arrows) fields employed to image singlons and doublons separately. The colored spheres represent the initial spin states and the purple groups are opposite spins bound in doublons. RF sweeps and pulses operate in the same hyperfine manifold while MW sweeps excite the atoms to the $F = 7/2$-manifold. Except of the second imaging step, all operations are performed at the non-interacting point of the Feshbach resonance at 209.1(1) G. The inset shows an experimental RF spectrum to illustrate the interaction shift between singlons and doublons relevant for steps 1 and 5. Two distinct peaks at the singlon ν_S and doublon ν_D resonance emerge which can be clearly resolved. From the relative height of the peak we extract a doublon fraction of $0.46(2)$. All data points are averaged thrice with the error bars showing the standard error of the mean and the fitting is done with a composite sinc-function.

regular energy difference between the states in the external magnetic field. This shift depends on the difference in the scattering length as well as the particular lattice depths (follows from Eq. (4.3)). In our case with lattice depths $V_p = 18E_r$ and $V_\perp = 36E_r$ the shift amounts to about 32 kHz and is therefore larger than the resolution of the RF-pulse used to separate them (17 kHz). A sufficient resolution is essential to separate the resonances as shown in the inset in Fig. 5.3. The visible peaks are resonances of the RF-excitation from $|\uparrow\rangle$ to $|\rightarrow\rangle$. While the singlon resonance ν_S is not affected, the doublon resonance ν_D is offset by the interaction shift as explained above. The following list explains the scheme to image singlons and doublons exploiting the described interaction shift. All atoms are initially in the state $|F = 9/2, m_F = -9/2\rangle$ or $|F = 9/2, m_F = -7/2\rangle$, either as singlon or bound in a doublon.

1. First, singlons in the $|m_F = -7/2\rangle$-state are excited to $|m_F = -5/2\rangle$ with an RF π-pulse. This way we only excite singlons while doublons in the same state are sufficiently separated via the interaction shift.

2. The excited singlons in the $m_F = -5/2$-state are transferred to $|F = 7/2, m_F = -3/2\rangle$ in the other hyperfine manifold with a MW sweep. Due to magnetic field fluctuations in the experiment and the enhanced sensitivity of the transition frequency for an MW transition, we cannot perform a pulse with sufficient fidelity here.

3. An RF sweep swaps the occupations in the $F = 9/2$ ground state. This way the remaining singlons are transferred to $m_F = -7/2$ and the doublons are practically unaffected. Since the bandwidth of the sweep is much larger than the interaction shift, singlons and doublons are equally transferred.

4. An RF sweep clears the currently occupied level $|F = 7/2, m_F = -3/2\rangle$ by sweeping the singlons to $m_F = -1/2$. Otherwise the second MW sweep in step 6 would bring them back to the $F = 9/2$-manifold.

5. Repeat step 1.

6. Repeat step 2.

After this series of pulses and sweeps the singlons are transferred into the $F = 7/2$ hyperfine manifold while the doublons remain in their original states. For the imaging part of the sequence we send two light pulses which image the particle distribution via absorption imaging. Thereby we gain independent information on the singlon an doublon distribution as explained in the following.

1. In the presence of the magnetic field we shine in light resonant with the closed-cycling transition $|F = 9/2, m_F = -9/2\rangle \rightarrow |F = 11/2, m_F = -11/2\rangle$ with the latter in the $4P_{3/2}$ excited state. Hence, we only detect one of the doublon components. The other atoms are invisible for two reasons. First, the imaging laser is detuned by about 30 MHz with respect to the respective transition. Second, starting from $m_F = -7/2$ there is no closed-cycling transition such that the atoms will ultimately be lost from the cycle ending up in a dark state. Therefore, this method is not useful for a determination of the doublon fraction, but since the spin components are distributed equally across the lattice, this method is a viable technique to positively image the doublon distribution.

2. Between the first and second imaging pulse the magnetic field is ramped down. Since the doublons have been removed during the imaging process, there are only singlons left in the lattice and thus molecule formation upon crossing the Feshbach resonance is not an issue. Moreover, the laser detuning is changed so as to be on resonance in the absence of a magnetic field. Consequently, the second image displays the singlon distribution.

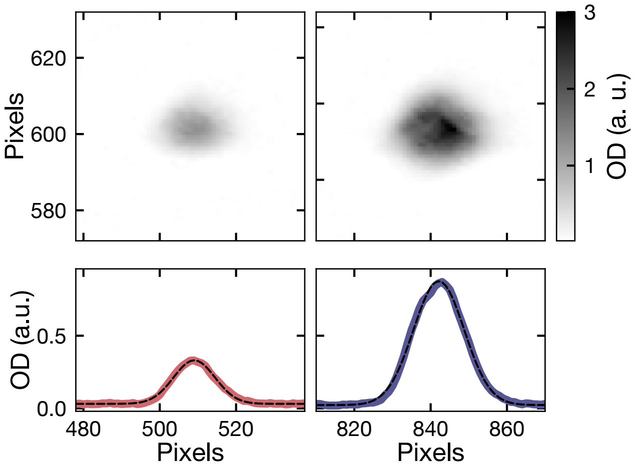

Figure 5.4.: In-situ distribution of singlons and doublons: Exemplary raw data obtained with the imaging scheme explained in this section. Top: Doublon (left) and singlon (right) density profile in the lattice. The colorbar represents the optical density in arbitrary units, but on the same scale for both panels. Bottom: Integrated profiles along the vertical direction. The dashed lines are Gaussian fits to the profile used to extract the cloud width.

A sample raw image obtained with this technique is shown in Fig. 5.4. The data can be used to evaluate the initial state distribution of singly and doubly occupied sites in the lattice as a function of the loading parameters and retrieve the cloud size from fitting a Gaussian distribution. This analysis was performed for the project reported in part IV and is evaluated in detail in sec. 9.2.2. The total fidelity of the entire sequence is limited by the magnetic field stability during the π-pulses to about 80 %, the sweeps have a nearly perfect transfer probability. This results in a small scatter of the recorded atom numbers. Therefore, we cannot use this scheme reliably to measure the doublon imbalance and instead resort to the indirect method explained above.

Part III.

Ultracold atoms in quasiperiodic potentials

A tight-binding lattice model with a quasiperiodic potential, the Aubry-André model, features a single-particle localization transition for all eigenstates and is known to be many-body localized for sufficiently strong detuning. These facts are well-established by numerical investigations and experiments. However, beyond the tight-binding limit a single-particle mobility edge (SPME) emerges such that localized and extended eigenstates coexist in different regions of the spectrum. The corresponding many-body equivalent - a many-body mobility edge - has been observed numerically in small systems, but its existence in the thermodynamic limit is still a highly debated topic. Here we describe our implementation of a lattice model with a single-particle mobility edge and explore its fate upon the addition of (weak) local interactions. We thereby want to investigate two central questions in this context: Does MBL exist in a model that features an SPME in its non-interacting limit? Does an SPME give rise to a many-body intermediate phase that features a coexistence of localized and extended many-body states?

6. Single-particle mobility edge in the generalized Aubry-André model

6.1. The generalized Aubry-André model

In chapter 3.1.1 the central properties of single-particle mobility edges as well as key models in theory and numerics were presented. However, the generalized Aubry-André (GAA) model introduced in Eq. (3.1) has no obvious significant experimental relevance apart from few fine-tuned exceptions, while the incommensurate lattice model in Eq. (2.2) results from the superposition of two optical lattices with an irrational wavelength ratio, which is readily implementable in cold atom experiments and in other suitable platforms [28, 29, 49, 204].

As explained in sec. 2.1.2, this model can be mapped to the AA model in the tight-binding limit of infinite primary lattice depth. However, when the tight-binding approximation breaks down, for example in the situation of a shallow primary lattice, additional continuous degrees of freedom have to be taken into account. In order to be able to derive an effective lattice Hamiltonian regardless, a Wegner flow approach [120, 132, 205] can be employed, yielding the Hamiltonian in Eq. (6.1) including corrections up to second order:

$$\begin{aligned}\hat{H}_{GAA} &= \hat{H}_{AA} + J_1 \sum_{i,\sigma} \cos\left[2\pi\beta\left(j+\frac{1}{2}\right)+\phi\right](\hat{c}^{\dagger}_{i+1,\sigma}\hat{c}_{i,\sigma} + \text{h.c.}) \\ &\quad - J_2 \sum_{i,\sigma}(\hat{c}^{\dagger}_{i+2,\sigma}\hat{c}_{i,\sigma} + \text{h.c.}) \\ &\quad + \Delta' \sum_{i,\sigma} \cos(4\pi\beta i + 2\phi)\hat{n}_{i,\sigma} \\ &= \hat{H}_{AA} + \hat{H}'.\end{aligned} \tag{6.1}$$

This lattice Hamiltonian resulting from a bichromatic potential will be referred to as GAA model in the following. The corrections to the tight-binding description of H_{AA} (Eq. 2.3) are a correction to the nearest-neighbor hopping amplitude J_1 caused by the detuning lattice, the introduction of second-order or next-nearest-neighbor tunneling with amplitude J_2 as well as a correction of the on-site potential with strength Δ'. Typical values of the parameters for realistic experimental situations are listed in appendix A. These additional terms are vital to capture the mobility edge occurring in this model as will be shown by numerical simulations in this chapter. The appearance of an SPME follows from the violation of the self-duality of the model and its explicit non-nearest neighbor nature [132].

One commonly employed way to study the localization properties of such models is to compute the normalized (NPR) and inverse participation ratio (IPR) as defined in Eq. (6.2) of all eigenstates in the lowest band.

$$IPR^{(i)} = \frac{\sum_m |u_m^{(i)}|^4}{\left(\sum_m |u_m^{(i)}|^2\right)^2}, \quad NPR^{(i)} = \left(N \sum_m |u_m^{(i)}|^4\right)^{-1} \tag{6.2}$$

Here the sum runs over all lattice sites m and $u_m^{(i)}$ denotes the i-th eigenstate. For a perfectly extended state that has the same occupation probability on every site $|u_m| = 1/\sqrt{N}$ for system size N, the IPR becomes $\sum_m |1/\sqrt{N}|^4 = N/N^2 = 1/N \xrightarrow[N\to\infty]{} 0$ (the denominator is a normalization factor equal to one for a normalized state). In the thermodynamic limit, this expression vanishes. On the other hand, if one considers a delta-localized state on site k ($|u_m| = \delta_{m,k}$), the IPR is $\sum_m \delta_{m,k} = 1$. It is even possible to draw a connection between the IPR and the imbalance: When ignoring the normalization factor the imbalance can be expressed as $\mathcal{I} = \sum_m \left(|u_{2m}|^2 - |u_{2m+1}|^2\right)$ distinguishing even and odd lattice sites. For an extended states it attains a vanishing value since even and odd lattice sites are equally occupied. On the other hand, an initial charge density wave state that retains its memory evidently adopts a positive value.

Conversely, the NPR remains finite for spatially extended states and goes to zero for localized states. This can be seen equally easily if we consider the same limiting case as for the IPR above. For a spatially extended state the NPR becomes $\left(N \sum_m |1/\sqrt{N}|^4\right)^{-1} = \left(N \cdot N/N^2\right)^{-1} = 1$. And for the maximally localized state we instead have $\left(N \sum_m |\delta_{m,k}|^4\right)^{-1} = 1/N \xrightarrow[N\to\infty]{} 0$.

By averaging over all eigenstates across the entire spectrum at a certain detuning strength the two quantities yield complementary information since they are sensitive to either localized or extended states. Thus, they reveal the existence of a single-particle intermediate phase when both observables are finite and indicate the coexistence of localized and extended states. This is explained in full detail in the following section.

6.2. Single-particle simulations

The properties of the non-interacting generalized Aubry-André model can be studied directly using ED simulations on large system sizes. From a direct comparison to the AA model we can then identify the major differences between the two models, which are relevant for the project. We implement the Hamiltonians from Eqs. (6.1) and (2.3) in the number basis and perform an exact diagonalization with a system size of $L = 369$ sites. This system size was also employed in [119] and represents a good compromise between finite-size effects and computation time. In order to study the impact of higher orders in the Hamiltonian directly, we choose $V_p = 4E_r$ for both models and manually set the higher order terms to zero for the AA model while they are taken into account with the correct values relevant to the experiment for the GAA model (see appendix A). The appearance of a single-particle mobility edge in the GAA model or its relatives [132, 206] can immediately be identified from IPR and NPR (Eq. 6.2). This is depicted in Fig. 6.1a where the participation ratios are plotted as a function of the detuning strength V_d as defined in Eq. (2.2). The single-particle localization point of the AA model is around $V_d = 0.5E_r$ as indicated by the vertical gray line. Within the numerical accuracy the IPR becomes finite at the same point the NPR goes to zero. This implies that all states become localized at the same detuning strength. Contrarily, in the GAA model there is a broad range where bot the IPR and NPR are finite, meaning that localized and delocalized states coexist. This is precisely the situation when a mobility edge is present. Note that the localization already sets in below the transition point of the AA model.

Another insightful observable to highlight the differences between both models is to investigate the eigenstates directly as a function of their energy. In the following we perform this analysis for a constant detuning strength of $V_d = 0.6E_r$. In Fig. 6.1c and d we show the logarithm of the real-space probability distribution $\langle\psi|\psi\rangle = |\psi|^2$ of every eigenstate $|\psi\rangle$ as a function of its energy. As expected, the AA model shown in panel d exhibits a homogeneous behavior of its eigenstates without any sign of an energy dependence. This is in agreement with the result from panel a which implies that all eigenstates localize for $V_d > 0.5E_r$ irrespective of their energy. The situation is vastly different for the GAA model in panel c. Here we see a strong dependence of the localization characteristics across the energy spectrum. While the low-energy states are strongly localized with a localization length that is shorter than in the AA model respectively, the high-energy states are delocalized. This immediately follows from the approximately homogeneous density distribution across the entire system. Between these limits the localization length further exhibits an energy dependence, a context that is studied in more detail in Fig. 6.1b. It is known that the eigenstates of both models are exponentially localized according to $|\psi(x)| \propto \exp(-|x - x_0|/\zeta))$ with center position x_0 and localization length ζ. We fit the

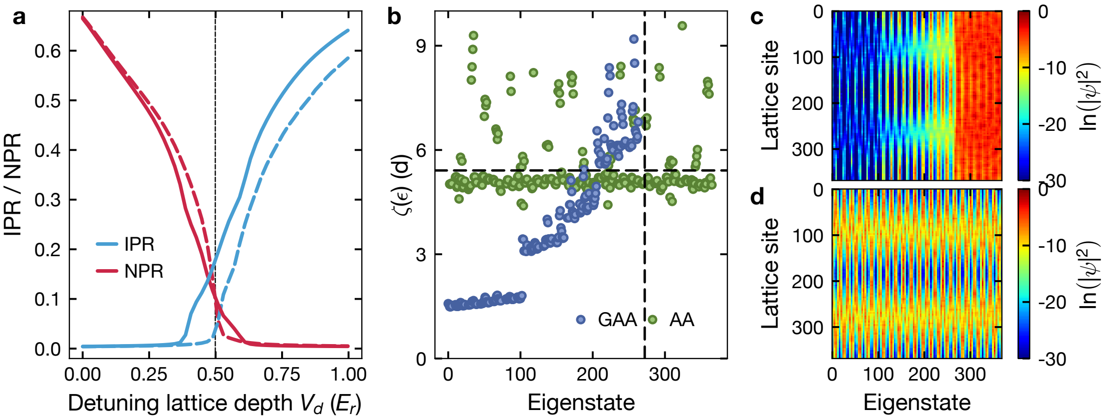

Figure 6.1.: Numerical properties of the GAA model: a IPR and NPR of the AA (dashed lines) and GAA model (solid lines). The dashed vertical line represents the single-particle localization point in the AA model. **b** Energy-dependent localization length $\zeta(\epsilon)$ in lattice sites d for the GAA and AA model. The horizontal dashed line is the analytical prediction for the AA model and the vertical line marks the approximate position of the mobility edge in the GAA model. **c** Eigenstates of the GAA model obtained from ED on 369 lattice sites. The color code represents the occupation probability on a logarithmic scale. A significant dependence of the localization length on the energy and the mobility edge are clearly visible. **d** The same situation for the AA model. The localization length is independent of the energy since the AA model does not possess a mobility edge. For all simulations in panels b-d a detuning strength of $0.6E_r$ was used.

numerically obtained eigenstates with this analytical function within a certain window around the center position to obtain the localization length. In order to weigh all points equally, the fitting is performed on a logarithmic scale. The scatter in the data is caused by boundary effects. In the AA model all states have about the same localization length and the numerically obtained value matches the analytical prediction [24] $\zeta(\Delta) = 1/\ln(\Delta/2J)$ impeccably, as indicated by the horizontal dashed line ($V_d = 0.6$ corresponds to $\Delta/J \simeq 2.4$). The GAA model, on the other hand, possesses eigenstates whose localization length ζ does depend on the energy. The strongest dependence occurs in the center of the band. At high enough energy the localization length diverges and the fit fails. This is the position of the mobility edge in the spectrum, also indicated by the vertical line in Fig. 6.1b. The location of the mobility edge in this particular situation is around $\epsilon = 0.87J$, but the location depends on the strength of the detuning. For strong enough detuning the mobility edge will finally disappear and the entire system will be localized.

While the existence of an SPME is evident from the numerical analysis presented in Fig. 6.1, we further have to investigate how it can be identified in the experiment. While previous experiments for example demonstrated the appearance of an SPME in the 3D Anderson model via a measurement of the expanding density distribution, we investigate how an

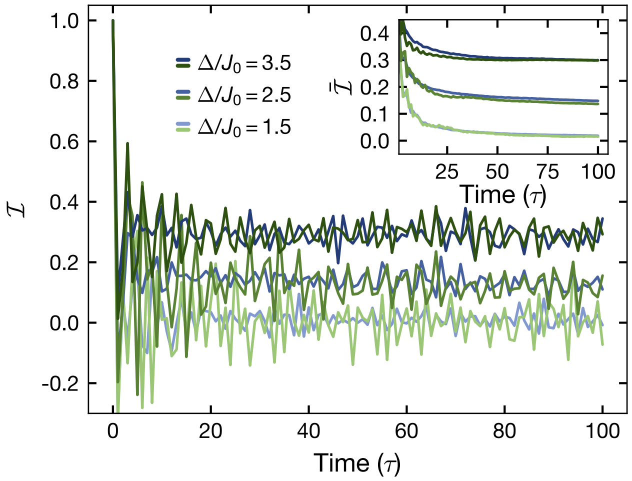

Figure 6.2.: Single-particle time traces: ED simulations of the non-interacting AA model (green) and GAA model (blue). The detuning values given in the legend are chosen such that the respective GAA model is in the localized, intermediate and extended phase. The inset shows the time-averaged imbalance $\bar{\mathcal{I}}$ of the main panel. In this case the main difference between both models for intermediate detuning in terms of a slightly difference steady-state imbalance becomes visible.

SPME could potentially be seen in the imbalance. For this purpose we simulate time traces of the non-interacting systems in the three regimes of the GAA model, namely extended, localized and intermediate starting from a charge-density wave initial state and compare them to the respective traces in the AA model. We use the same parameters as in Fig. 6.1 meaning that we only consider the leading terms in the AA model and use the parameters from appendix A for the GAA model. Since these are single-particle systems, the simulations can be performed by exact diagonalization (ED) on large system sizes. In this case we choose $L = 100$ sites and simulate the time traces in steps of one tunneling time.

All traces are averaged over ten initial state realizations and eight phases of the detuning potential. The lowest detuning value $\Delta/J_0 = 1.5$ is below the single-particle localization transition and thus in the fully extended phase. The corresponding time traces thus drop to zero within the first few tunneling times and remain there for the remaining evolution. The opposite happens for the largest detuning Δ/J_0 where the imbalance remains finite around 0.3 throughout. In the inset of Fig. 6.2 we compute the time-averaged imbalance $\bar{\mathcal{I}} = \frac{1}{T}\int_0^T \mathcal{I}(t)dt$ that removes the remaining oscillations in the original time traces and better reveals the average value. Herein we observe that in both the extended and localized phase both models behave the same way and in particular saturate to the same imbalance plateau. Since all single-particle states are either extended or localized in both models this behavior is actually plausible. Conversely, for the intermediate detuning value $\Delta/J_0 = 2.5$ the initial conditions encompass a mixture of localized and extended states, so the fact that the imbalance remains finite is caused by the former. We further observe that the steady-state value in the GAA model is slightly higher, a result that is highly surprising since one would expect that the admixture of extended single-particle states should decrease the imbalance. Though, this outcome is in agreement with the behavior of the IPR in Fig. 6.1a that is higher in the GAA model and thus explains the larger imbalance. One can understand this result by considering the CDW initial state as a superposition of eigenstates $|\phi_i\rangle$ according to $|\Psi_{\mathrm{CDW}}\rangle = \sum_i c_i |\phi_i\rangle$ with coefficients $c_i = \langle\phi_i|\Psi_{\mathrm{CDW}}\rangle$. In this notation the imbalance can be expressed as $\bar{\mathcal{I}} = \sum_i |c_i|^2 \cdot \mathcal{I}\left(|\phi_i\rangle\right)$, which is a weighted average of the imbalance of each eigenstate. Strongly localized states with large imbalance now have a large overlap with the initial CDW initial state, while extended ones have a much weaker contribution. Hence, the localized low-energy states dominate and give rise to a higher imbalance in the GAA model despite the presence of extended states. However, the traces are hardly distinguishable, and potential small differences that hint towards the existence of an single-particle intermediate phase are too weak to be resolved within the experimental accuracy. Therefore, the imbalance alone is not eligible to be used as single observable in an experiment designed to investigate the intermediate phase in the GAA model. Instead, at least a second complementary observable is required as will be explained in the following section 6.3.

6.3. Previous experiment and the single-particle mobility egde in our system

A previous work carried out at our experiment realized the Hamiltonian from Eq. (6.1) and investigated the appearing single-particle mobility edge thoroughly [119, 120]. Those results are briefly summarized here as they are of major importance for the new results presented in chapter 7 of this thesis. In these experiments, a high-temperature initial state is produced via the CDW order and a sudden quantum quench. This way we can ensure that eigenstates throughout the entire spectrum of the first band are occupied, such that the existence of an SPME would be observed as a coexistence between localized and extended single-particle states. In analogy to the complementary numerical observables IPR and NPR the experiment also employed two observables, one sensitive to localized states and the other sensitive to extended states present in the system. The choice of two complementary observables is essential as the imbalance alone cannot reliably identify the aspired coexistence of localized and extended states. Simulating an exemplary time trace of the GAA and AA model, we find that the imbalance is indistinguishable within the experimental uncertainty and thus fails to identify the intermediate regime (see Fig. 6.2). The imbalance $\mathcal{I}$ returns positive values as soon as the first single-particle states localize. Contrarily, the expansion of the cloud $\mathcal{E}$, defined as the renormalized difference of the

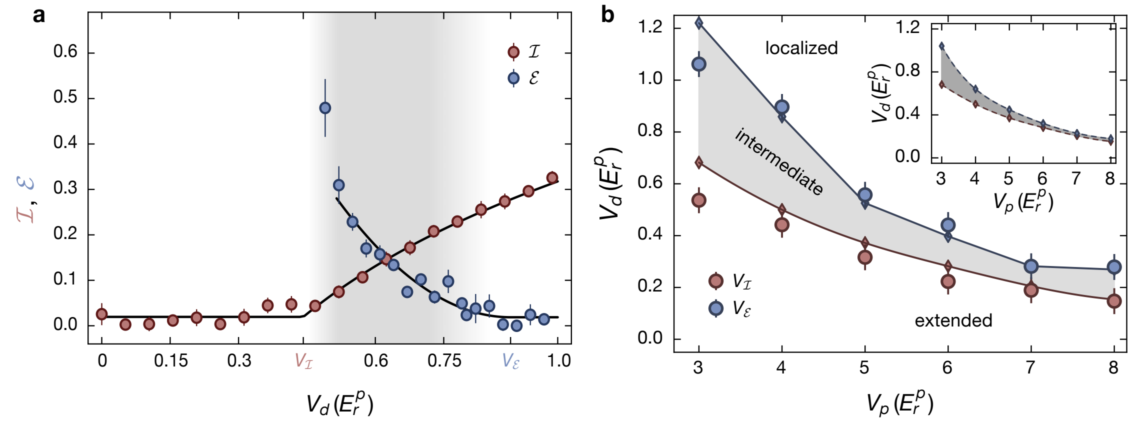

Figure 6.3.: Experimental results on the incommensurate lattice model: a Imbalance and expansion as a function of the detuning lattice depth for a primary lattice depth of $4E_r$. The solid lines are heuristic fits to the data in order to extract the critical point and the gray shaded region marks the detuning lattice depths where localized and extended states coexist. **b** Extracted phase boundaries of the intermediate phase from the data in panel a as presented in [119, 120]. Diamonds denote the numerical results including experimental imperfections of tube averaging. The inset shows the numerical results for the ideal system. Figure adapted from [120] with permission.

cloud size before and after time evolution, settles to zero as soon as all single-particle states are fully localized. Hence, if both types coexist in the intermediate region, both observables are found to be finite. This precisely happens for a certain range of detuning lattice depths and is shown in Fig. 6.3a for the case of $4E_r$ primary lattice depth. The experiment is able to identify a wide range of detuning strengths where both observables are finite, indicated by the gray shaded region. The transition points $V_\mathcal{I}$ and $V_\mathcal{E}$ for both observables are extracted via heuristic fits to the experimental data. By repeating this measurement for various primary lattice depths and extracting the critical points, a phase diagram can be mapped out as presented in Fig. 6.3b. The obtained results provide evidence for the emergence of three different single-particle phases for shallow primary lattice depths. At weak detuning all states are extended while sufficiently strong detuning localizes all eigenstates of the system. The appearance of an intermediate phase is elucidated above. Upon increasing V_p the tight-binding limit is approached and the width of the intermediate phase decreases continuously until it vanishes in the AA model. This trend is even more pronounced in the numerical calculation shown in the inset. From these results another observation can be drawn that all eigenstates of the underlying model become fully localized when the detuning strength overcomes the bandwidth of the first band [132]. At $8E_r$ primary lattice depth this is the case for $V_p \geq 0.24E_r$ and for $4E_r$ at $V_p \geq 0.65E_r$ respectively. The experimental data is in excellent agreement with numerical results. In the investigation of the interacting version of the model we rely on these single-particle results as they serve as an important reference for the non-interacting limit in our system.

7. Many-body intermediate phase and MBL in a model with a single-particle mobility edge

7.1. Current research on many-body mobility edges

As already introduced in sec. 3.1.2, it is important to distinguish two different types of mobility edges. The first type is a purely interaction-induced mobility edge as it was observed numerically in the randomly disordered 1D Heisenberg spin chain and related works (see sec. 3.1.2), where the corresponding non-interacting model is fully localized. The consensus states that the MBL phase transition is energy-dependent until at sufficiently large disorder the system is fully many-body localized even at infinite temperature. The second type is the more general feature of a many-body intermediate phase (MBIP) originating from a single-particle mobility edge upon the addition of interactions. It is therefore the main goal to investigate the fate of such an intermediate phase composed of extended and localized states when turning on local interactions. This question is usually approached perturbatively in numerics and analytics such that most works on this topic explore the regime of weak interactions on the order of the tunneling. In this project we exclusively focus on the latter type, an MBIP.

Up to this point the numerous numerical works on the issue of many-body mobility edges are not fully conclusive due to severe restrictions in the available systems sizes. There is thus no definite information about the thermodynamic limit. In particular, it is a viable option that many-body mobility edges are only a finite-size artifact and indeed there are opposing research results: on the one hand, published simulations exclude the existence of many-body mobility edges and an intermediate phase in general [67, 146]. Their main argument is based on hot thermal bubbles in an otherwise localized many-body system. These bubbles spread out resonantly and will ultimately thermalize the entire system, ruling out the existence of a mobility edge as well as an energy-driven MBL transition. A complementary viewpoint states that interactions lead to a net energy transfer from localized to extended states and thus delocalize any initial state [207]. On the other hand, recently, a new numerical investigation of a hard-core Bose-Hubbard model with a many-body mobility edge in the particle density [68] found long-lived localization up to 500 tunneling times and put forward an argumentation that is based on the restricted mobility of thermal bubbles. Though, these results also hold for a relatively small system and intermediate times only and it is therefore unknown what to expect in the thermodynamic limit. Further efforts from theory and experiment are required to shed light on this interesting question and it remained an open debate after the publication of our work [208] reported in this chapter.

Analogous limitations apply to the important question what exactly happens when interactions are added to a single-particle intermediate phase. The numerical works on this issue focusing on the specific case of a quasiperiodic potential [172, 173, 209] as in Eq. (3.1) produced rather inconclusive results due to finite-size effects. Though, those publications commonly conclude that even in the many-body system there emerges a new phase which is neither thermal nor many-body localized. Given this paradox, the phase was termed *non-ergodic metal* (or partially-extended) in order to emphasize the mixed nature of the eigenstates in this regime. On the one hand, the term *metal* insinuates a finite DC conductivity and thus particle transport, which is a key requirement for thermal systems that is absent in localized systems. This fact is represented by a vanishing DC conductivity in MBL systems [18–20] even at infinite temperature. They are therefore perfect insulators at all energies, which discriminates them from band insulators. Those only have strictly zero conductivity at zero temperature, otherwise thermal excitations to higher bands lead to a finite conductivity. On the other hand, *non-ergodic* implies that the system does not thermalize either in a sense that it violates ETH. The works cited above consider the eigenstate entanglement entropy as a precursor for non-ergodicity. Across the transition from a delocalized to a localized phase the entanglement entropy scaling changes from volume-law to area-law and by computing this quantity for different system sizes as a function of the energy, a critical energy E_L can be found above which the entropy scaling changes and the eigenstates become extended. This energy is therefore deemed to be the mobility edge as it separates localized and extended eigenstates. As complementary observable the mentioned theoretical works make use of the particle number fluctuations of states nearby in energy, defined as

$$O(E) = \sum_{j=1}^{L/2} \langle \Psi_E | \hat{n}_j | \Psi_E \rangle \tag{7.1}$$

with a many-body eigenstate $|\Psi_E\rangle$. Large fluctuations of this quantity $O(E)$ are a signature for non-thermal behavior and the violation of ETH. Computing these fluctuations as a function of energy, a critical energy E_T is identified as the energy below which the variance of the fluctuations increases drastically, characteristic for non-thermal behavior. The energies E_T and E_L were found to be unequal with $E_L < E_T$ indicating that the localization and thermalization transition point might not coincide. Those results point towards the

Observable	**Thermal**	**Non-ergodic metal**	**MBL**
Eigenstate entanglement entropy	Volume-law	Volume-law, but non-thermal	Area-law
NPR	Finite	$\propto 1/V_H^\gamma$ $(0 < \gamma < 1)$	$\propto 1/V_H$
Fluctuations	$O(E)$ small	$O(E)$ large	$O(E)$ large

Table 7.1.: Overview of numerical characteristics of the non-ergodic metal: This table summarizes the numerically found properties of the extended, partially-extended and localized phases in the quasiperiodic model as described in the main text.

existence of an intermediate phase with extended, non-ergodic eigenstates. In order to distinguish this intermediate phase from the established thermal and MBL phases, a series of observables are studied in [173]. They investigated the characteristic scaling of the entanglement entropy, normalized participation ratio and fluctuations, well-established observables in the context of thermalization and localization. The numerically obtained properties of the non-ergodic metal are summarized in Tab. 7.1. However, it should be emphasized that these results were carried out with exact diagonalization and system sizes $L \leq 16$ bear finite-size limitations that limit the significance of these findings although a recent work employing machine learning claimed to have found the non-ergodic metal phase with high confidence [210].

A many-body intermediate phase was also found in different settings, but with very similar results such that it is useful to mention them here. Hyatt et al. [211] consider the mechanism of coupling a localized system to a bath in a ladder model where the system and the bath have the same number of degrees of freedom (which distinguishes it from open system effects discussed in sec. 2.4). This assumption is comparable to the situation in a many-body mobility edge where localized and extended many-body states coexist at different energies and the latter may serve as a bath in the presence of interactions. While in such a setting the system usually tends to thermal equilibrium, certain parameter regimes can be found which violate the ETH, especially when the coupling between system and bath is weak. This observation is similar to the many-body localization proximity effect [58], which states that if a strongly localized subsystem is coupled to a weak bath, it can lead to localization of the entire system. Moreover, in a similar model of a two-legged ladder [212] reported on a new phase of matter called many-body mobility emulsion, which features extended and localized states at the same energy, so there is no mobility edge. Hence, there are still many open questions to be explored in the future.

In order to gain additional insights into this complex subject, we perform an experiment to search for a many-body intermediate phase starting from the single-particle mobility edge in the generalized Aubry-André model. With approximately 250 lattice sites, our experimental system is significantly larger than those typically studied in numerical investigation. Hence, finite-size effects should be significantly weaker and thus we can provide valuable complementary input, at least on the available observation times.

7.2. Experimental investigation of the non-ergodic metal phase

7.2.1. Experimental goals

Having established the notions of a single-particle mobility edge and many-body localization as well as the current theoretical understanding of a potential many-body intermediate phase, we move on to the new findings of this project. In a joint work of experiment and numerics we tackle two main questions that naturally arise when a system with a single-particle mobility edge coupled by interactions is considered. These are also depicted in the schematic heuristic phase diagram of the GAA model in Fig. 7.1:

1. Does MBL exist in a model which possesses a single-particle mobility edge? This question has been addressed in numerical studies predicting MBL in some models, but not as a generic feature [170, 213].
2. Does an SPIP survive finite interactions to become a many-body intermediate phase like a non-ergodic metal?

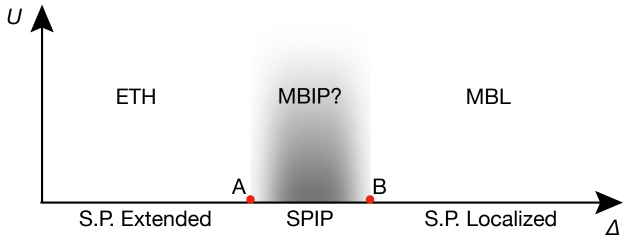

Figure 7.1.: Schematic conjectured phase diagram of the GAA model: The non-interacting GAA model has three different phases depending on the detuning strength (extended, intermediate and localized). The parameter Δ on the horizontal axis is the detuning strength and U is the Hubbard on-site interaction. The phase boundaries are indicated by A and B. The situation in the interacting case is mostly unknown, although an MBL phase is expected in a regime where all single-particle states are localized. Especially the existence of an MBIP (shaded in gray) is highly debated.

Experimentally, both models are accessible such that we can directly compare the dynamics of both interacting models whose single-particle limits either exhibit an SPME (GAA model) or not (AA model). We can detect differences in the dynamics and therefrom infer the potential existence of a many-body intermediate phase. This is the main strategy of the project described in this thesis. We thereby make use of the fact that the AA model has been studied very thoroughly both in experiment and theory such that its phase diagram is supposedly well understood. Moreover, it was shown that our experiment realizes the AA model very closely, both in the single-particle case [29] as well as in the interacting system as inferred from multiple projects comparing it to numerical simulations [40, 48].

7.2.2. Experimental techniques

The general lattice setup was already explained in sec. 4.2, here only the specific details for this project are reported. The light for the detuning lattice is generated by the same laser as the orthogonal lattices and thus has the wavelength $\lambda_d = 738\,\mathrm{nm}$. The incommensurability between the primary and detuning lattice is $\beta = \lambda_p / \lambda_d \simeq 0.721$. This value is also used in the numerical simulations below as well as in the non-interacting computations presented in sec. 6.2. Further, disorder averaging is implemented via changes to the detuning phase ϕ by setting different frequencies of the detuning lattice for individual runs. The lattice loading is performed with strong repulsive interactions at a background scattering length of $140a_0$, suppressing the doublon fraction in the initial state typically to $5 - 10\,\%$, close to our detection limit. Right before the time evolution, while the long lattice is switched off, the detuning lattice is ramped diabatically to the desired value within 10 µs. This timescale is much shorter than any dynamics in the lattice such that it can be regarded as a quench and hence the application of "quenched disorder" is experimentally justified. Quenching the primary from $18E_{rs}$ during the initial state preparation to the set value for the time evolution initiates the dynamics. After time evolution the scheme is repeated in inverse order. After ramping the short lattice back to $18E_{rs}$, the detuning lattice is switched off fast and at the same time the long lattice ramps up to $20E_{rl}$, creating strongly tilted double wells together with the primary lattice in order to freeze the dynamics. The remaining sequence is as described in sec. 5.1.1 including bandmapping and imbalance extraction.

In the experiment we can freely choose the primary lattice depth V_p and detuning lattice depth V_d during time evolution. This combination simultaneously sets the tight-binding parameters in first and second order as introduced in Eq. (6.1). While we focus on two different values of the primary lattice, we freely tune the detuning lattice depth between the thermal and MBL phase. The correspondence between the pairs (V_p, V_d) and the tight-binding parameters J_0, J_1, J_2, Δ and Δ' is visualized in Fig. 7.2 and further explained and tabulated in appendix A. In order to compare both models directly, we typically use the tight-binding parameters as multiples of the nearest-neighbor tunneling element J_0 in the following.

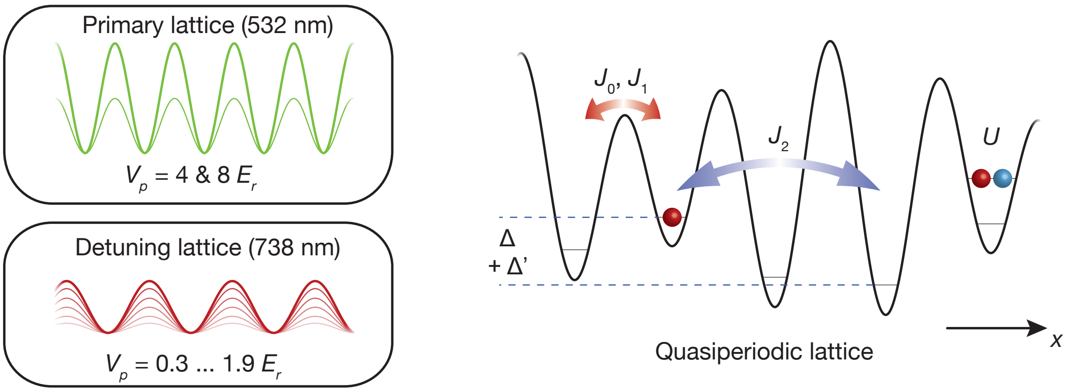

Figure 7.2.: Lattice setup in the MBIP experiment: Along the x-axis a primary lattice with wavelength $\lambda_p = 532\,\mathrm{nm}$ and a detuning lattice with $\lambda_p = 738\,\mathrm{nm}$ are superimposed to create the quasiperiodic potential. The depths of the lattices are given and the figure on the right illustrates the first- and second-order tight-binding parameters of the GAA-Hamiltonian in Eq. (6.1).

7.2.3. MBL in a system with an SPME

As opposed to previous works on the Aubry-André model on this experiment [29, 48, 60, 61], we realize the GAA model by a lower primary lattice depth [119]. This way higher orders in the Hamiltonian in eq. (6.1), in particular the second order tunneling J_2, become more relevant which leads to the appearance of an SPME in the single-particle spectrum as explained in section 3.1.1. Our first goal in this part is to explore if MBL is present in this system at all and if so, at which parameters it occurs. The general issue of MBL in the presence of an SPIP has been explored before with partially inconclusive results. Several works [170, 173, 213] agree that a spinless fermion model with the incommensurate detuning potential from Eq. (3.1) exhibits an MBL phase for sufficiently strong detuning in the infinite temperature limit. Such a conclusion is based on ED simulations for the entanglement entropy and level spacing statistics which exhibit the characteristic MBL properties (sec. 2.2.1). However, this observation is no general statement and strongly depends on the particular form of the detuning term. Other quasiperiodic models with modified on-site potentials were found to yield observables in agreement with thermal expectations in the presence of interactions. Therefore, a definite statement is missing and current studies also suffer from strong finite-size effects although it was attempted to relate properties of the non-interacting spectrum to the many-body system [213]. In particular, information about the thermodynamic limit is not accessible with numerics alone, hence we try to contribute with our experimental system that is about an order of magnitude larger than typical numerical systems in ED.

The experimental identification and characterization of a potential MBL phase will be carried out in a similar fashion as was already employed to detect critical dynamics near the phase transition of the AA model [48]. For this purpose we measure imbalance time traces after a quantum quench from an out-of-equilibrium CDW initial state for various detuning strengths Δ/J_0 (or V_d as defined in the continuum model in Eq. (2.2)). The experimental data is supported by exact diagonalization (ED) computations on up to 16 lattice sites assuming spinful (spin-1/2) fermions with on-site interactions in order to model the experiment as closely as possible. The initial state has a filling of 1/4 given the CDW order and the final numerics are averaged over different realizations of the spin configuration. In the experiment we assume a random spin order and automatically average over those in our detection sequence.

First, we focus on the regime of weak interactions, because this is the preferred setting in most theoretical investigations searching for MBL and an MBIP [63, 132, 169–171, 213], typically in random-field Heisenberg spin chains or spinless fermions with nearest neighbor interactions. It is believed that the weakly interacting regime is most auspicious for the observation of an MBIP because the interactions can be treated as a perturbation, simplifying the calculations, and the properties of the non-interacting system are most likely to survive. In this project we thus primarily work at an interaction strength of $U/J_0 = 1$. The time traces for the GAA model are recorded between 10τ and 100τ while the traces of the AA model span the range from 8τ to 40τ, the total observation time in both cases is roughly equal (up to 10 ms) due to the different primary lattice depths and hence unequal tunneling times $\tau = \hbar/J_0$. The short-time dynamics starting from the initial imbalance value $\mathcal{I}_0 = 0.90(2)$ is omitted because it is not relevant for our investigation. It mainly shows damped oscillations and a rapid imbalance decay from the initial value $\mathcal{I}_0$ [29, 48]. The resulting traces for both models are plotted in Fig. 7.3 on a doubly logarithmic scale. We focus on two detuning strengths above the single-particle localization transition of the tight-binding AA model located at $\Delta/J_0 = 2.0$ because for weaker detuning strengths the imbalance decays exponentially to zero within a few tunneling times due to the absence of localized states. The first time trace is taken at weak detuning strength of $\Delta/J_0 = 2.1$ just above the single-particle transition point. The traces for both models exhibit a considerable imbalance decay irrespective of the underlying model. Contrarily, the time traces at larger detuning strength of $\Delta/J_0 = 3.1$ is recorded deep in the single-particle localized phase of both models. Here, we observe larger values of the imbalance and a much slower decay over the experimental time span. Again, this assessment applies to both models equally. The experimental data is plotted together with ED simulations on 16 lattice sites and shows reasonable agreement. Every data point is averaged over six different detuning phases ϕ and the numerical simulations are averaged over ten random phases and eight different initial state realizations. We attribute the offset between the experimental and numerical time traces to the effect of an external harmonic confinement. This increases the observed imbalance due to an additional source

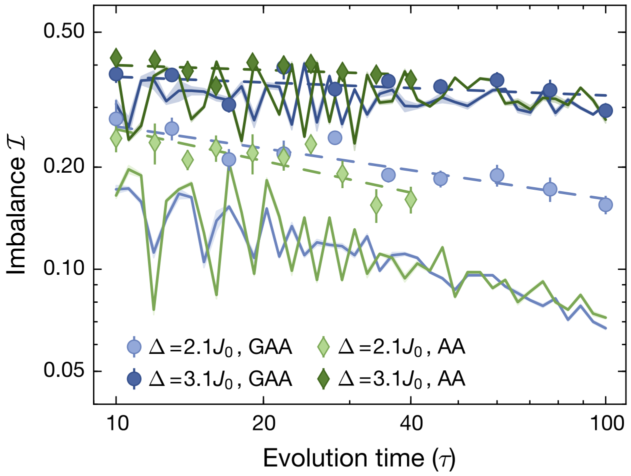

Figure 7.3.: Time evolution of the imbalance in the AA and GAA model: Measured imbalance time traces in the AA ($V_p = 8E_r^p$) and GAA ($V_p = 4E_r^p$) model for fixed interaction strength $U/J_0 = 1$. The dashed lines are power-law fits to the data and the solid lines are the numerical results including the uncertainty from averaging over random phases and different initial states.

of localization, in particular in the regime around the single-particle localization transition point and therefore explains why the trace at larger detuning are better described by the simulations.

The observed dynamics in the AA model at the different detuning strengths reveal the presence of a thermal (ETH) and a many-body localized (MBL) phase below and above the interaction-dependent critical detuning strength respectively. This notion is well established theoretically [24, 25] and experimentally [29, 48]. We note that the imbalance time traces of both models are indistinguishable within our experimental resolution regardless the particular regime under study. From the apparent similarity in the dynamics we infer that the GAA model possesses a many-body extended phase at weak detuning while for strong detuning the system is likely many-body localized. This is the first strong indication that MBL can exist in a system with a single-particle mobility edge for sufficiently strong detuning when all single-particle states are localized.

We now study the imbalance dynamics in more detail with the technique introduced in sec. 2.3. The traces are fitted with a power-law of the form

$$\mathcal{I}(t) = \mathcal{I}_0 t^{-\xi} \tag{7.2}$$

where $\mathcal{I}_0$ denotes the initial imbalance and ξ is the critical exponent. The fitting is performed on a doubly logarithmic axis where a power-law describes a linear function in order to weigh all points equally. There was a recent debate whether the power-law description is valid in the case of a quasiperiodic potential. In the real-random case it

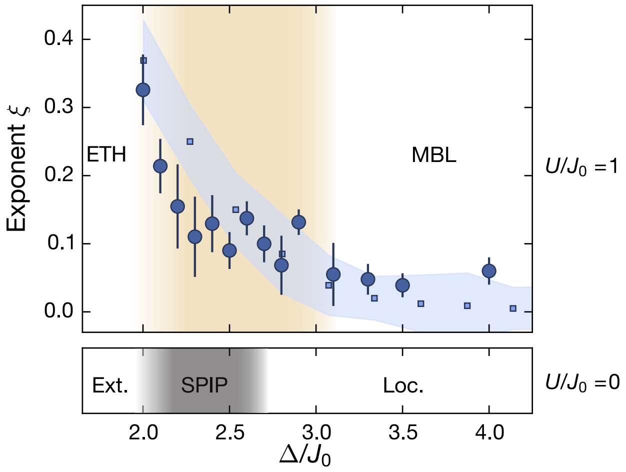

Figure 7.4.: Power-law exponents of the GAA model: Measured relaxation exponents as a funtion of the detuning strength. The top panel shows the results for the interacting case with $U/J_0 = 1$. We identify a thermal phase characterized by a fast imbalance decay below the single-particle transition at $\Delta/J_0 = 2$ and a localized phase with a constant background exponent. In the intermediate regime (brown shading) we find decreasing exponents with increasing detuning, a characteristic of critical dynamics. The experimental data is in good agreement with the numerical simulations including fit uncertainties indicated by the blue shaded region. The lower panel depicts the non-interacting situation with a single-particle extended and localized phase as well as the intermediate phase in the presence of an SPIP. The gray shaded region is the numerically predicted intermediate phase.

is well established that the Griffiths mechanism leads to an algebraic imbalance decay and subdiffusive transport [43, 44, 155]. This is related to locally insulating rare regions which slow down the particle transport. Such rare regions, however, are absent in the quasiperiodic case, so it is still an open question what process exactly applies in this case. A thorough discussion of the experimental data in the critical regime of the AA model as well as the theoretical debate on the analytical form of the decay (power-law, exponential or stretched exponential) is given in [48]. For our purposes though, we need a quantitative measure for the imbalance decay and although the power-law description may not be physically correct, it describes our data well over the observed time window.

The resulting exponents ξ as a function of the detuning are plotted in Fig. 7.4. Just above the single-particle transition point we observe an exponent of $\xi = 0.33(5)$ before it monotonously decreases for increasing detuning strengths. Finally, it converges to a constant positive plateau around $\Delta/J_0 = 3.0(2)$, which we perceive as the MBL transition point in this case although one would expect the exponent to vanish in the many-body localized phase. Experimental imperfections in the form of open system effects (see sec. 2.4) such as weak bath couplings due to off-resonant photon scattering [61] as well as coupling between adjacent one-dimensional tubes [60] lead to a finite lifetime and an overall decay of the imbalance. These effects are well understood, hence we attribute this result to imply that MBL is present in a model with a single-particle mobility edge when all single-particle states are localized. This determined transition point is, however, above the upper bound of the SPIP which spans between $1.7 \leq \Delta/J_0 \leq 2.6$ such that our findings suggest the existence of MBL only when all single-particle states are localized. However, this alone is not at all a trivial statement. While the AA model features MBL when all single-particle states are localized, this does not automatically apply to the GAA model as well since the Hamiltonian defining the time evolution is different. In order to make predictions about the nature of the many-body system it is not sufficient to study the corresponding model in the non-interacting regime. Indeed, in [213] a general criterion was sought to determine whether MBL exists in a model with an SPME and it was found that certain models feature MBL while others do not. Another striking example for the non-trivial properties of many-body systems are certain symmetry-protected topological phases, where it has been shown that finite interactions can enable topological phases although the corresponding non-interacting model is topologically trivial [214]. All in all, this observation underlines the non-trivial nature of the result.

It is tempting to ask whether MBL can also occur when not all single-particle states are localized, i.e. when the corresponding non-interacting system is in the intermediate phase. This is precisely the question studied in [170, 213] for various potentials. In order to gain an answer, it requires a model whose intermediate phase extends to larger detunings, closer to the experimental transition point. One way to accomplish this goal is to go to even shallower primary lattices, where the single-particle intermediate phase extends to even larger detuning strengths (see Fig. 7.5). Based on these considerations we take additional data at $3E_r^p$ primary lattice depth and compare it to the data obtained at $4E_r^p$ presented in Figs. 7.3 and 7.4. It is displayed in section 7.2.4 where the existence of the many-body intermediate phase is explored.

At this point it is important to emphasize that even shallower lattices are problematic for multiple reasons. First, in order to achieve sufficient detuning strengths in terms of Δ/J_0 would require the detuning lattice to be deeper than the primary lattice as soon as $V_p \leq 2E_r$ and $\Delta/J_0 \geq 2$. The clear distinction between the primary and detuning lattice as perturbation becomes meaningless. Second, the model in Eq. (6.1) is no longer valid as higher-order contributions have to be taken into account as their impact may easily become significant. This is particularly relevant in the context of long-range tunneling. The GAA model connects the tight-binding limit (where the AA model is formulated) with the continuum limit of the incommensurate lattice model. The presence of MBL in models with long-range tunneling [148] and in the continuum limit [215] is still under current theoretical debate and we do not want to enter this direction of research. Instead, it may be

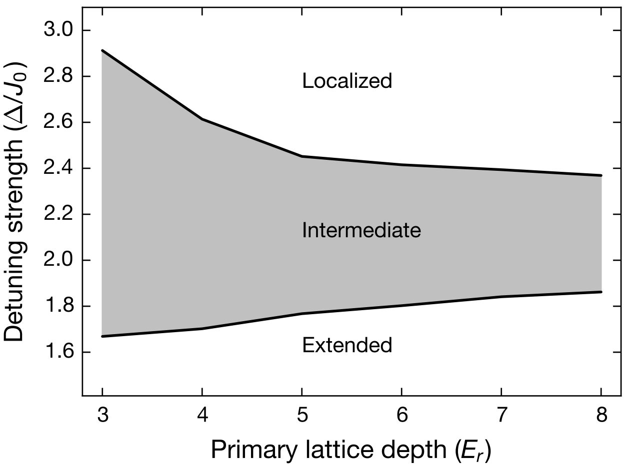

Figure 7.5.: Numerically determined width of the single-particle intermediate phase in the GAA model: The boundaries of the intermediate phase (gray shading) are determined from the IPR and NPR on a lattice with 369 sites. For deeper primary lattices the width of the intermediate phase shrinks as we expect it to vanish in the tight-binding limit. Experimental data was taken at $V_p = 3, 4$ and $8E_r$.

worth considering other models which feature a broader intermediate regime while being feasible to implement in an actual experiment. A promising candidate in this direction is the one-dimensional Soukoulis-Economou model [216]. In addition to the primary lattice it requires two detuning lattices with the second having twice the wavelength of the first, but this is beyond the scope of this work.

7.2.4. Existence of a many-body intermediate phase

The second question we want to examine in this project concerns the possible existence of a many-body intermediate phase and the concomitant coexistence of localized and extended many-body states. As reviewed in sec. 7.1 this is a theoretically highly debated question without definite answers, usually limited by small system sizes or short times. We want to contribute experimentally to this issue given the size of our experimental system where we expect finite-size limitations to play a much smaller role. Starting point are the imbalance time traces and the corresponding relaxation exponents. By comparing the results for the GAA and AA models we gain insights into the different dynamics of models with and without a single-particle mobility edge.

Between the thermal and MBL phase we observe slow dynamics (indicated by the brown shaded region in Fig. 7.4), characterized by a decreasing exponent with increasing detuning. Such a behavior was previously observed in the AA model as well [48]. In our search for the many-body intermediate phase we focus on the decay dynamics in this regime since the non-interacting GAA model has its intermediate phase at these detuning values, concretely up to $\Delta/J_0 \approx 2.6$ as indicated in Fig. 7.5.

As explained in sec. 7.1 there are three potential scenarios for the fate of a single-particle intermediate phase. On the one hand, a new many-body phase may come about by the emergence of a many-body mobility edge or in a more general form of an MBIP like the non-ergodic metal. On the other hand, is was argued that such a phase cannot exist in the thermodynamic limit due to the resonant spreading of thermal bubbles hybridizing the localized states. In this context a plausible point of view is, that the absence of such an intermediate phase may express itself in the dynamics in terms of an accelerated decay towards thermal equilibrium as compared to a model which does not possess an SPME. When coupling coexisting localized and extended states, the latter may act as a bath for the localized states, which is known to thermalize the system [55, 56], provided that the coupling is large enough and the bath has sufficiently many degrees of freedom. We investigate this assumption by directly comparing the relaxation exponents of the AA and the GAA model since such a thermalization process should be absent in the latter model. The results are shown in Fig. 7.6 for weak and intermediate interaction strengths. The data points are interpolated with a guide to the eye defined as the heuristic fit function

$$\xi(\Delta) = \begin{cases} a(\Delta - \Delta_*)^2 + \xi_0, & \text{if } \Delta \leq \Delta_* \\ \xi_0, & \text{if } \Delta > \Delta_* \end{cases} \tag{7.3}$$

which is a good description of the experimental relaxation exponents. Δ_* denotes the critical detuning strength above which the exponents reach a plateau ξ_0 and a is a scaling fit parameter. In analogy to previous works [41, 48] this point Δ_* can be related to the critical point of the MBL transition.

Below the critical point the decay exponents of the AA model are consistently higher, but this offset can be explained by an averaging effect in our experiment as we explain in sec. 7.2.5. Taking this systematic effect into account we conclude that within the experimental uncertainties the models are practically indistinguishable across all investigated detuning strengths. This leads to the conclusion that on the experimentally accessible time scales the presence of extended single-particle states does not lead to an accelerated thermalization of the many-body system at any detuning strength. Thus, this outcome is not in contradiction to the existence of a many-body intermediate phase following the picture from above.

While the appearance of an MBIP was mostly studied for the regime of weak interactions ($U/J_0 = 1$) where they can be treated perturbatively, another possible mechanism leading to the existence of an MBIP was suggested to be observed at strong interactions in an

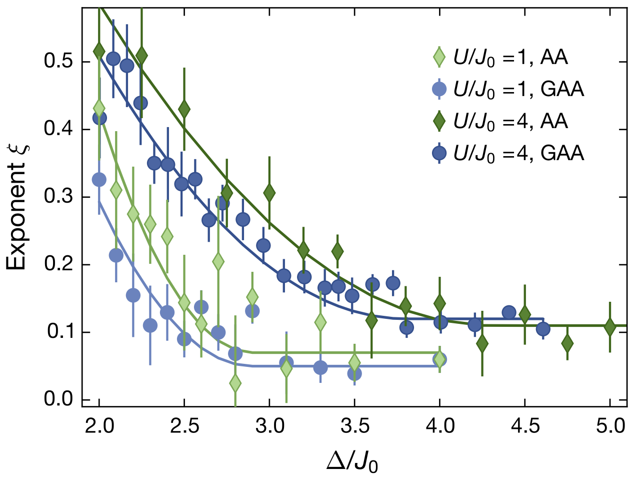

Figure 7.6.: Comparison of relaxation exponents in the GAA and AA model: Direct comparison of the power-law exponents in both models and two different interaction strengths. Error bars denote the standard error of the mean from six averages and solid lines are obtained from the heuristic fit function in Eq. (7.3) and serve as guides to the eye.

anisotropic XXZ-chain in a random magnetic field [217]. The mechanism relies on constrained dynamics due to the conservation of the total spin. The interplay between strong interactions and the symmetry gives rise to an energy-dependent localization transition. This view is in contrast to the studies focusing on weak interactions where the appearance of a many-body mobility edge is based on perturbative arguments [12]. Intrigued by this possibility, we investigate this assumption by measuring the data set at $U/J_0 = 4$ where the interactions can no longer be regarded as a perturbation parameter compared to the detuning. The resulting relaxation exponents are presented in Fig. 7.6 together with the previous $U/J_0 = 1$ data. While we observe overall larger exponents and a shift of the transition point to a higher detuning strength, the general result is basically the same. Even for the case of strong interactions we find remarkably similar dynamics and exponents such that our conclusions apply to both interaction strengths.

Additional experimental data

In our GAA model we found that MBL is present when all single-particle states are fully localized. Moreover, a thorough analysis of the data taken at $4E_r^p$ and $8E_r^p$ does not reveal any evidence for the existence of a many-body intermediate phase. In order to increase the difference between both regimes and to have a broader SPIP, we take additional data at $3E_r^p$ and $U/J_0 = 1$. Like in the investigation above, we take imbalance time traces between 10τ and 100τ and fit a power-law to extract the decay exponent. One tunneling time is

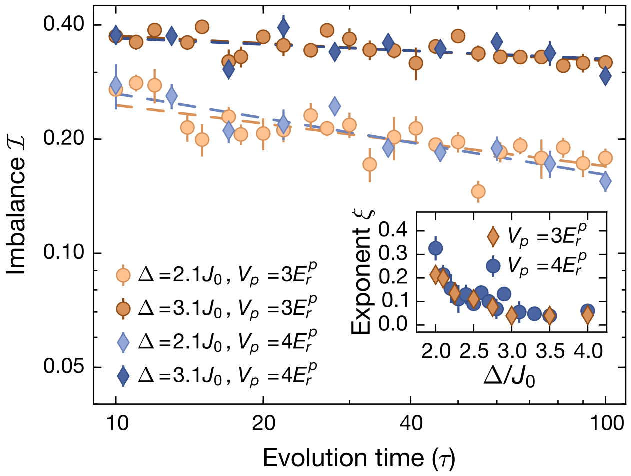

Figure 7.7.: Comparison of the data at $3E_r^p$ and $4E_r^p$: Imbalance time traces at two different detuning strengths Δ/J_0 and interaction $U/J_0 = 1$. The dashed lines are power-law fits. The inset shows those relaxation exponents obtained from the fit as a function of the detuning. All data points are averaged six times with error bars representing the standard error of the mean.

approximately 81 µs such that the total observation time is still comparable to the other cases.

In Fig. 7.7 we compare the time traces and exponents at the different lattice depths as a function of the detuning. Within the experimental uncertainty no difference can be detected between the data at $3E_r^p$ and $4E_r^p$. Hence, the broader intermediate regime does not express itself in the relaxation dynamics such that our conclusions regarding the many-body intermediate phase remain unchanged.

Numerical results and simulations at longer evolution times

The numerical simulations accompanying the project are carried out for system sizes of $L \leq 16$ and implement the Hamiltonian from Eq. (6.1) directly, thereby matching our experimental setup as closely as possible. Simulations for larger systems are prohibitively difficult due to the exponential growth of the Hilbert space. The initial CDW state is fixed to have zero magnetization and quarter filling ($L/4$ fermions in spin up and down each, this restricts the system size in the simulations to be multiples of four), in particular no double occupancies are allowed. Every imbalance calculation is averaged over eight initial state realizations (spin scrambling) and ten random phases ϕ. One particularity is that in the numerics we consider the real AA model by setting higher-order corrections from Eq. (6.1) to zero and keeping $4E_r^p$ primary lattice depth, while in the experiment these are finite in the $8E_r^p$ primary lattice.

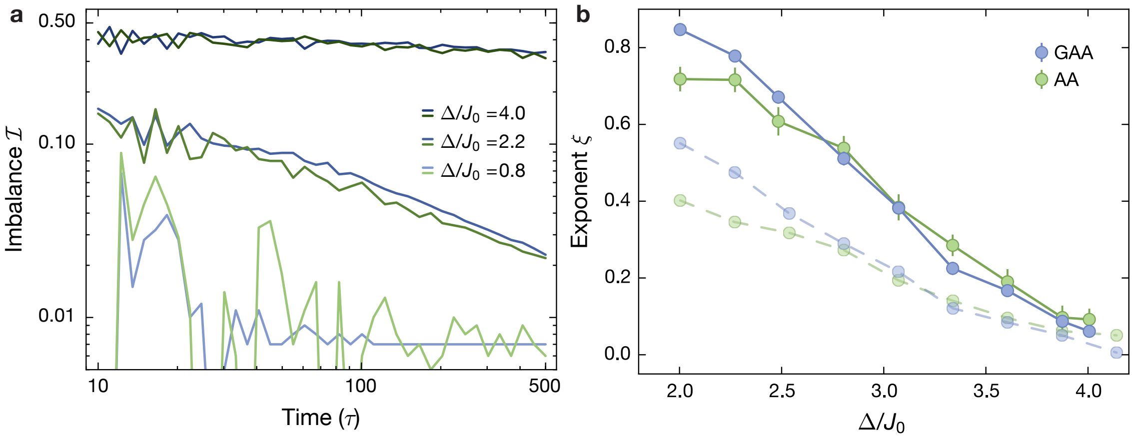

Figure 7.8.: Numerical investigation of the long-time dynamics: a Imbalance evolution in the GAA and AA model for fixed interaction strength $U/J_0 = 4$. The AA model is represented by the green lines and the GAA model by the blue ones. The traces for the weakest detuning remain finite due to finite-size errors. **b** Fitted relaxation exponents ξ including the uncertainties for $L = 16$. The dashed line indicates the numerical exponents for $L = 12$. Error bars denote the numerical uncertainty from averaging over eight spin configurations and ten detuning phases.

Due to the finite-time limitations of our experiment we extend our simulations of the quench dynamics to longer times ($> 100\tau$) with the goal to resolve qualitative differences between the models. This complementary study is motivated by the possibility that the interaction between localized and extended states is only weak and hence longer timescales are required. Fig. 7.8a shows numerical imbalance time traces, the detuning strengths are chosen such that we compute one time trace for each of the single-particle regimes (extended, intermediate, localized) for both models to have a direct comparison. The weakest detuning $\Delta/J_0 = 0.8$ produces a thermal result where the imbalance immediately decays to a vanishing value. We attribute the small residual value to finite-size effects. On the contrary, in the case of large detuning ($\Delta/J_0 = 4.0$) the imbalance is large and basically stable, in agreement with an MBL phase. The traces in the intermediate regime ($\Delta/J_0 = 2.2$) exhibit the characteristic decay described above. Overall, we see here that the imbalances of the AA and GAA model are virtually indistinguishable, although in the intermediate case the GAA imbalance appears to be slightly higher. The trend we found in the non-interaction simulations (see sec. 6.2) is also present in the interacting system.

As explained above, we analyze the decay exponent ξ of the numerical time traces whose results are presented in Fig 7.8b. We obtain these exponents from a power-law fit (see Eq. 7.2) to the numerical imbalance time traces in the time range between 100 and 500τ. For large detuning they are in agreement with our experimental results at shorter times and predict the presence of MBL. In the intermediate regime between $2.0 \leq \Delta/J_0 \leq 2.6$

the numerics suggest that the GAA exponents are slightly larger than the AA exponents. This signature may indeed hint towards an accelerated thermalization in the presence of extended many-body states and an absence of a many-body intermediate phase. Unfortunately, the validity of these statements is only limited due to finite-size effects. This becomes evident from a comparison of the numerical exponents for $L = 12$ and $L = 16$ in Fig. 7.8b. Not only do the absolute values strongly depend on the system size, also the difference in the dynamics of both models becomes smaller for larger systems. This suggests that the effect of an intermediate phase or even its presence may vanish in the thermodynamic limit and is only a finite-size effect after all. Though, it has to be concluded that the accessible system sizes are too small to make concrete statements. For $\Delta/J_0 > 2.6$ the exponents of both models agree and converge to zero at large detunings. These results are in agreement with the ones obtained at shorter times as well as from the experimental data.

7.2.5. Experimental imperfections

Up to this point, we considered our experiment as one-dimensional, but the unavoidable open-system effects caused by inter-tube coupling [60] and photon scattering [61] limit our experimental observation times to about 10 ms. Additionally, technical sources such as amplitude and frequency noise of the optical lattices lead to atom loss on time scales on the order of 1000τ and hence play a minor role on the time scales accessed in this experiment. However, these contributions are difficult to estimate quantitatively. Another systematic effect of the experiment stems from the fact that we generate a three-dimensional optical lattice which is split into individual one-dimensional tubes via deep perpendicular lattices such that the orthogonal tunneling rate $J_\perp$ is suppressed by about three orders of magnitude. However, due to the Gaussian-shaped intensity profile of the laser beams with a beam waist around 150 µm, inner and outer tubes have slightly different values of V_p and V_d. The bandmapping sequence during our final state detection averages over all one-dimensional tubes, yielding the average dynamics of 1D systems with different lattice depths weighted by the respective atom numbers.

Via in-situ images of the atomic cloud in the lattice we extract a size of about 42 µm in the horizontal x-y-plane and about 12 µm along the vertical z-direction. With this information an atom number distribution and effective detuning strength as a function of the relative lattice depths V_p and V_d can be derived, as shown in Fig. 7.9. Outer tubes evidently feature a weaker detuning strength because both a shallower detuning lattice and primary lattice (via an increase of J_0) lead to a reduction of the relative detuning strength Δ/J_0. This effect depends on the primary lattice depth and is even enhanced for deeper primary lattices due to the non-linear scaling of the tight-binding parameters (see also Tab. A.1 in the

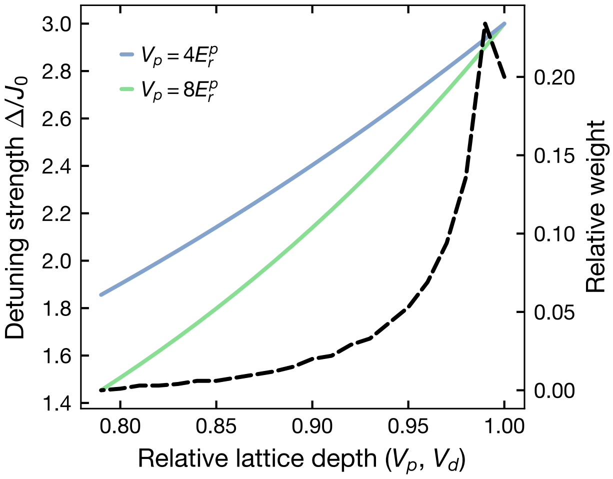

Figure 7.9.: Impact of tube averaging: Distribution of the detuning strength Δ/J_0 as a function of the relative lattice depth, the central tube is set to $\Delta/J_0 = 3.0$. The tube averaging effect is apparently amplified for deeper primary lattices. The black dashed line shows the relative weight of the one-dimensional tubes as a function of the relative lattice depth corresponding to the respective atom number.

appendix). The computation of the tube-dependent detuning strength is also plotted in Fig. 7.9. In an extreme case, this can lead to a situation where the single-particle states in the center are localized while the outer ones see a detuning below the transitions and are hence extended.

This tube averaging effect presumably has some impact on our experimental imbalance measurement. First, from the relaxation exponents in Fig. 7.4 we see that a weaker detuning leads to a larger relaxation exponent in the intermediate regime where slow dynamics are observed. Tube averaging consequently results in a larger exponent ξ as compared to a homogeneous system. Moreover, the effect becomes stronger for deeper primary lattices such that we expect the AA model to see a larger effect since it is realized with $V_p = 8E_r^p$ as opposed to the GAA model $V_p = 4E_r^p$. The expected offset between both models induced by tube averaging can be approximated by a weighted average of the exponents from Fig. 7.4 and it turns out to be about 0.04 for $2.0 \leq \Delta/J_0 \leq 3.0$. Indeed, a small offset of the exponents between the models in Fig. 7.6 is observed which is likely explained by the tube averaging effect. Though, the conclusion about the similarity of the relaxation dynamics in both models remains unchanged.

7.3. Conclusion and outlook

In summary, we realized the interacting GAA model beyond the tight-binding description with a single-particle mobility-edge in the non-interacting limit. At large detuning strength we found evidence for a many-body localized phase at sufficiently strong detuning when all single-particle states are localized. This is a non-trivial result since it is impossible to relate the single-particle properties of a system to the many-body case. The transition point itself is indistinguishable from the one found in the AA model within our experimental resolution. It is worth mentioning that the absence of MBL in models with an SPME would have ruled out the possibility of having MBL in realistic 3D systems because generic three-dimensional models possess a mobility edge [218, 219].

An investigation of the relaxation dynamics in both models at multiple detuning and interaction strengths reveals that they are very similar on short timescales, suggesting that the presence of extended states does not serve as an efficient heat bath for the probed initial states and evolution times. While these observations do not rule out the existence of an MBIP, the significance of the experimental findings is limited due to external baths. Moreover, the imbalance as a single observable may not be sufficient to probe the characteristic properties of the many-body intermediate phase. One approach could be to have multiple complementary observables to detect extended and localized many-body states in analogy to the technique employed in [119] for the respective single-particle system. Potential candidate observables include the detection of transport properties like the expansion of the cloud or the DC conductivity. The former serves well on the single-particle level, it is unsuited in the interacting case because in order to detect a sufficient transport distance in our experiment, the sample has to expand considerably. Not only is this process extremely slow as demonstrated in [119], but it also makes the ensemble more dilute and thereby changes the local energy density as a function of time. Instead, it was suggested to study entanglement entropy or observables on the eigenstate level although the latter may be hard to access in an experiment. A measurement of the AC conductivity in a quantum gas experiment has been proposed theoretically [156] has been demonstrated in [220]. Though, due to open system effect we might be limited in the low-frequency response of the system.

One worthwhile direction of future research is the exploration of the origin of slow dynamics in both models. While the dynamical properties of the AA model close to the phase transition were probed previously [48], the underlying mechanism is still under debate. In the real-random Anderson model there is the Griffiths effect relying on locally insulating or thermal regions induced by islands of strong or weak disorder. Such regions are absent in the quasiperiodic model and the Griffiths effect cannot be used to explain the observation of slow dynamics. However, in the experiment there is a randomness in the initial state, which may produce local spin-polarized regions which have to be slowly thermalized by the surrounding system when the disorder is stronger than the single-particle localization point. In our study, it was assumed that the intermediate regime of slow dynamics is caused by different mechanisms in both models studied, but it may well be that they are of similar physical origin. This process is not yet fully understood [221] and requires further investigation. Moreover, it is important to access longer evolution times to study other mechanisms that are suggested to lead to a potential delocalization of an MBL system. While the charge sector is localized by the detuning potential, the spin sector is free to move via spin flips between neighboring sites and can lead to spin diffusion in our SU(2) symmetric system, ultimately leading to delocalization [222–226]. Though it is presumably a slow process happening on time scales far beyond experimental limitations. Thus, while a spin-dependent detuning potential may be relevant for the appearance of full MBL in general, it is only of minor significance for experimental studies of this subject.

Part IV.

Ultracold atoms in linear potentials

Since the seminal work by Wannier it is known that a single-particle system in a linear external potential has exponentially localized eigenstates. The physics of the interacting model, however, is less clear and has recently been explored exhaustively. It was found that tilted lattice systems bear a great relevance in the context of weak ergodicity breaking. At leading order in perturbation theory the tilted Fermi-Hubbard model displays similar terms that appear in dipole-conserving setting, which exhibit Hilbert space fragmentation and thus fail to thermalize as their Hilbert space is shattered into exponentially many disconnected subsectors. In this part we report on the experimental realization of a tilted Fermi-Hubbard model and the observation of state-dependent dynamics. Together with simulations of the corresponding effective Hamiltonian we show that our observations are in agreement with the implementation of a fragmented model in our experimental system.

8. The Wannier-Stark ladder

In the second project reported in this thesis we investigate the dynamical properties of the Fermi-Hubbard model in the presence of a linear external potential. While the interacting model is currently an active research area and also explored thoroughly in chapter 9, the corresponding single-particle model is well understood as the well-known Wannier-Stark ladder [158], also called Stark model in the literature. It owes its name to the energy level structure that displays highly degenerate equidistant levels separated by the tilt energy. This chapter only briefly summarizes the relevant properties of a single particle in a tilted lattice, a more detailed investigation can be found in [133, 227]. We exploit the availability of analytical solutions to calibrate our experimental parameters with high accuracy, a prerequisite for our understanding of the corresponding interacting model.

8.1. The Stark model and its properties

The fermionic Stark model describes a lattice in the tight-binding limit superimposed with a linear external potential and is given by the Hamiltonian

$$\hat{H} = -J \sum_{i,\sigma} (\hat{c}^{\dagger}_{i,\sigma} \hat{c}_{i+1,\sigma} + \text{h.c.}) + \sum_{i,\sigma} \Delta_{\sigma} i \hat{n}_{i,\sigma} \tag{8.1}$$

with the tunneling element J and the state-dependent tilt Δ_σ. This setting is illustrated schematically in Fig. 8.1a highlighting the Hubbard parameters. Note that the compensation of the spin-dependent tilt is an integral part of the project reported in chapter 9 and the corresponding experimental technique of RF-dressing is explained in sec. 4.4.3. Hence, in the following we will use a common tilt Δ for all spin components to simplify the discussion as it is irrelevant for the physics of the non-interacting model. Since this Hamiltonian from Eq. (8.1) was studied analytically in a previous thesis [133], only the key results important for the reported project are revised. The main characteristic of the Stark model is that all eigenstates are localized for any finite tilt strengths irrespective of their energy, the same situation, which also occurs in the Anderson model. In particular, the model does not have a single-particle mobility edge. The eigenstates, also called Wannier-Stark states, from the center of the spectrum are shown in Fig. 8.1b for three

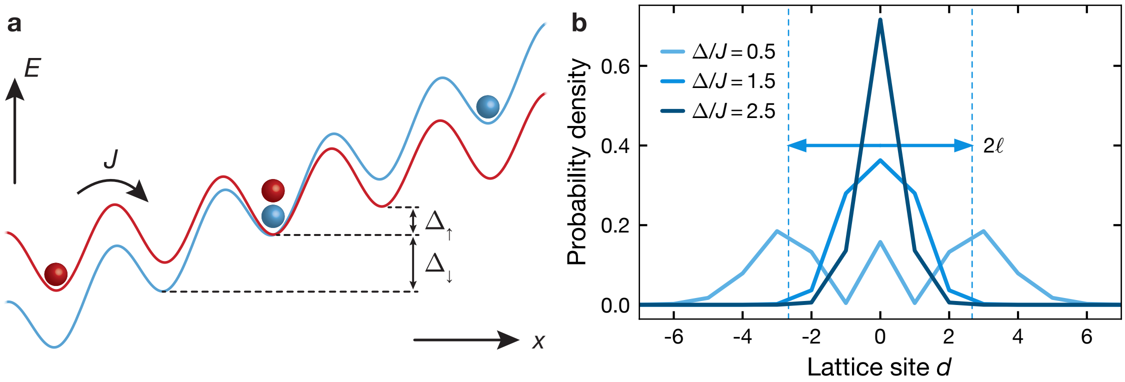

Figure 8.1.: Visualization of the Stark model: **a** Schematic illustration of the Hamiltonian in Eq. (8.1). x is the spatial coordinate and E denotes the energy. Colors represent different spin states. It further visualizes the spin-dependent tilt Δ_σ that can be tuned via RF dressing. **b** Eigenstate probability density of the Wannier-Stark ladder for three different values of the tilt. Evidently, they are localized for all tilt strengths and the localization length ℓ for the intermediate tilt strength is illustrated by the dashed vertical lines. The presented states are picked from the center of the energy distribution.

different values of the tilt. Apparently, the wavefunction is localized on fewer and fewer lattice sites when the ratio of tilt and tunneling Δ/J is increased. In fact, this extent ℓ is analogous to the localization length in disordered lattices and can be approximated by the expression $\ell \simeq 4Jd/\Delta$ with the lattice spacing d as illustrated in Fig. 8.1b. In the limit of infinite tilt the eigenstates of the Stark model converge to the Wannier functions, the localized eigenstates of the lattice.

A single particle initially spatially localized undergoes periodic breathing dynamics around its fixed center of mass and with an oscillation amplitude given by the localization length ℓ. The oscillation frequency thereby matches the tilt. From the analytical solution of the probability density we can derive the imbalance as a function of time. It can be written in the analytical form

$$\mathcal{I}(t) = \mathcal{J}_0\left[\frac{8J}{\Delta}\sin\left(\frac{\pi\Delta t}{h}\right)\right] \tag{8.2}$$

with the zeroth order Bessel function of first kind $\mathcal{J}_0$ and yields a parity-projected observable probing the localized real-space dynamics. In the limit of large tilt that is realized in our experiment ($\Delta/J = 8$) the atoms are strongly localized around their original lattice site and we can approximate the expression in Eq. (8.2) by expanding the Bessel function up to second order yielding $\mathcal{I}(t) \approx 1 - \sin^2(\pi\Delta t/h)/4$. Hence, we observe nearly sinusoidal Bloch oscillations with the frequency given by the tilt. For weaker tilt strengths the particle extends over multiple lattice sites such that higher frequency components enter the expression and the coherent imbalance dynamics become richer with additional oscillation features within one Bloch cycle [117, 133].

While the preceding discussion applies to a perfect system, the experimental setup inevitably has certain imperfections that affect the outcomes. Most prominent among them is the harmonic confinement originating from the Gaussian shaped beams of dipole traps and lattices. It modifies the Hamiltonian and adds a quadratic correction to the external potential according to $\alpha \sum_i i^2 \hat{n}_i$ such that the tilt becomes space dependent: $\Delta_\sigma(i) = \Delta_\sigma + 2i\alpha$. This local curvature is much weaker than the tilt, typically suppressed by about three orders of magnitude. Hence, the individual dynamics of the atoms are not affected within the oscillation period, but the imbalance, as it averages over the entire system, records a sum of oscillations at slightly different frequencies. This results in the familiar case that the dynamics start dephasing after a collapse time $T_c \approx 1/(2\alpha L)$ and finally revive when all oscillations are back in phase [133] for the same reason it was observed for matter wave fields and Rabi oscillations of a coherent state [228, 229]. Therefore, the Bloch oscillations recorded in the experiment exhibit a damped envelope. The revival dynamics are not observed experimentally because additional noise sources such as lattice or magnetic field noise irretrievably decohere the oscillations. It is therefore of interest what steady-state value the imbalance attains when the oscillations are dephased. In order to calculate this expression, one starts from a density-matrix approach where all off-diagonal elements, representing the coherences, are manually set to zero. This results in the steady-state imbalance of the Wannier-Stark model that solely depends on the tilt and obeys the simple relation

$$\mathcal{I}_\infty(\Delta) = \mathcal{J}_0^2\left(\frac{4J}{\Delta}\right). \tag{8.3}$$

Not only is this function strictly non-negative, but also possesses poles for $\Delta/J \leq 1.5$. However, this does not imply that the states are delocalized. Instead, their weight on even and odd lattice sites is equal as can be seen in Fig. 8.1b for the case of intermediate detuning. These characteristics of the Wannier-Stark ladder, namely the Bloch oscillations and steady-state imbalance, will be used as a tool to calibrate our experimental system as described in sec. 8.3.

8.2. Experimental implementation

The implementation of a linear potential as included in the Hamiltonian in Eq. (8.1) has been realized in previous quantum gas experiments. Most often the setups were designed such that the dynamics happen along the vertical direction. The lattice is then superimposed with the gravitational potential [97, 98] resulting in a nearly perfectly linear dependence of the energy on the position that is independent of the atom's internal state. However, the achievable tilt is rather weak (on the order of the tunneling J in our experiment) compared to other methods and it requires means like an inhomogeneous field for magnetic levitation to tune the tilt seen by the atoms.

Another approach is the optical implementation of a potential gradient via the AC-Stark shift of an intense laser beam [99, 100]. Its Gaussian profile has a nearly linear slope 1σ away from the center that serves as the external potential. Hence, this technique requires that the atoms are overlapped with the tilt beam that is misaligned by the right amount with respect to the center. Depending on the available laser power and detuning this method can realize large values of the tilt, but is only reliable for small system sizes before the inhomogeneity of the tilt becomes relevant.

In our experiment we use the magnetic field generated by a single coil with 25 mm diameter, 20 windings and a mean distance of 26.5 mm from the atomic cloud [133, 187]. Besides a large homogeneous part, the resulting magnetic field possesses a strong linear component that takes the role of the tilt. Higher order terms are also present, although with a negligible amplitude, and add up with the harmonic confinement and can be seen in the dephasing of the Bloch oscillations. The tilt induced by the magnetic field is $dE(B)/dB \cdot \partial_x B(x)$. Herein $E(B)$ is the energy of the atomic state in the presence of a magnetic field according to the Breit-Rabi equation. In small magnetic fields below the Paschen-Back limit the energy depends on the magnetic hyperfine state m_F. Therefore, the different spin states in the experiment, encoded via m_F do not see the same slope. Note that this technique was employed in a previous experiment where the tilt difference was used as a tool to study spin-dependent transport in a two-dimensional Fermi-Hubbard model [230]. The tilt difference induced by the magnetic moments of the respective spin state can be compensated with the technique of RF dressing (see sec. 4.4.3) and set to any value between close to zero, resulting in an average tilt of $\bar{\Delta} = (\Delta_\downarrow + \Delta_\uparrow)/2$, and the naturally given value of about 11 %. We can achieve tilts of up to $h \cdot 1.9\,\mathrm{kHz}$ over several hundred tunneling times before running into current limitations, which corresponds to about $8.5J$ in a primary lattice with a depth of $12E_r$.

Note that in order to set the correct interaction strength around the Feshbach resonance via the vertical magnetic field B_z, the field along the horizontal direction B_x composed of a constant part B_{x0} and the linear contribution generated by the gradient coil has to be taken into account. The total field generated by this configuration is

$$B_{tot}(x) = \sqrt{B_z^2 + B_x^2} = \sqrt{B_z^2 + \left(B_{x0} + x \cdot \frac{dB_x}{dx}\right)^2} \simeq B_z + \frac{B_{x0}^2}{2B_z} + \frac{B_{x0}}{B_z} \cdot x \cdot \frac{dB_x}{dx} \tag{8.4}$$

where we used that the vertical field is the largest contribution to expand the square root and we neglected the squared contribution of the gradient. This expression directly reveals that one obtains an additional homogeneous contribution that needs to be compensated.

Moreover, the linear potential gets suppressed by the vertical field and amplified by the longitudinal homogeneous part. Thus, setting the correct slope of the external potential and the appropriate vertical field to obtain the desired interaction strength is an iterative process and requires multiple steps to converge because both quantities of interest depend of each other. The calibration process and the experimental implementation of this procedure are reported in [117, 133]. Finally, the magnetic field is space-dependent which causes a variation of the interaction strength across the atomic cloud. This effect is treated quantitatively in sec. 9.3.5.

8.3. Calibrations and reference measurements

Measurements in the non-interacting tilted Fermi-Hubbard model conceal essential information that is of larger interest for the respective quantum many-body system. In this project we employ reference measurements on the non-interacting or even spin-polarized system in order to access and calibrate the Fermi-Hubbard parameters, namely the tunneling element J and the tilt Δ_σ. For this purpose we exploit that the Wannier-Stark ladder provides analytical functions for the Hubbard parameters that can be used to retrieve the aspired information. In a first step we record Bloch oscillations with a spin-polarized gas in the $|\downarrow\rangle$-state to eliminate all interaction effects. As follows from Eq. (8.2), the periodicity of the imbalance evolution solely depends on the tilt, whereas the amplitude of the oscillations is set by the ratio between tilt and tunneling element. We simulate the dynamics including the harmonic confinement by directly solving the non-interacting Hamiltonian using exact diagonalization. From this we can retrieve fit values for J, Δ and α by fitting it to the experimental traces as shown in Fig. 8.2a. By repeating this measurement for multiple values of the tilt as well as for both spin components, we can reliably calibrate Δ across the entire experimental range. Note that this method is not really suited to fit J. The tunneling is very sensitive to the amplitude and due to the decay it is very prone to errors. Only for about the first two periods the fit value is in good agreement with the theoretical expectation, but this short time window is in general not sufficient to obtain an accurate value for the tilt. Moreover, from the fitted collapse time of $T_c = 11.0\,\mathrm{ms}$ we extract a local curvature on the order of $\alpha = h \cdot (2LT_c)^{-1} \approx h \cdot 0.2\,\mathrm{Hz} \approx 10^{-3}J$. Hence, the local potential variation due to the confinement is indeed negligible.

Second, once the tilt is known precisely, we can make use of the relation in Eq. (8.3) to extract the tunneling element J from the steady-state imbalance. After the dephasing of the Bloch oscillations, the non-interacting system adopts a plateau imbalance value as shown in the inset of Fig. 8.2a. We extract this plateau value as a function of the tilt and show the result in Fig. 8.2b. We directly fit the function Eq. (8.3) and retrieve J as a fit

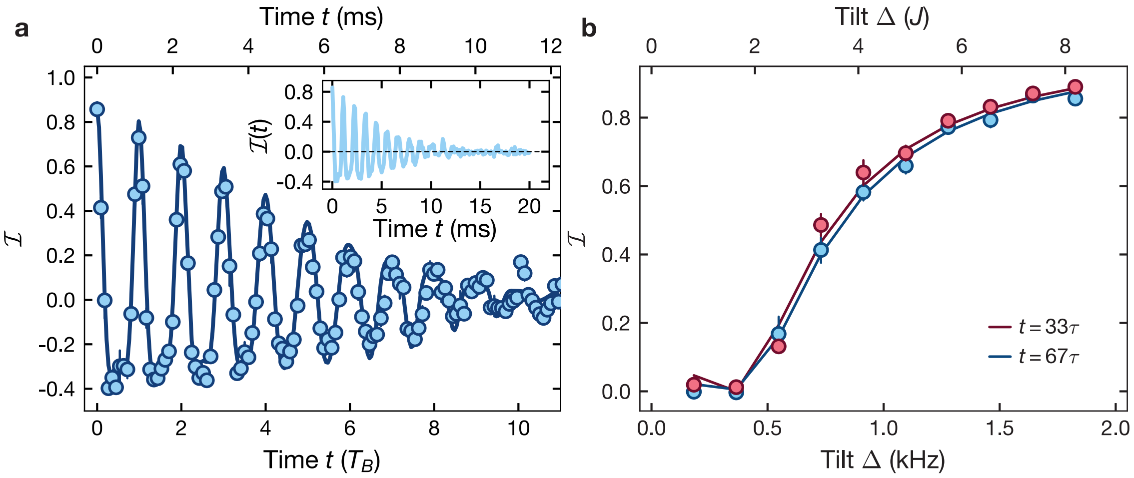

Figure 8.2.: Calibration measurements in the non-interacting model: a Real-space Bloch oscillations of a spin-polarized Fermi gas. The solid line represents a numerical simulation including the harmonic confinement from which the tilt Δ can be extracted. The obtained dephasing time is $11.0\,\text{ms} = 12.2T_B$. In the inset we show the time trace up to longer times reaching its steady-state value, that matches the prediction from Eq. (8.3) (dashed line) very well. **b** Steady-state imbalance as a function of the tilt after two different evolution times. Solid lines are fits with the analytical function in Eq. (8.3) to extract the tunneling element J. Error bars denote the standard error of the mean obtained from six averages.

parameter. After 33τ we obtain $J = h \cdot 223(4)\,\text{Hz}$ and after 67τ it is $J = h \cdot 233(2)\,\text{Hz}$. For a perfect system with a primary lattice depth of $12E_r$ one expects $J = h \cdot 216\,\text{Hz}$, so we understand the experiment quite precisely. This measurement was performed for two different evolution times to ensure that there are no decay mechanisms that could forge the experimental data. However, the extracted tunneling elements almost agree within the experimental uncertainty such that we can safely assume the non-interacting to be stable on the timescales under study.

9. Non-ergodicity and state-dependent dynamics due to Hilbert-space fragmentation

The second project of this thesis also explores another regime in the spectrum between thermal and integrable systems (see Fig. 3.1). The experimental goal in this project is the demonstration of state-dependent dynamics in the strongly tilted Fermi-Hubbard model and the description of this observation in terms of a leading order effective Hamiltonian. This will serve as strong indication that we indeed realize a fragmented model in our experiment. Although recent experimental works provided evidence for non-ergodicty in the presence of a tilted external potential [117, 231, 232], one of the central features of Hilbert space fragmentation, namely initial-state dependent dynamics, has not been demonstrated yet. In this work we realize different families of initial states characterized by the doublon fraction and probe the subsequent dynamics via the singlon, doublon and charge imbalance. These traces are reproduced by a fragmented effective Hamiltonian. Supported by complementary numerical observables we further investigate the kind of dynamics within individual fragments.

In the following we will introduce the concept of an effective Hamiltonian that will be used to describe the dynamics at leading order in perturbation theory. After explaining the important experimental techniques including the initial state preparation and characterization we present our experimental results and their interpretation.

9.1. Hilbert space fragmentation in the tilted Fermi-Hubbard model

In sec. 3.2 we introduced the field of Hilbert space fragmentation as a mechanism of weak (or even strong) ergodicity breaking from the viewpoint of previous theoretical studies in spin systems and random unitary circuits. While in those systems the central ingredients for fragmentation, namely U(1)-charge and dipole moment conservation as well as local interactions, are explicitly engineered, they naturally occur in the strongly tilted spin-1/2 Fermi-Hubbard model when expanding the Hamiltonian in perturbation theory up to leading order. This results in a description in terms of an effective Hamiltonian that directly satisfies the conservation laws required for fragmentation. Here we show the correspondence between both models and elaborate on how we can investigate the underlying physics in our quantum gas experiment. We first recall the Hamiltonian of the two-component Fermi-Hubbard model with on-site interactions and a linear external potential given by

$$\hat{H} = -J \sum_{i,\sigma} (\hat{c}^{\dagger}_{i+1,\sigma} \hat{c}_{i,\sigma} + \text{h.c.}) + U \sum_{i} \hat{n}_{i,\uparrow} \hat{n}_{i,\downarrow} + \sum_{i,\sigma} \Delta_{\sigma} i \hat{n}_{i,\sigma}, \tag{9.1}$$

with the hopping element J, interaction strength U and tilt Δ_σ. The latter is in general spin-dependent (index σ), but we can approximately compensate this effect with our technique of RF dressing (see sec. 4.4.3). Thus, we omit the spin-dependence in the following and use a common tilt $\Delta \equiv \Delta_\downarrow = \Delta_\uparrow$ for the remaining discussion. However, in sec. 9.3.3 we investigate the dynamics with spin-dependent tilt explicitly and develop an effective picture for that situation.

In certain limiting cases the Hamiltonian in Eq. (9.1) can be expanded in perturbation theory. This can either be achieved by a Schrieffer-Wolff transformation [233] or a high-frequency Magnus expansion. Details on the derivation can be found in [90, 117, 133], here we only give the final result relevant for the project and explain the appearing terms at leading order in perturbation theory.

In the limit of large tilt and weak interactions ($\Delta \gg |U|, J$) the tilted Fermi-Hubbard Hamiltonian (Eq. 9.1) can be expanded in powers of $1/\Delta$ to obtain an effective Hamiltonian $\hat{H}^{\text{dip}}_{\text{eff}}$ at third order in perturbation theory that reads

$$\hat{H}^{\text{dip}}_{\text{eff}} = J^{(3)} \hat{T}_3 + 2J^{(3)} \hat{T}_{XY} + \tilde{U} \sum_{i} \hat{n}_{i,\uparrow} \hat{n}_{i,\downarrow} + 2J^{(3)} \sum_{i,\sigma} \hat{n}_{i,\sigma} \hat{n}_{i+1,\bar{\sigma}} \tag{9.2}$$

and preserves the total charge $\hat{Q} = \sum_i \hat{n}_i$ and dipole moment $\hat{P} = \sum_i i\hat{n}_i$. The central energy scale of this Hamiltonian is the effective tunneling rate $J^{(3)} = J^2 U / \Delta^2$. We have already encountered this third-order expression for a correlated hopping of two particles joining on the same lattice site in Eq. (3.9). Given that the effective hopping $J^{(3)}$ depends on the interaction strength, it is evident that dipole-conserving processes are generated by interactions and purely off-diagonal terms vanish due to destructive interference [117]. Moreover, the Hamiltonian predicts two types of correlated hoppings, namely the squeezing term $\hat{T}_3$ and the spin-exchange term $\hat{T}_{XY}$, which are given by

$$\begin{aligned}\hat{T}_3 &= \sum_{i,\sigma}(\hat{c}^{\dagger}_{i,\sigma}\hat{c}_{i+1,\sigma}\hat{c}_{i+1,\bar{\sigma}}\hat{c}^{\dagger}_{i+2,\bar{\sigma}} + \text{h.c.}),\\ \hat{T}_{XY} &= \sum_{i}(\hat{c}^{\dagger}_{i,\uparrow}\hat{c}_{i,\downarrow}\hat{c}^{\dagger}_{i+1,\downarrow}\hat{c}_{i+1,\uparrow} + \text{h.c.})\end{aligned} \tag{9.3}$$

and that are schematically illustrated in Fig. 9.1a. Note that the term $\hat{T}_3$ precisely corresponds to the pair hopping model introduced in sec. 3.2.1 that is known to feature dipole moment conservation and strong fragmentation as shown in [87, 88] up to additional spin degrees of freedom. This fact directly underlines the correspondence between the fragmented Hamiltonian studies in the respective section and the tilted Fermi-Hubbard model in the limit of large tilt. Already in the original Hamiltonian (Eq. 9.1) it is straightforward to see that it conserves the dipole moment for large tilt. In this case the term of the external potential $\hat{H}_\Delta = \sum_i \Delta i \hat{n}_i$ dominates and hence the Hamiltonian approximately commutes with $\hat{H}_\Delta$ making the dipole moment $\Delta \cdot \hat{P} = \hat{H}_\Delta$ a conserved quantity and leading to strong Hilbert space fragmentation [87]. One can thus introduce symmetry sectors defined by the dipole moment $\langle \hat{P} \rangle$ of the initial state. In the case of finite tilt the hopping terms with amplitude $J^{(3)}$ couple multiple symmetry sectors with different dipole moments. Hence, this conservation law is no longer exact such that the description in terms of a dipole-moment conserving effective Hamiltonian has to break down at exponentially long times while the effective description is appropriate on intermediate timescales. Instead, higher order terms have to be taken into account, which leads to weak fragmentation as explained in sec. 3.2.2.

It is worth mentioning that the effective Hamiltonian $\hat{H}^{\text{dip}}_{\text{eff}}$ and in particular the term $\hat{T}_3$ are SU(2)-invariant. This means that fragmentation occurs in infinitely many bases. The most relevant basis for the experimental description is the local S^z-basis where the incoherent initial product states are prepared.

Unlike previous theoretical studies of a closely related model [87, 88, 90, 95], our effective Hamiltonian in Eq. (9.2) contains a diagonal interaction term with amplitude $\tilde{U} = U\left(1 - 4J^2/\Delta^2\right)$ that leads to an effective conservation of the doublon number due to energy conservation when $\tilde{U} \gg J^{(3)}$. This is precisely the situation in our case since $J^{(3)}/\tilde{U} = 1/(\Delta^2/J^2 - 4) \simeq (J/\Delta)^2 \ll 1$ and hence the first process sketched in Fig. 9.1a starting with two singlons on adjacent even sites is suppressed. If however, a singlon and a doublon are adjacent on even sites, the process $\hat{T}_3$ can happen resonantly with hopping rate $J^{(3)}$. Though, doublon number is no conserved quantity of $\hat{H}^{\text{dip}}_{\text{eff}}$. While the dynamics are properly captured by the effective Hamiltonian, we have to enforce the doublon conservation manually in order to compute the correct dynamical fragments or

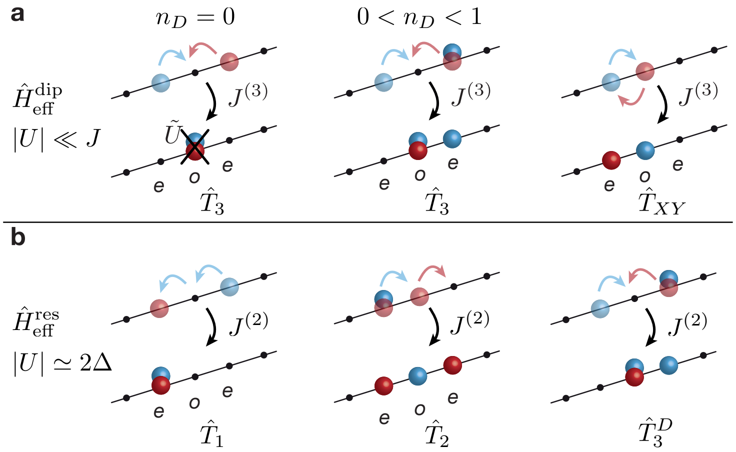

Figure 9.1.: Leading order hopping processes of the effective Hamiltonians: a Schematics of the correlated tunneling processes according to respective term of $\hat{H}_{\text{eff}}^{\text{dip}}$ in Eq. (9.2). Colored spheres represent different spin states, the upper row illustrates the initial, the lower row the final state. For a singlon initial state the first process is energetically suppressed. **b** Same for the resonant regime $U \simeq 2\Delta$ governed by the effective Hamiltonian in Eq. (9.5). All processes happen with the effective hopping rate of the respective Hamiltonian.

Krylov subspaces. For this purpose we replace the term $\hat{T}_3$ in Eq. (9.2) with

$$\hat{T}_3' = \sum_{i,\sigma} \left((\hat{n}_{i,\sigma} - \hat{n}_{i+2,\bar{\sigma}})^2 \hat{c}_{i,\bar{\sigma}} \hat{c}^\dagger_{i+1,\bar{\sigma}} \hat{c}^\dagger_{i+1,\sigma} \hat{c}_{i+2,\sigma} + \text{h.c.} \right). \tag{9.4}$$

Compared to Eq. (9.3) the resulting dynamics are more constrained and thus the relative fragment dimensions are smaller than without this additionally imposed conservation law.

While the limit $\Delta \gg |U|, J$ was studied numerically and analytically on previous occasions in the context of fragmentation, this is not the only regime of the Fermi-Hubbard model that exhibits fragmented characteristics. Triggered by experimental results reported for this model in the resonant regime $|U| \simeq 2\Delta$ and the subsequent theoretical exploration [117] we revisit this regime in the case of large tilt to study the fragmented nature of this model. On the resonance $|U| = 2\Delta$ and $\Delta \gg J$ the effective Hamiltonian is of second order in perturbation theory and reads

$$\begin{aligned} \hat{H}_{\text{eff}}^{\text{res}} = \hat{H}_0 + (U - 2\Delta) \sum_i \hat{n}_{i,\uparrow}\hat{n}_{i,\downarrow} + \frac{8J^2}{3\Delta} \sum_i \hat{n}_{i,\uparrow}\hat{n}_{i,\downarrow} - \frac{4J^2}{3\Delta}\hat{T}_{XY} \\ + \frac{J^2}{\Delta}\hat{T}_1 - \frac{2J^2}{\Delta}\hat{T}_2 + \frac{2J^2}{3\Delta}\hat{T}_3^D + \hat{H}_D. \end{aligned} \tag{9.5}$$

The effective Hamiltonian in this regime consists of three different kinds of correlated hopping processes defined by the terms $\hat{T}_1$, $\hat{T}_2$ and $\hat{T}_3^D$ illustrated in Fig. 9.1b and the relevant energy scale in this case is the effective tunneling $J^{(2)} = J^2/\Delta$. The second term in Eq. (9.5) considers a detuning from the exact resonance and is a necessary ingredient given that the resonant interaction strength is slightly shifted by the third term [117]. The resonance condition at leading order in perturbation theory thus reads

$$U = 2\Delta - 8J^2/(3\Delta). \tag{9.6}$$

For large tilt Δ this correction is small such that we will write $|U| \simeq 2\Delta$ in the following. The other contributions to the effective Hamiltonian are defined as

$$\begin{aligned}
\hat{H}_0 &= \Delta \sum_{i,\sigma} i\hat{n}_{i,\sigma} + 2\Delta \sum_{i} \hat{n}_{i,\uparrow}\hat{n}_{i,\downarrow} = \Delta \cdot \hat{P} + U \cdot \hat{N}_D, \\
\hat{T}_{XY} &= \sum_{i,\sigma} (\hat{c}^\dagger_{i,\bar{\sigma}}\hat{c}_{i+1,\bar{\sigma}}\hat{c}^\dagger_{i+1,\sigma}\hat{c}_{i,\sigma} + \text{h.c.}), \\
\hat{T}_1 &= \sum_{i,\sigma} \Big((1-\hat{n}_{i+2,\bar{\sigma}})(1-2\hat{n}_{i+1,\bar{\sigma}})\hat{n}_{i,\bar{\sigma}}\hat{c}^\dagger_{i,\sigma}\hat{c}_{i+2,\sigma} + \text{h.c.} \Big), \\
\hat{T}_2 &= \sum_{i,\sigma} \Big((1-\hat{n}_{i+2,\bar{\sigma}})\hat{n}_{i,\sigma}\hat{c}^\dagger_{i,\bar{\sigma}}\hat{c}_{i+1,\bar{\sigma}}\hat{c}^\dagger_{i+1,\sigma}\hat{c}_{i+2,\sigma} + \text{h.c.} \Big), \\
\hat{T}_3^D &= \sum_{i,\sigma} \Big((\hat{n}_{i,\sigma}-\hat{n}_{i+2,\bar{\sigma}})^2(1-2(\hat{n}_{i+2,\bar{\sigma}}-\hat{n}_{i,\sigma}))\hat{c}_{i,\bar{\sigma}}\hat{c}^\dagger_{i+1,\bar{\sigma}}\hat{c}^\dagger_{i+1,\sigma}\hat{c}_{i+2,\sigma} + \text{h.c.} \Big), \\
\hat{H}_D &= -\frac{4J^2}{3\Delta}\left(2\sum_i \hat{n}_{i,\uparrow}\hat{n}_{i,\downarrow}(\hat{n}_{i+1}+\hat{n}_{i-1}) + \sum_{i,\sigma}\hat{n}_{i,\sigma}\hat{n}_{i+1,\bar{\sigma}} \right).
\end{aligned} \tag{9.7}$$

Since $[\hat{H}^{\text{res}}_{\text{eff}}, \hat{H}_0] = 0$, the effective Hamiltonian conserves the linear combination of dipole moment P and doublon number N_D such that the occurrence of fragmentation can be understood from this conservation law. In [117] it was shown numerically that the Hamiltonian is indeed strongly fragmented. Like in the regime $|U| \ll \Delta$ the effective Hamiltonian contains a squeezing term $\hat{T}_3^D$, in this case the process respects the globally conserved quantity $\hat{H}_0$. Moreover, the term $(U - 2\Delta)\sum_i \hat{n}_{i,\uparrow}\hat{n}_{i,\downarrow}$ considers the resonance condition for renormalized interactions given in Eq. (9.6) since U is not exactly twice the tilt. This detuning would normally appear in every second-order process, but it can be shown [234] that as long as $|U - 2\Delta| < J$, these corrections can safely be neglected at leading order in perturbation theory and a global detuning as given in Eq. (9.5) is sufficient.

9.2. Experimental techniques

At this point we outline experimental methods relevant for this project that have not been mentioned so far, but whose ingredients are presented in part II. This concerns the preparation and characterization of initial states in the optical lattice as this knowledge is an important building block of this project.

9.2.1. General sequence and preparation of initial states

Our experimental sequence has many parallels with the experiments performed in [117, 126] as far as the initial state preparation and overall lattice sequence are concerned. First, the atoms are loaded into a deep three-dimensional lattice - the process is discussed in more detail below - and held for a duration of 30 ms to destroy residual coherences and obtain a product state. While all dynamics are frozen in the deep lattice, the gradient field is ramped to the desired value and at the same time the Feshbach field has to adjust in order to compensate the homogeneous part of the gradient field and set the correct interaction strength. After this wait time the dynamics are initiated by quenching the primary lattice to $12E_r$ and switching off the long lattice, both within 10 µs. The employed primary lattice depth in this project is deeper than in previous works at this experiment so as to achieve larger tilts Δ/J. Since the attainable slope Δ is limited by the coil design, we have to use a lower tunneling element J in order to satisfy the large-tilt limit. At the end of time evolution the primary and long lattice are ramped to their respective values before the evolution. The gradient is switched off and the vertical magnetic field is set to the non-interacting point of the Feshbach resonance in order to have no interactions during the final state readout. All this is performed while the final atom distribution in the lattice is frozen for another 30 ms.

A characteristic signature of Hilbert space fragmentation, that we want to demonstrate experimentally in this project, is the initial-state dependence of the dynamics in the tilted Fermi-Hubbard model. Therefore, we have to be able to prepare states that live within different fragments and symmetry sectors of the Hilbert space. In general, the type of state we can reliably produce is an incoherent mixture of product states with zero magnetization. It can be described by the density matrix $\hat{\rho} = N^{-1} \sum_\sigma |\psi_0(\sigma)\rangle \langle\psi_0(\sigma)|$ with the sum running over all spin permutations with vanishing magnetization. The product state $|\psi_0(\sigma)\rangle$ can be represented in the number basis as $|\psi_0(\sigma)\rangle = \prod_{i\,\text{even}} \left(\hat{c}^\dagger_{i,\uparrow}\right)^{\hat{n}_{i,\uparrow}} \left(\hat{c}^\dagger_{i,\downarrow}\right)^{\hat{n}_{i,\downarrow}}$. In our experiment we do not have access to the local chemical potential such that it is not feasible to control local charge or spin distributions. That would be the ideal scenario so as to prepare initial states corresponding to the same global conserved quantities and to probe dynamics of distinct fragments within the same symmetry sector. However, one parameter that we can control reliably with good reproducibility is the doublon fraction n_D, so we prepare initial product state families with different values of n_D. Although this changes the average filling fraction, we are still able to identify state-dependent dynamics (see sec. 9.3.1).

In our case we define the doublon fraction as the number of atoms bound on doubly occupied sites N_D divided by the total atom number N: $n_D = N_D/N$. The resulting density distribution in an interacting Fermi-Hubbard model was studied previously [235, 236] and we use those results to optimize the loading procedure into the lowest band of our three-dimensional lattice. The final scenario is basically characterized by a single dimensionless parameter, the compression, that compares the relevant energy scales, tunneling, interaction and harmonic confinement. For small compression the tunneling dominates over the trapping potential such that one obtains a metallic state with delocalized atoms to minimize the kinetic energy. Upon increasing the compression the filling in the center gets increased and one can realize a Mott insulator or even a band insulator. Our main parameter to affect this important quantity is the strength of the external harmonic confinement and we provide a detailed analysis of the loading characteristics in the following section. The finite temperature of the atoms in the lattice thereby limits the density in the trap center as well as the achievable doublon fraction.

9.2.2. Initial state characterization

In this project we developed a technique to image the singlon and doublon distribution in the lattice in separate images. This scheme is illustrated in full detail in sec. 5.3 and the results of this analysis are presented here. As mentioned above, the vertical confinement during the loading process and the scattering length a are the parameters we can tune to control the final density distribution in the optical lattice. Therefore, we characterize the cloud sizes and doublon fractions to optimize the respective initial state for the experiment. The harmonic confinement is quantified in terms of the trap frequency $\omega_h = \sqrt{\alpha\hbar/(md^2\pi)}$ with the lattice spacing $d = 266\,\mathrm{nm}$ and atomic mass m. α denotes the local curvature introduced in sec. 8.3. The trap frequency is determined from an independent measurement in the dipole trap configuration where we measured the trap frequency directly from real-space oscillations performed by the cloud. At the non-interacting point of the Feshbach resonance we perform in-situ measurements of the singlon and doublon cloud size as a function of the trap frequency ω_h as shown in Fig. 9.2a. Upon increasing the confinement the total cloud size declines and so do the singlon σ_S and doublon radius σ_D presented in the inset. A smaller cloud size results in a higher charge density in the center and a reduced hole density, important ingredients to observe the aspired dynamics. However, a disadvantage of strong confinement during loading is shown in Fig. 9.2b. The doublon fraction for fixed loading scattering length of $-20a_0$ decreases for strong confinement owing to a reduced lifetime [195]. We therefore fix the trap frequency to about $\omega_h \approx 2\pi \times 60\,\mathrm{Hz}$ during the lattice loading process which is a good compromise between initial doublon fraction and cloud size.

At this fixed harmonic confinement the doublon fraction is controlled via the scattering length during the loading process. The resulting doublon fraction in the initial state as a function of the scattering length is plotted in Fig. 9.2c. We operate in the range between

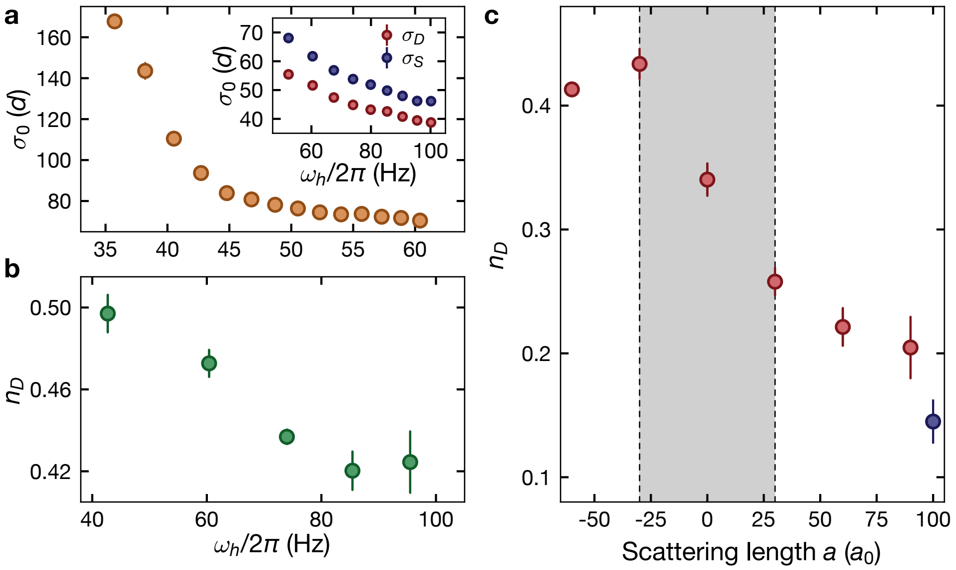

Figure 9.2.: Investigation of lattice loading parameters: a Measured in-situ cloud size in multiples of the lattice spacing d as a function of the harmonic confinement. The inset shows the singlon and doublon cloud size for even larger trap frequency than in the main panel. **b** Initial doublon fraction with loading scattering length $-20a_0$ versus the harmonic confinement. In the experiment we operate around $\omega_h \approx 2\pi \times 60\,\text{Hz}$. **c** For initial states with doublons we vary the scattering length between $-30a_0$ and $30a_0$ as indicated by the gray shaded region. The blue data point was taken with a different compression to suppress the doublon formation further. All data points are averaged thrice and error bars represent the standard error of the mean.

$-30a_0$ and $30a_0$ such that we typically have between 25 % to 45 % initial doublon fraction. Even more attractive interactions were not found to yield a larger doublon fraction, perhaps because of a reduced lifetime in the lattice [195]. Moreover, large attractive interactions prefer a more uniform density distribution and larger cloud size accompanied by an increased hole fraction [126], while we rather thrive for a small number of defects and larger doublon density near the center. In order to prepare pure singlon states, we load strongly repulsively ($100a_0$) and further weaken the confinement set by the dipole traps. Although this leads to a lower average density and a larger cloud size, it does not represent an issue for the singlon states. Residual doublons on the order of 15 % are removed from the lattice with a blast pulse before time evolution.

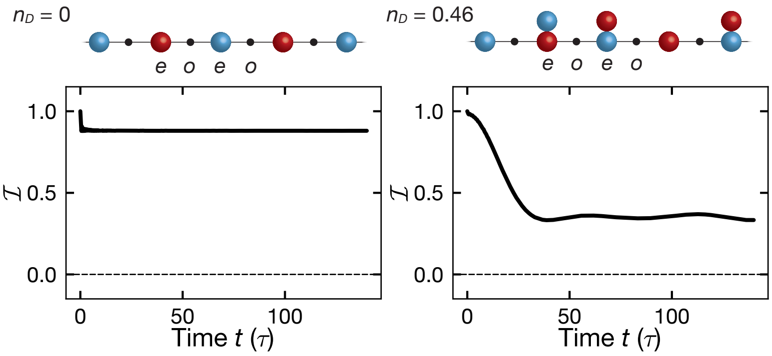

Figure 9.3.: Schematic illustration of initial state dependence: State-dependent imbalance dynamics $\mathcal{I}(t)$ for different doublon fractions n_D. The solid lines are the cumulative average of TEBD simulations with $U = 2.7J$ and $\Delta = 8J$ on $L = 101$ lattice sites according to the Hamiltonian in Eq. (9.1). Dashed horizontal lines indicate the imbalance value of a thermal ensemble at infinite temperature within the full symmetry sector of the given initial state.

9.3. Realization of fragmented models in tilted Fermi-Hubbard chains

The following section presents the experimental and numerical results of the project on Hilbert space fragmentation published in [234]. The central experimental goal are the demonstration of state-dependent dynamics in the strongly tilted Fermi-Hubbard model as sketched in Fig. 9.3 and the description via a fragmented effective Hamiltonian. To show this we explore two regimes of the tilted Hubbard model, as introduced in sec. 9.1, that are known to exhibit fragmentation in the limit of large tilt $\Delta/J \to \infty$:

- $\Delta \gg |U|, J$ ("Dipole-conserving regime")
- $|U| \simeq 2\Delta \gg J$ ("Resonant regime")

Here we can expand the Fermi Hubbard Hamiltonian (Eq. 9.1) to obtain a leading-order effective Hamiltonian (see sec. 9.1) to identify the correlated hopping processes (see Fig 9.1) and further define the dynamical fragments within their respective symmetry sector. By preparing various initial states that live within different fragments and recording the respective imbalance time evolution we show the characteristic initial-state dependence typical for systems with weak ergodicity breaking. The obtained traces are compared to the predictions from the respective effective Hamiltonian and good agreement provides evidence that we realize a fragmented model in our experiment. With complementary numerical observables we try to investigate whether individual fragments thermalize within accessible timescales.

9.3.1. The dipole-conserving regime

Models with intrinsic dipole conservation have been studied previously for spin chains [87], random unitary circuits [81, 88] and spinless Hubbard systems [89, 90] and they all exhibit ergodicty breaking features caused by Hilbert space fragmentation. The tilted Fermi-Hubbard model was shown to exhibit dipole conservation in the regime $\Delta \gg U, J$ as explained in sec. 9.1. For our CDW wave initial state with every even site occupied by a singlon or a doublon the effective Hamiltonian in Eq. (9.2) predicts two correlated tunneling processes according to $\hat{T}_3$ as shown in Fig. 9.1a, while $\hat{T}_{XY}$ does not play an important role for a CDW state. Due to the diagonal energy penalty $\tilde{U}$ the first process for an initial singlon CDW is suppressed due to energy conservation ($J^{(3)}/U = (J/\Delta)^2 \ll 1$). Contrarily, if a singlon and a doublon are adjacent to an empty site, the illustrated process is resonant and happens on a timescale set by the effective hopping rate. Based on these considerations the doublon density is expected to have a strong effect on the dynamics described by the effective Hamiltonian $\hat{H}_{\text{eff}}^{\text{dip}}$. In order to demonstrate the effective processes in the experimental data, we measure density-resolved imbalance time traces of singlons $\mathcal{I}_S$, doublons $\mathcal{I}_D$ and all atoms $\mathcal{I}$ (charge imbalance) with the method explained in sec. 5.2.

Imbalance traces and initial state dependence

To realize the dipole-conserving regime experimentally, we set $\Delta/J = 8.0(2)$, $U/J = 2.7(2)$ and the minimal tilt difference (see sec. 4.4.3) $\delta\Delta = (\Delta_\downarrow - \Delta_\uparrow)/\Delta_\downarrow = 0.6(2)\,\%$ as this is a parameter regime where we observe significant signatures and at the same time satisfy the conditions for the dipole-conserving regime sufficiently well. Comparing the charge imbalance time traces in Fig. 9.4b we observe qualitatively similar behavior for pure singlon states ($n_D = 0$) and mixed initial states with $n_D = 0.28(2)$. After a fast drop from the starting point at short times the imbalance develops a steady-state value at evolution times $t \geq 30\tau$, in agreement with previous observations for weaker tilt [117]. Note that in these traces we do not observe Bloch oscillations as they would be expected in a linearly tilted lattice because they can only be observed on shorter timescales $\lesssim 15\tau$ before they dephase due to harmonic confinement and decoherence [117]. However, for the initial state with doublons the steady-state imbalance is significantly reduced as compared to the singlon CDW. This dependence is more strikingly illustrated by the density-resolved time traces in Fig. 9.4a. While the singlon imbalance $\mathcal{I}_S(t)$ remains around 0.75 and thus only marginally below the value of the singlon state, the doublon imbalance $\mathcal{I}_D(t)$ shows a drastic decrease to an average value around 0.4. This observation can be readily explained by the action of $\hat{T}_3$, which leads to a rearrangement of doublons between even and odd lattice sites, while the singlons remain unaffected (see Fig. 9.1a). These processes happen

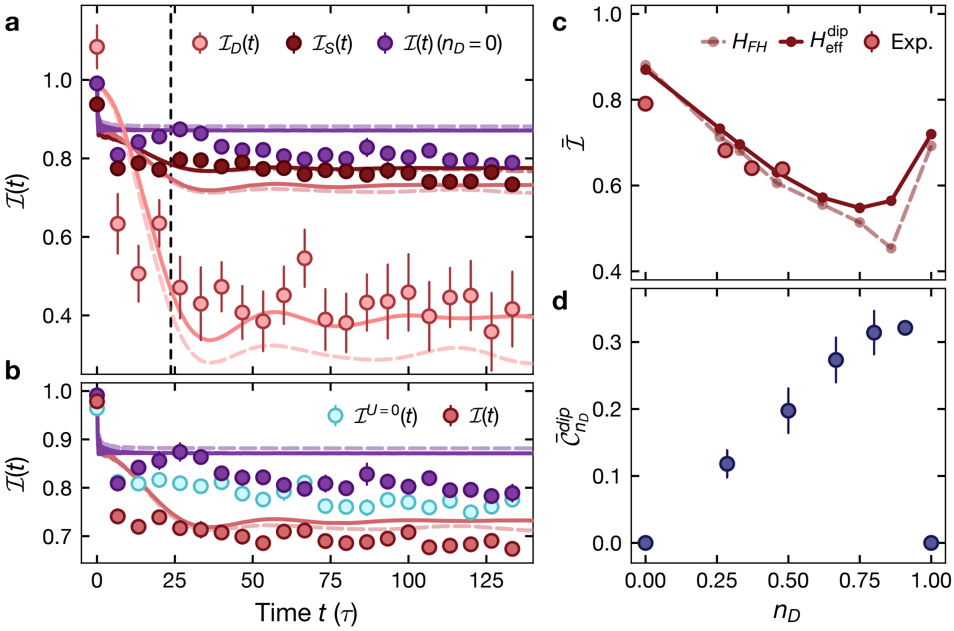

Figure 9.4.: Dipole-conserving regime: a Imbalance time traces for different initial states: Singlon CDW, doublon $\mathcal{I}_D$ and singlon imbalance $\mathcal{I}_S$ of a mixed initial state with $n_D = 0.28(2)$. Solid lines are the result of TEBD simulations on $L = 101$ lattice sites for the effective and dashed, transparent lines for the exact model. The dashed vertical line shows the effective timescale $1/(2\pi J^{(3)})$. **b** Charge imbalance $\mathcal{I}$ for the data from panel a together with the non-interacting case and the singlon CDW initial state. Experimental data points are averaged ten times and error bars denote the standard error of the mean. **c** Steady-state charge imbalance as a function of the doublon fraction. Experimental data and TEBD simulations of the exact and effective Hamiltonian are averaged in the time window between 120 and 140τ. **d** Average fragment dimension according to Eq. (9.8) as a function of the doublon fraction in the initial state. The average is computed over all possible charge configurations in a system with $L = 13$ lattice sites.

on a timescale $1/(2\pi J^{(3)}) \simeq 24\tau$ in agreement with our observations. Moreover, we confirm that this initial-state dependence is indeed a many-body phenomenon by taking a time trace for the mixed initial state with $U = 0$. Within our experimental uncertainty it attains the steady-state value of the pure singlon CDW even in the presence of doublons, here $n_D = 0.28(2)$ (see Fig. 9.4b). Hence, we can experimentally prove the expectation that dipole-conserving processes require interactions. This observation is further underlined by the fact that the effective Hamiltonian $\hat{H}_{\mathrm{eff}}^{\mathrm{dip}}$ in Eq. (9.2) vanishes trivially for $U = 0$.

We reproduce our experimental traces from Fig. 9.4a using time-evolving block decimation (TEBD) [237] based on matrix product states (MPS) for the exact (Eq. 9.1) and effective Hamiltonian (Eq. 9.2) in a lattice with $L = 101$ sites. We choose this numerical technique over ED to be able to include experimental imperfections in the simulations and we can further simulate large system sizes on the required timescales. Based on previous studies with comparable initial conditions [126] we assume a hole fraction of 20 % on even sites that is caused by non-adiabatic lattice loading and thus a finite temperature as well as other experimental imperfections. Moreover, in the outer regions of the atomic cloud the density is overall lower such that holes appear with larger probability and our imbalance extraction method inevitably averages of the entire atom cloud. Holes effectively cut the atomic chain and constrain the dynamics because the effective hopping processes require certain charge configurations for resonances to occur. Hence, in order to simulate the experiment as closely as possible, we have to include holes in the numerics. Since we can only simulate 13 lattice sites for fillings ≥ 0.5 efficiently with ED, the addition of holes would reduce the particle number even further and we have to expect strong finite-size effects. The simulations typically show oscillations like Bloch oscillations and interaction-induced revivals that are absent in the experiment on intermediate timescales due to ensemble averaging and other imperfections. We therefore present the time-averaged imbalance defined as $\mathcal{I}(t) = \frac{1}{t}\int_0^t \mathcal{I}(\tau)d\tau$. We find that the numerical simulations match our experimental data very well, in particular they are captured by the perturbative description with the effective Hamiltonian. There is a small deviation between exact and effective description for $t \gtrsim 10\tau$ due to the effects of higher orders, but still the effective Hamiltonian captures the observed dynamics of our system emphasizing that they can be reproduced with the leading-order processes. This agreement between our experimental data and the simulations from a fragmented Hamiltonian are a first strong indication that we indeed probe the dynamics within a fragmented Hilbert space. We further note a weak residual imbalance decay for the singlon initial state that we attribute to technical heating due to lattice noise on the transverse laser beams. This effect is more dominant for large imbalance values such that the other initial states are less influenced. Moreover, we can attribute a small systematic offset between experiment and numerics to an inhomogeneous density distribution of the initial state.

Connection to Hilbert space fragmentation

In order to connect our observations to the phenomenon of Hilbert space fragmentation beyond the description in terms on an effective Hamiltonian, we rely on complementary numerical investigations. We study the steady-state imbalance for various initial doublon fractions and correlate it with the dimension of the fragment within the respective symmetry sector the initial state ψ lives in. In Fig. 9.4c we show the experimentally determined steady-state charge imbalance, obtained from averaging the data points in the time window between 120 and 140τ, as a function of the initial doublon fraction n_D. As anticipated, the steady-state imbalance monotonously decreases for increasing n_D. In the experiment we can prepare values up to $n_D < 0.5$, but we complement the range numerically by going up to $n_D = 1$ (half-filling). We observe that this behavior continues until the imbalance reaches a minimum around $n_D = 0.85$ before it increases again. At first glance this result is surprising as the symmetry sector is largest for half-filling and thus most likely to thermalize. However, this outcome can be explained by the effective doublon number conservation due to the diagonal energy penalty $\tilde{U}$ associated with the formation and dissociation of doublons. A pure doublon CDW would indeed be frozen like the singlon CDW considering only the leading-order processes of $\hat{H}_{\text{eff}}^{\text{dip}}$. As explained in sec. 9.1, we take this effective doublon number conservation into account by replacing $\hat{T}_3$ in the effective Hamiltonian with $\hat{T}_3'$ (Eq. 9.4) and using this expression for the computation of the dimension $d_{\mathcal{K}}$ of the dynamically relevant fragment. The various initial states we can prepare in the experiment have different fillings and hence differ in the total charge or particle number, thus living in different symmetry sectors of the Hilbert space. Further, even at the same doublon fraction, certain charge configurations do not have the same dipole moment such that a direct comparison of the fragment dimension is not meaningful as one would ideally compare different fragments $\mathcal{K}$ within the same symmetry sector $\mathcal{S}$. Instead, we compute the relative fragment dimension normalized to the dimension $d_{\mathcal{S}}$ of the respective symmetry sector the fragment is contained in and present the quantity

$$\mathcal{C}_\psi = \frac{\log(d_{\mathcal{K}})}{\log(d_{\mathcal{S}})} = \frac{\log\left[\dim\left(\mathcal{K}_{n_D,\psi}\right)\right]}{\log\left[\dim\left(\mathcal{S}_{P,n_D}\right)\right]}. \tag{9.8}$$

Assuming an exponential scaling of fragment and symmetry sector dimension with system size (up to polynomial corrections), this quantity is independent of the system size and lies in the range $\mathcal{C}_\psi \in [0,1]$. While a frozen state would have $\mathcal{C}_\psi = 0$, this quantity tends to 1 if the fragment is almost as large as the full symmetry sector defined by doublon number and dipole moment. We use ED on an ideal system (i.e. no holes) with size $L = 13$ and sample over all initial state configurations to obtain the averaged quantity $\bar{\mathcal{C}}_{n_D}^{\text{dip}}$ that is shown in Fig. 9.4c. We can identify a strong correlation between the steady-state imbalance value shown in Fig. 9.4b and the average size of the corresponding fragment. If the dynamics thermalize within the respective fragments, this is a strong indication that the observed dynamics can be explained by the fragmentation of the underlying Hilbert space. Though, we cannot infer the type of dynamics within the fragments, whether there is thermalization or non-ergodicity restricted to a certain Krylov subspace as our numerical observables do not allow a conclusion for this regime. We comment more on this issue for the second investigated regime in sec. 9.3.2. The dimensions for individual states are presented in Appendix B.2.

Interpretation of our results in terms of Stark MBL

Although this particular regime of strong tilt and weak interactions was repeatedly studied in the context of Stark MBL [89, 95, 96, 101], we cannot conclude from our experimental data whether our system really exhibits features typical for Stark MBL. On the available timescales the observed dynamics can be explained by a leading-order effective Hamiltonian and the resulting dynamical hopping processes. This does not make any statement about the long-term behavior. In our case of finite tilt the strongly fragmented effective Hamiltonian only applies on transient timescales as higher orders in the expansion make the system weakly fragmented by coupling different fragments and lead to a relaxation on exponentially long times $t \propto \exp(\Delta/J)$, according to the theory of prethermalization [180, 238]. Admittedly, Stark MBL was found in the presence of harmonic confinement that is certainly present in our system, but in order to show Stark MBL over Hilbert space fragmentation we would have to access the long-time behavior of the time traces. Our system might as well be in a prethermal regime governed by the leading order effective Hamiltonian before it finally thermalizes. It is also worth mentioning that the observed initial state dependence distinguishes this system fundamentally from regular MBL characteristics.

9.3.2. The resonant regime

In the presence of resonances between interaction energy U and tilt Δ the tilted Fermi-Hubbard model also features non-ergodic properties and a description in terms of an effective Hamiltonian can be found. At first glance this might appear counter-intuitive as resonances, even at long distance, enable transport via resonant particle exchange as observed in [239] and can restore thermalization. Such a scenario was drawn for MBL systems, for instance as a mechanism to explain the Griffiths regime near the phase transition [43]. However, in the strongly tilted Fermi-Hubbard model we have the imposition of dynamical constraints via dipole moment and doublon number conservation such that this picture does not apply. Instead, in a previous study [117] the authors identified non-ergodicity over long times, even at low and intermediate tilt, and related this outcome to emergent kinetic constraints governed by a fragmented Hamiltonian.

Time traces and initial-state dependence

The expected initial state dependence in the regime $U \simeq 2\Delta \gg J$ can be illustrated by considering the processes of $\hat{H}_{\mathrm{eff}}^{\mathrm{res}}$ sketched in Fig. 9.1b. Among the correlated tunneling processes only those related to $\hat{T}_3^D$ change the recorded charge and doublon imbalance. In addition, the process $\hat{T}_2$ leads to a change of the singlon imbalance. Both processes have in common that they require the presence of doublons. Starting from a pure singlon CDW it requires the dynamical production of doublons via $\hat{T}_1$ to enable the other processes, which impedes their efficiency and time scale. This picture illustrates the expected initial state dependence of the dynamics in this fragmented regime of the tilted Fermi-Hubbard model.

Like in the previous regime we investigate this assumption by measuring imbalance time traces for an initial singlon CDW ($n_D = 0$) and a mixed initial state with the highest achievable doublon fraction of $n_D = 0.47(4)$. These traces are plotted in Fig. 9.5a. After an initial drop in the beginning, the singlon CDW state remains at a high imbalance plateau close to $\mathcal{I}_S = 0.75$. The same characteristic was found in the regime $\Delta \gg U, J$, but here the imbalance is slightly lower. This behavior can be explained by the resonant formation of doublons according to process $\hat{T}_1$ where a single particle hops by two lattice sites to its nearest neighbor and the released potential energy gets transferred into interaction energy. Subsequently, the dynamics continue via $\hat{T}_2$ and $\hat{T}_3^D$. This chain of processes was already found to lead to a reduced imbalance for a singlon initial state at the resonance $U \simeq 2\Delta$ [117]. Conversely, when starting from an initial state with doublons we observe a fast and strong reduction of the imbalance owing to the previously explained leading-order processes. Hereby we further notice that singlon $\mathcal{I}_S$ and doublon imbalance $\mathcal{I}_D$ attain similar values, a striking difference to the previous regime where the leading-order process only affected the doublon evolution on even and odd sites. This is a consequence of the fact that the singlon imbalance is imminently affected by the effective Hamiltonian, namely by the operator $\hat{T}_2$.

Again, the data is reproduced with time-averaged TEBD simulations of the full and effective Hamiltonian, this time on $L = 51$ lattice sites and including 20 % holes on even sites. We use the interaction strength $U = 15.7J$ fulfilling the resonance condition from Eq. (9.6). We find very good qualitative agreement with the experimental data reproducing all characteristic features described previously. The systematic offset is attributed to ensemble averaging and an imperfect density distribution in the lattice. The processes that reduce the observed imbalance are strongly density-dependent and thus the distribution of doublons and the presence of holes can change the recorded traces significantly. Conversely, starting from a singlon CDW only the process $\hat{T}_1$ takes place. Hence, the agreement between theory and experiment is better in this case. Moreover, the traces from the exact and effective Hamiltonian exhibit good conformity and only start to deviate for times $t \gtrsim 30\tau$ due to higher orders in the expansion. We conclude that in the resonant regime we equally get good agreement between the data and the leading-order effective Hamiltonian. Since $\hat{H}_{\text{eff}}^{\text{res}}$ is fragmented, this is a strong indication that we indeed probe the dynamics of a fragmented model.

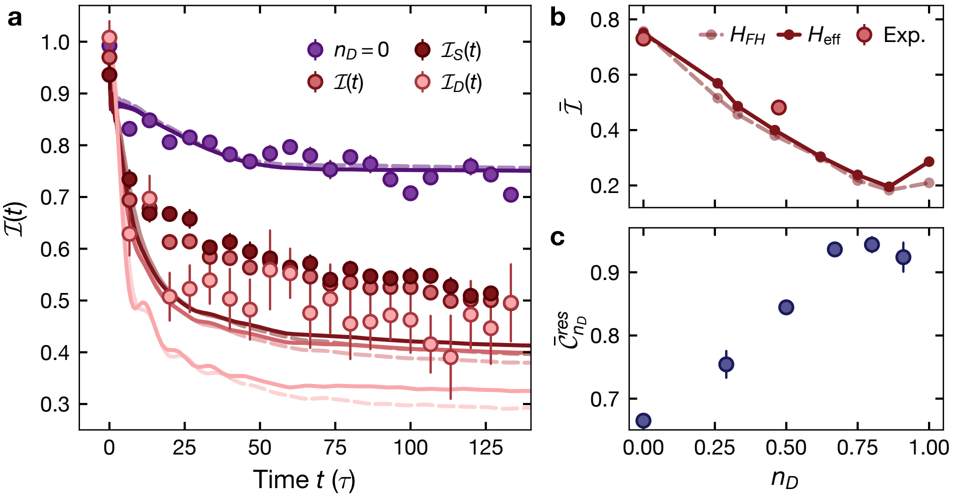

Figure 9.5.: Resonance regime $U \simeq 2\Delta$: a Imbalance time traces for a singlon initial state as well as with a doublon fraction of $n_D = 0.47(4)$. Error bars denote the standard error of the mean after ten averages. Solid lines represent TEBD simulations of the effective, dashed, transparent lines of the exact Hamiltonian performed on $L = 51$ lattice sites and averaged over ten different initial configurations. **b** Steady-state charge imbalance as a function of the initial doublon fraction n_D from experimental data points and time-averaged TEBD simulations of full and effective Hamiltonian averaged between 120 and 140τ. **c** Average fragment dimension according to Eq. (9.8) as a function of the initial doublon fraction. The dimension is averaged over all possible charge configurations in a system with $L = 13$ lattice sites.

Connection to Hilbert space fragmentation

Like in the previous regime we relate our observations deduced from the recorded imbalance time traces to the phenomenon of Hilbert space fragmentation. Fig. 9.5b displays the steady-state imbalance averaged between 120τ and 140τ, both for experimental data and numerics. Not only do we find good agreement between experiment and theory, but also between exact and effective dynamics across the full range of doublon fractions. Like in the dipole-conserving regime we correlate the steady-state imbalance with the average fragment dimension $\bar{C}^{\text{res}}_{n_D}$ in Fig. 9.5c. Note that in the case of $n_D = 1$ the fractal dimension $\bar{C}^{\text{res}}_{n_D} = 0$, hence the doublon CDW is frozen, but the simulated steady-state imbalance is around 0.3. While the computation of the fragment dimension assumes an ideal state, the TEBD simulations of exact and effective Hamiltonian contain 20 % holes. While this had no effect in the dipole-conserving regime, at resonance the doublon CDW is no longer frozen because the process $\hat{T}_1$ can take place in inverse direction. This leads to a dynamical doublon decay and subsequent dynamics according to $\hat{T}_2$ and $\hat{T}_3^D$. Like in the previous regime we conclude that this correlation can be explained by fragmentation if we assume that the dynamics are thermal within individual fragments. In the resonant regime we can investigate this assumption more closely as done in the following section.

Entanglement entropy and thermalization dynamics

We can gain further information about the system's properties by looking at the thermalization dynamics within the individual fragments. For this purpose we compute the time evolution of the half-chain entanglement entropy $S_{L/2}$ for multiple initial doublon fractions and compare it to the Page value [87, 140] of the respective fragment. That value represents a thermal ensemble at infinite temperature. Note that these simulations are carried out for a small system of 13 lattice sites with ED and for an ideal system without holes, otherwise an estimate for the Page value is intractable due to a too large Hilbert space. Moreover, we disregard atypical initial states with strong boundary effects irrelevant for larger system sizes. We compute the entanglement entropy for multiple doublon fractions up to 5000τ, average them over relevant initial state configurations and plot the resulting traces in Fig. 9.6. They all exhibit a steady increase towards a filling-dependent saturation value. The dashed horizontal lines mark the mean Page value for the respective doublon fraction and the shaded area marks the uncertainty from averaging over different initial states with the same doublon fraction. Note that this implicitly connects to the fragment dimension plotted in Fig. 9.5c. Since the thermal entanglement entropy, as an extensive thermodynamic quantity, depends on the fragment dimension, the entropy scaling with the doublon fraction can be directly explained from this result. In all cases shown it seems like the entanglement entropy finally saturates to the respective Page value after very long times, much longer than experimentally accessible timescales. Hence, within the individual fragments the system thermalizes, but as a whole the system remains non-ergodic as can be, above all, inferred from the non-zero steady-state imbalance on intermediate times. This is a typical feature of fragmented systems and underlines that Hilbert space fragmentation is likely present in our system although this evidence is purely numerical.

This outcome pinpoints a major difference between Hilbert space fragmentation and conventional MBL. As explained in sec. 2.2, MBL features a fast initial increase to the non-interacting entropy value within the first tunneling times followed by a logarithmic growth in time and a volume-law saturation value at exponentially long time that is subthermal and thus smaller than the Page value. In the regime $U \simeq 2\Delta$ on the other hand we observe an initial ballistic growth followed by an asymptotic approach to the thermal value within the respective fragment. This concept of Krylov-restricted ETH was first introduced in [90]. Note that in the dipole-conserving regime $\Delta \gg U, J$ we cannot make such a statement because the evolution of the entanglement entropy is much slower and exhibits long-lived oscillations such that we cannot reach a conclusion about

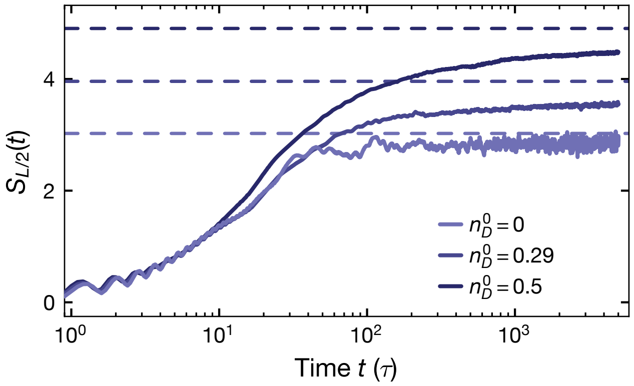

Figure 9.6.: Half-chain entanglement entropy in the resonant regime $U \simeq 2\Delta$: Time evolution of the entanglement entropy for three different initial doublon fractions. Dashed horizontal lines indicate the Page value of the respective fragment signaling a thermal ensemble at infinite temperature with an uncertainty due to averaging over all relevant initial charge configurations indicated by the shaded region. The simulations were performed with ED for an ideal system on 13 lattice sites.

its convergence on available timescales. Moreover, thermalization within the individual fragments is not established in this regime. Instead, the authors in [90] even identified integrable sectors that obviously violate this assumption and could potentially explain the slower evolution of entanglement.

9.3.3. Effect of a tilt difference

The effective Hamiltonian in the dipole-conserving regime (Eq. 9.2) is, like the Fermi-Hubbard model, SU(2)-invariant. The effect of SU(2)-symmetry breaking can be studied when the tilts seen by both spins are not equal. In the presence of such a tilt difference the central process predicted by $\hat{H}_{\text{eff}}^{\text{dip}}$ becomes off-resonant with an energy mismatch $\delta = |\Delta_\downarrow - \Delta_\uparrow| > 0$. This adds additional constraints to the system and thus the dynamics become strongly suppressed if $J^{(3)} < \delta < J$. We study this effect experimentally for the dipole-conserving regime and for a mixed initial state with doublon fraction $n_D = 0.47(4)$ by measuring the singlon and doublon imbalance after a fixed evolution time between 67τ and 80τ in the presence of a certain tilt difference $\delta\Delta = (\Delta_\downarrow - \Delta_\uparrow)/\Delta_\downarrow$. As characterized in Fig. 4.3, we can tune the tilt difference freely in the range $\delta\Delta \in [0.006, 0.11]$ via the power of the RF dressing field. The obtained results are plotted in Fig. 9.7. For the smallest possible tilt difference we recover the results from Fig. 9.4a, while the steady-state doublon imbalance increases monotonously for larger $\delta\Delta$. At the same time the singlon imbalance shows no significant dependence on the tilt difference, again for the reason that $\hat{T}_3$ leaves the singlon imbalance unchanged. We reproduce the experimental results with TEBD

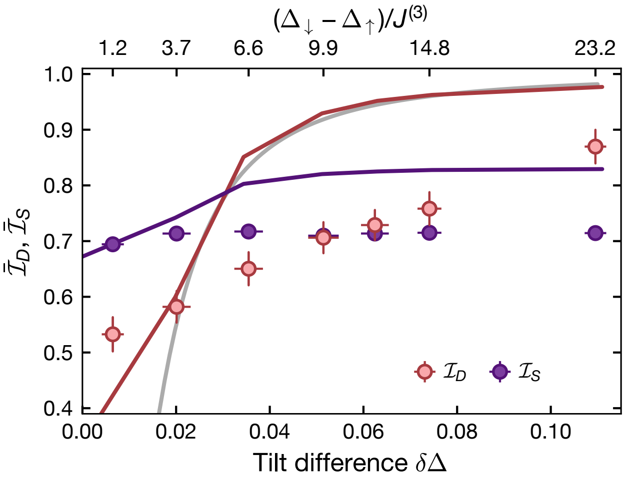

Figure 9.7.: Tilt difference in the dipole-conserving regime: Singlon and doublon steady-state imbalance as a function of the tilt difference $\delta\Delta$ averaged in the time window between 67τ and 80τ for an initial state with $n_D = 0.47(4)$. Solid lines are the result of TEBD simulations with the exact Hamiltonian on 51 lattice sites and the gray line denotes the imbalance of a Wannier-Stark localized dipole as explained in the text. The upper horizontal axis quantifies the relative tilt difference in units of the effective tunneling. Experimental data points are averaged 40 times and error bars are the standard error of the mean.

simulations of the exact Hamiltonian and the spin-dependent tilt implemented. While the overall trend is observed in the experiment is reproduced by the simulations, we notice a systematic deviation for large values of $\delta\Delta$. We attribute this to technical heating from the orthogonal lattice beams, which particularly affects large imbalance values. The same effect was observed for the singlon CDW in the dipole-conserving regime (see Fig. 9.4a).

In order to get a quantitative understanding of the physical impact of this tilt difference, we can modify the effective Hamiltonian to include the spin-dependent tilt. As long as δ is small compared to the hopping rate ($\delta \ll J$), the perturbative expansion can still be applied and we obtain an effective Hamiltonian

$$\hat{H}^{\delta}_{\text{eff}} = \hat{H}^{\text{dip}}_{\text{eff}} + \Delta_\uparrow \sum_i i\hat{n}_i + \delta \sum_i i\hat{n}_{i,\downarrow}. \tag{9.9}$$

The effect of this additional term in δ can be intuitively understood by considering a family of states $\{|n\rangle\} = \{|\ldots \uparrow\uparrow\updownarrow 0 \uparrow\uparrow \ldots\rangle\}$ with a doublon ($\updownarrow$) initiated on site n with a neighboring hole and surrounded by a spin-polarized background. This family defines a subspace that is closed under the action of the effective Hamiltonian. The term $\hat{T}_{XY}$ has a trivial interaction and diagonal contributions except of the term in δ become proportional to the identity matrix. Thus, when projected onto this subspace, Eq. (9.9) simplifies to the expression

$$\hat{H}^{\delta}_{\text{eff}} = -J^{(3)} \sum_{n} |n\rangle \langle n+1| + \text{h.c.} + \delta \sum_{n} n\, |n\rangle \langle n| \,. \tag{9.10}$$

This precisely defines a single-particle Hamiltonian of a doublon-hole pair that propagates with tunneling $J^{(3)}$ in a tilted external potential with slope δ. In the spin-1 framework used in [87] this corresponds to a dipole $|+-\rangle$ propagating in a background of polarized spins. The resulting dynamics are well-known, the doublon undergoes Bloch oscillations and acquires a steady-state imbalance of

$$\bar{\mathcal{I}}_D = \mathcal{J}_0^2 \left(\frac{4J^2 U}{\Delta_{\downarrow}^3 \cdot \delta\Delta} \right) = \mathcal{J}_0^2 \left(\frac{4J^{(3)}}{\delta} \right) \tag{9.11}$$

as explained in sec. 8.1. This analytical prediction is shown in Fig. 9.7 and matches the numerical result from the TEBD simulations of the exact Hamiltonian (Eq. 9.1) very well. Only in the limit of small $\delta\Delta$ this simplified description fails because the picture of a bound doublon-hole pair is no longer appropriate. Note that in our experiment the condition $\delta < J$ is fulfilled for the full range of tilt differences as $J/J^{(3)} \simeq 26$. For very large differences $\delta > J$ it can be shown that the dipole moment is independently conserved for each spin such that the effective Hamiltonian only contains diagonal contributions and the dynamics are frozen for any initial state [234, 240].

9.3.4. Interaction scan

Finally, we investigate the characteristics of the tilted Fermi-Hubbard model for large $\Delta \gg J$ as a function of the interaction strength U beyond the strictly defined regimes studied above. We measure the steady-state imbalance averaged in the time window from 67τ to 80τ for a pure singlon initial state as well as for a mixture with doublon fraction $n_D = 0.47(4)$. We present the recorded singlon and doublon imbalance in Fig. 9.8 and also highlight the relevant regimes studied above. In the dipole-conserving regime (blue-shaded area) we recover the main characteristic that the singlon imbalance is mostly unaffected while the doublons show a strong signal, an outcome that could directly be explained by the processes of the effective Hamiltonian. In the fragmented regime at the resonance $U \simeq 2\Delta$ (yellow region) we see a distinct decline in both the singlon and doublon imbalance. Within our experimental uncertainty the initial singlon CDW shows no dependence on the interaction strength across the full investigated range. At first glance, this seems to be in contradiction to the results from [117], where distinct dips in the imbalance were identified near the resonance $U \simeq 2\Delta$ and that were related to the dynamical formation of doublons and subsequent dynamics as predicted by the effective Hamiltonian (Eq. 9.5) and its leading-order processes (Fig. 9.1b). Though, this

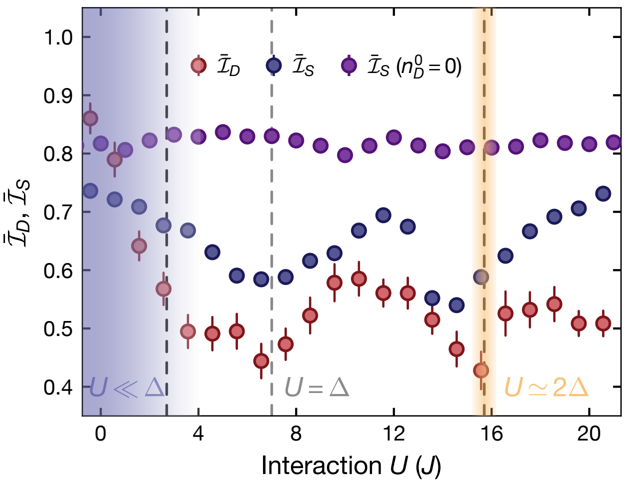

Figure 9.8.: Interaction dependence of the tilted Fermi-Hubbard model: Steady-state singlon and doublon imbalance extracted in the time window between 67τ and 80τ as a function of the interaction strength. The purple points represent the singlon CDW initial state that does not show dynamics on this timescale. The mixed state has an initial doublon fraction of $n_D = 0.47(4)$. Colored regions highlight the investigated regimes in this project that exhibit Hilbert space fragmentation with the dashed vertical lines marking the concrete experimental interaction strength. The data points are are averaged eight times for five points in time and error bars denote the standard error of the mean.

was observed at lower tilt ($\Delta = 3.3J$) and longer observation times up to 700τ such that we do not expect a significant signal at our shorter observation times.

Also indicated in the figure is the resonant regime $U = \Delta$ that is known to exhibit fragmentation and represents a constrained version of the Quantum East Model [177] that respects particle number conservation. According to [79] this regime further features quantum many-body scars, highlighting the rich dynamics of the tilted Fermi-Hubbard model. Similar to the other regimes, one can derive an effective Hamiltonian, in this case at first order in perturbation theory, and compute the structure of the fragmented Hilbert space. Moreover, this regime provides product states giving rise to scarred dynamics [79] and thus enabling an investigation of the interplay between quantum scars and Hilbert space fragmentation. We leave this study for future work. In the limit of strong interactions and away from possible resonances ($|U| \gg J, \Delta$; $|U| \neq n\Delta$; $n \in \mathbb{N}$) the number of doublons is effectively conserved and moreover, the model maps to a first-order effective Hamiltonian of spinless fermions in the presence of a tilt. We cannot enter this regime in the experiment because we are technically limited to the interaction range plotted in Fig. 9.8.

9.3.5. Discussion of experimental imperfections

Up to this point the discussion of the experimental results applies to an ideal system, with the exception that we included holes in the numerical simulations. However, a realistic experimental setup exhibits imperfection that may necessitate a closer inspection of the data. In our experiment we identify three main deviations from the ideal setting and explore the impact on the final data by means of simulations with the approximate method developed in [241].

Limited doublon lifetime

Individual atoms in an optical lattice have a finite lifetime due to off-resonant photon scattering and subsequent heating. Typical scattering rates of photons from the lattice and dipole trap lasers are in the range of few Hz such that atom number lifetimes are on the order of hundreds of milliseconds up to few seconds. In an independent measurement we determined the singlon lifetime in the optical lattice, mainly limited by this effect, to be $2.6(2) \times 10^3 \tau$, so it plays a negligible role on the experimentally relevant timescale. Conversely, the primary loss mechanism for doublons are light-assisted collisions. This term describes the pair-wise loss of atoms located on the same lattice site caused by strong dipole-dipole interactions between a ground-state and an excited-state atom that previously absorbed an off-resonant photon [126, 195]. For our blue-detuned lattices these interactions are repulsive such that the atoms move away from each other and pick up a part of the detuning as kinetic energy. This energy absorption is sufficient for both atoms to escape the trap.

We aim to measure the doublon lifetime independent of any ongoing dynamics in the lattice so as to distinguish the induced losses from dynamical doublon dissociation and formation. We remove the tilt as well as the magnetic field ramps at the beginning and the end of the time evolution. The atoms are kept at constant, strongly repulsive interaction ($U = 20J$) such that doublons cannot decay dynamically into singlons. This decay is prohibited energetically because in the tight-binding limit, the dissociation of a doublon releases the interaction energy U and converts it into kinetic energy. The width of the ground band is $4J$ such that two atoms can only absorb an energy of $8J$ at most. Keeping the doublon at strong interactions $U = 20J$ thus suppresses this decay channel and the only decay we measure in the experiment is caused by light-assisted collisions. Via iterative measurements of the atom number with and without the doublons removed by our near-resonant blast pulse we can monitor the singlon and doublon number as a function of the hold time in the lattice as shown in the inset of Fig. 9.9a. While the singlon number is constant, important evidence that there is no dynamical doublon loss, the total

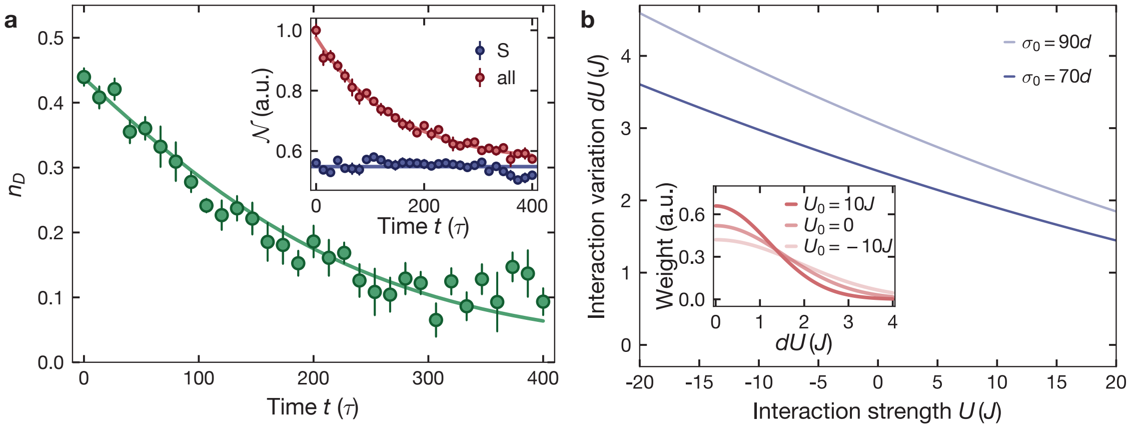

Figure 9.9.: Quantitative analysis of experimental imperfections: a Dependence of the doublon fraction in a deep lattice as a function of the hold time in a deep primary lattice with $18E_{rs}$ and strongly repulsive interactions ($U = 20J$). The solid line represents the expectation from the text without free parameters. The inset shows the singlon and doublon numbers that are used to compute the doublon fraction plotted in the main panel. Solid lines are fits to the data points (averaged four times and error bars showing the standard error of the mean), an exponential decay to the doublons and a constant value to the singlons. **b** Variation of the interaction strength along a 1D tube between the center and edge of the cloud due to the magnetic field gradient at a fixed tilt of $\Delta = 9J$ for different initial states, corresponding to the singlon CDW and a mixed states with maximal doublon fraction $n_D = 0.47(4)$. While the main panel gives an upper bound for the interaction shift, the inset shows the relative weight of dU based on the Gaussian density distribution of the atomic cloud for a mixed initial state ($\sigma_0 = 70$ sites).

atom number decays exponentially. The fit describes the data very well and yields a doublon lifetime of $109(8)$ ms $= 145(11)\tau$. The dynamical doublon fraction is then given by as $n_D = 1 - \bar{N}_S / N(t)$ with the constant singlon number $\bar{N}_S$ and presented in the main panel of Fig. 9.9a. This outcome explains that the available observation time is limited by this doublon loss and we therefore do not exceed evolution times of about 133τ.

Interaction averaging

As explained in sec. 8.2, the magnetic field gradient induces a spatially dependent interaction strength along the 1D tubes of the optical lattice and depends on the extent of the atomic density distribution. The cloud size determined from in-situ images, is defined as the 4σ-width of the Gaussian profile and depends on the initial state. In case of a pure singlon CDW we obtain about 360 sites while the cloud is smaller with 290 sites for the initial state with maximal doublon fraction. Using the expression of the interaction strength in Eq. (4.3) and the parametrization of the Feshbach resonance in Eq. (4.4) we can compute the range of interaction strengths as a function of the set value for both cloud sizes [133]. The result is plotted in Fig. 9.9b and shows the interaction difference dU between the cloud center and wings for a $12E_r$ deep primary lattice. These values are only an upper bound for the amplitude of the averaging effect. The inset shows the weights of interaction variation taking the Gaussian density distribution of a mixed initial state with $n_D = 0.47(4)$ into account. These weights are plotted for three different center interactions U_0 and underline that the effect is weaker for strongly repulsive interactions. The most striking impact of his averaging effect is that it causes a finite interaction even in the case $U = 0$.

Time-dependent interaction strength

The finite lifetime of double occupancies in the optical lattice imposes constraints on the design of the experimental sequence. Our main limitation is the ramp time of the power supply responsible for the generation of the Feshbach field. In a previous experiment [117] on the same apparatus we conceded wait times as long as 140 ms for the magnetic field to settle between lattice loading the beginning of the time evolution. This duration was found to be sufficient to reach the target value of the magnetic field and thus the correct interaction strength to an accuracy better than our detection limit. In that case, however, we were only working with singlons in the initial states and the associated lifetime is much longer such that the long wait time did not represent an obstacle. In this experiment, however, we prepare states with doublons that are subject to light-induced losses. Within a wait time of 140 ms we would already lose about 73 % of the initial doublon fraction making the experiment practically impossible. Instead, we have to use shorter wait times before and after the time evolution in order to keep as many doublons as possible. The obvious disadvantage of this method is that the magnetic field will not have settled at the beginning of the time evolution and we induce a time-dependent interaction strength.

We can employ the technique of RF spectroscopy to directly measure the induced shift in the magnetic field and thus the interaction shift during time evolution in the optical lattice. Starting from a spin-polarized sample in the $|{\downarrow}\rangle$-state we send and RF π-pulse resonant with the transition $|{\downarrow}\rangle \rightarrow |{\uparrow}\rangle$ for different evolution times t after a wait time of 30 ms like in the experimental sequence. For every time t we record the excitation spectrum of the pulse and extract the center frequency from a Gaussian fit. Note that the analytical spectrum of a π-pulse is $P(\omega) \propto \mathrm{sinc}^2\left((\omega-\omega_0)T_\pi/2\right)$ with the center frequency ω_0. However, due to the space-dependent magnetic field the transition frequency is not the same throughout the atomic cloud. The spectrum is thus inhomogeneously broadened (in analogy to Doppler broadening in laser spectroscopy) and the Gaussian approximation applies fairly well. The recorded resonances are depicted in Fig. 9.10a for the shortest and longest wait time. From the extracted transition frequencies we obtain the respective

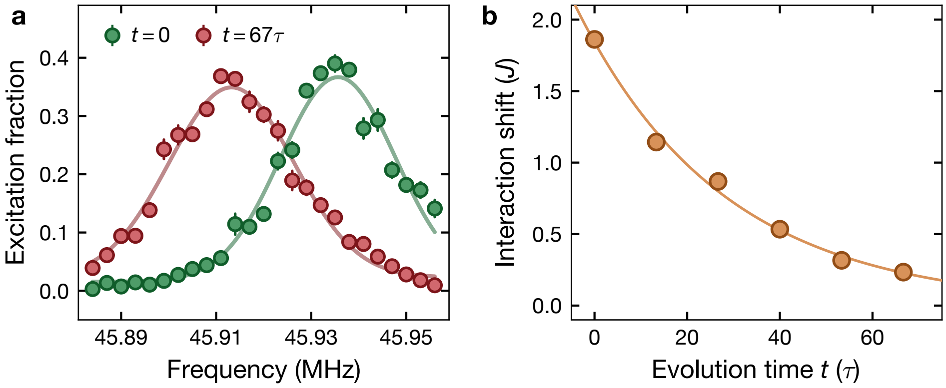

Figure 9.10.: Time dependence of the interaction strength U: a Excitation spectra of RF π pulses after two different evolution times t. Solid lines are Gaussian fits to the data points and error bars denote the standard error of the mean from four averages. **b** Interaction shift $U(t) - U_0$ with the set interaction strength $U = 0$ as a function of the evolution time obtained from the fitted center frequencies in panel a. The solid line is an exponential fit to the data points returning a time constant of $32(6)\tau$.

magnetic field by solving the Breit-Rabi equation numerically. The resulting interaction strength then follows from the equation for the Feshbach resonance (Eq. 4.4) and the results are shown in Fig. 9.10b. The interaction shift is well captured by an exponential decay with a time constant of $24(4)$ ms $\simeq 32(6)\tau$ and an initial offset of $1.8(1)J$. Therefore, the short-time dynamics are mostly affected by the shift while our statements about long-time dynamics and steady-state properties are rather unaffected. In case of a singlon initial state the preceding discussion does not apply because we adapt the wait time to the previously established duration of 140 ms.

Quantitative analysis with the approximate method

The preceding experimental imperfections are not included in the TEBD and ED simulations, but it is important to understand their quantitative impact on the recorded imbalance. We tackle this problem by means of the approximate method recently developed in our group [241]. This method is particularly efficient for strongly localized systems and thus eligible for this project. In short, this numerical algorithm considers a lattice with $2\ell + 1$ sites around a $|\downarrow\rangle$-atom at the center. We take $k_\downarrow$ additional $|\downarrow\rangle$-atoms, $k_\uparrow$ $|\uparrow\rangle$-atoms and k_d doublons with the restriction $k_\uparrow, k_\downarrow, k_d < \ell$. These approximations are justified for localized systems where the dynamics of a given atom are restricted to a sublattice of size $2\ell + 1$. Its evolution is computed via ED and averaged over all possible charge and spin configurations. The main advantages of this method over TEBD or ED (on the full system) are that it operates on a much smaller Hilbert space and the possibility

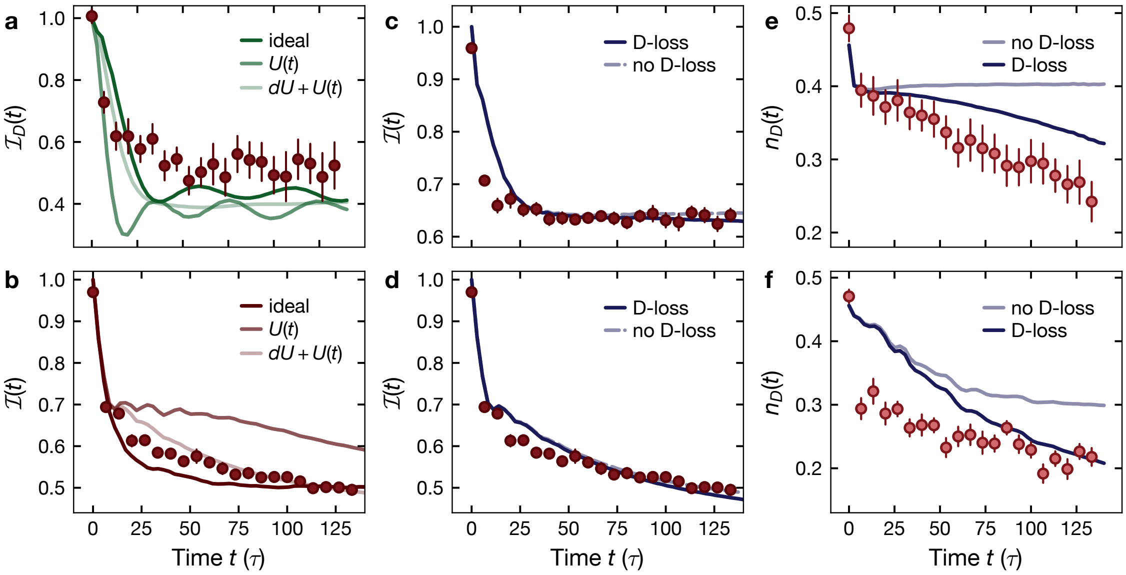

Figure 9.11.: Quantitative analysis of experimental imperfections with the approximate method: The top row presents the results for the regime $U \ll \Delta$ and the bottom row for $U \simeq 2\Delta$. The imbalance traces are all time-averaged. **a** Doublon imbalance for the ideal case, time dependent interaction $U(t)$ as well as with additional space-dependence dU. Dots represent experimental data averaged ten times and error bars showing the standard error of the mean. **b** Charge imbalance in the resonant regime with otherwise same parameters. **c, d** Charge imbalance traces showing the effect of doublon loss during time evolution (see text). Both traces also include the time- and space-dependence of U. **e, f** Dynamical evolution of the doublon fraction with and without the background loss and comparison to experimental data. All computations were performed on a system with $L = 100$ lattice sites and for the initial state a doublon fraction of 45% was used. The simulations were performed by Bharath H. M.

to include imperfections like time and spatially dependent interactions in a direct manner. In addition, it does not have finite-size effects because large systems can be simulated efficiently by averaging over multiple small subsystems with size $2\ell + 1$. Moreover, the loss of doublons can be included by solving the Lindblad Master equation

$$\dot{\hat{\rho}} = -\frac{i}{\hbar}[\hat{H}, \hat{\rho}] + \gamma \sum_{i=1}^{2\ell+1} \hat{L}_i \hat{\rho} \hat{L}_i^\dagger - \frac{1}{2}\{\hat{L}_i^\dagger \hat{L}_i, \hat{\rho}\}. \tag{9.12}$$

Herein $\hat{H}$ is the Fermi-Hubbard Hamiltonian (Eq. 9.1), $\hat{\rho}$ denotes the density matrix of a many-body mixed state and $\hat{L}_i = \hat{c}_{i,\downarrow}\hat{c}_{i,\uparrow}$ is the jump operator that represents the loss of a doublon at lattice site i. The master equation is solved with the technique explained in [234, 241].

The quantitative effects of the experimental imperfections as simulated with the approximate method and the comparison with experimental data are illustrated in Fig. 9.11.

Therein the top row depicts the results for the dipole-conserving regime and the bottom row for the resonant regime. The simulations are performed for the parameter set $(\ell, k_\uparrow, k_\downarrow, k_d) = (5, 3, 3, 3)$ and it was ensured that the traces are fully converged. The effect of time and space dependence of the interaction strength on the imbalance evolution in the dipole-conserving regime is only marginal as emphasized by Fig. 9.11a. As the main difference oscillations are damped, but the steady-state value of the time-averaged imbalance agrees. This situation is different for the resonant regime (panel b). Here the time-dependence of U changes the result drastically compared to the ideal case because initially the system is not on resonance and the resonance feature is narrow at strong tilts. Only in the long-time limit the traces approach each other. The addition of spatially varying interactions mitigates the effect because some regions of the cloud are in the resonant regime. With both imperfections included the experimental results are nicely reproduced. On top we add the effect of doublon loss due to light-assisted collisions. In both regimes (panels c and d) the charge imbalance traces are hardly distinguishable, emphasizing that the doublon loss has a negligible quantitative effect on the imbalance evolution. Finally, we compare the doublon fraction between experiment and numerics (panels e and f). The traces with doublon loss show good qualitative agreement with the experimental data points. All in all, the experimental imperfections studied here only have a small effect on the results and do not change our interpretation of the data.

9.3.6. Conclusions and outlook

In summary, we experimentally realize the tilted Fermi-Hubbard model and find indications that we indeed probe the dynamics in agreement with weak ergodicity breaking via Hilbert space fragmentation. First, we measure density-resolved imbalance time traces and show a strong dependence of the observed dynamics on the initial conditions. We succeed in describing the experimental time traces in terms of leading-order hopping processes of an effective Hamiltonian and further identify the emergent timescales at higher orders in perturbation theory directly in the experiment. Given that the effective Hamiltonian is fragmented, this comprises strong indications that we indeed realize a model that exhibits Hilbert space fragmentation in our optical lattice. Moreover, we relate the recorded steady-state imbalance to the average fragment dimension via numerical analyses. We find strong correlations as a function of the doublon fraction in the initial state, which is a hallmark of Krylov-restricted thermalization and thus a violation of strong ETH. This notion is further underlined by the entanglement entropy evolution in the resonant regime $U \simeq 2\Delta$, which seems to converge to the Page value on long time although these are beyond experimentally accessible timescales. However, this numerical investigation is not conclusive and requires further input, also from the experimental side. The reported investigation is made feasible by the technique of RF dressing that mitigates the tilt difference between both spin states. At the same time this feature can be used to implement effective spin models via precise control over the tilt difference in future projects.

The field of weak ergodicity breaking is constantly evolving at the moment and based on these new results and the current interest in Hilbert space fragmentation and quantum scars there are a couple of worthwhile research directions for future projects. First, it has been considered to extend this scheme to a two-dimensional tilted lattice system. When the tilt is applied at an irrational angle with respect to the lattice axes, the dipole moments are preserved along both directions on a prethermal timescale [88]. Moreover, such a configuration creates a quasiperiodic potential such that tilted two-dimensional systems may be relevant for the investigation of the stability of MBL in higher dimensions [96]. The dynamical properties of such 2D systems were previously studied experimentally [99] for the particular case that the tilt is aligned with one lattice axis, and theoretically [242, 243] in the context of hydrodynamic descriptions and diffusion. In addition, it is possible to study quadrupole moment conservation when adding harmonic confinement to the system. Not only can the pair hopping model, that appears in the effective Hamiltonian in the dipole-conserving regime (Eq. 9.2), be mapped to a tilted lattice, but also onto a thin torus [90, 244]. Hence, one can conceive this setting as testbed for the exploration of fractional quantum Hall physics [92, 93]. Finally, future experiments may investigate the microscopic properties of individual fragments. While we find indications of Krylov-restricted thermalization in the regime $|U| \simeq 2\Delta$, we cannot reach a conclusion for the dipole-conserving regime. It might well be that there exist as well integrable or scarred fragments as instigated in [90], which represents an interesting direction for future projects.

Part V.

Appendix

A. Parameters of the AA and GAA model

The tight-binding parameters as well as the higher order corrections, that emerge upon the transformation from the continuum (Eq. 2.2) to the lattice model (Eq. 6.1), can be calculated in two different ways, either analytically employing the Wannier functions (localized eigenfunctions of the lattice Hamiltonian) or numerically via the Wegner flow method [132]. Both methods are briefly presented in this appendix.

The tight-binding parameters of the AA model, J_0 and Δ, as well as the second-order tunneling element J_2 can be computed analytically via the unperturbed Wannier functions w_j of the primary lattice centered at site j via

$$\begin{aligned} J_0 &= -\langle w_0| \hat{H}_0 |w_1\rangle \equiv -\int_{-\infty}^{\infty} dx w_0^* \hat{H}_0 w_1, \\ \Delta &= \frac{V_d \beta^2}{2E_r^p} \langle w_0| \cos(2\beta k_p x) |w_0\rangle , \\ J_2 &= -\langle w_0| \hat{H}_0 |w_2\rangle , \end{aligned} \tag{A.1}$$

where $\hat{H}_0 = -\frac{\hbar^2}{2m}\frac{d^2}{dx^2} + \frac{V_p}{2}\cos(2k_p x)$. The remaining parameters J_1 and Δ', however, require the Wannier functions of the detuned primary lattice (superposition of detuning and primary lattice) and cannot be computed in that manner. Instead, the full set of parameters is generated with the Wegner flow approach. Where applicable both methods yield the same results and they are presented in Table A.1.

In the experiment, the distinction between the GAA and AA model is made via the primary lattice depth V_p and the detuning strength is chosen via V_d, the depth of the incommensurate lattice. In the numerics, on the other hand, a common lattice depth of $V_p = 4E_r$ for both models is chosen. For each pair (V_p, V_d) the GAA parameters are generated (see Tab. A.2) for the simulations of the time evolution. In case of the AA model, higher orders in the Hamiltonian (H' in Eq. 6.1) are removed. Thus, the conversion to the tight-binding parameters Δ/J_0 is model-independent, unlike in the experimental data.

	GAA model		**AA model**	
	$V_p = 4E_r^p$		$V_p = 8E_r^p$	
J_0/h (Hz)	1508		543	
J_2/J_0	-0.072		-0.021	
	$\Delta/J_0 = 2.1$	$\Delta/J_0 = 3.1$	$\Delta/J_0 = 2.1$	$\Delta/J_0 = 3.1$
V_d (E_r^p)	0.52	0.77	0.16	0.24
$-J_1/J_0$	0.23	0.35	0.057	0.085
$-\Delta'/J_0$	0.016	0.036	0.002	0.006
	$\Delta/J_0 = 2.5$	$\Delta/J_0 = 4.0$	$\Delta/J_0 = 2.5$	$\Delta/J_0 = 4.0$
V_d (E_r^p)	0.62	1.00	0.19	0.31
$-J_1/J_0$	0.28	0.45	0.067	0.11
$-\Delta'/J_0$	0.023	0.060	0.004	0.010

Table A.1.: Model parameters: This table summarizes the relevant parameters values form the GAA Hamiltonian in our experiment. The signs of the parameters are chosen in accordance with the convention in Eq. (6.1).

V_d (E_r^p)	0.50	0.57	0.62	0.70	0.77	0.83	0.90	1.00
Δ/J_0	2.01	2.27	2.49	2.81	3.08	3.34	3.61	4.01
$-J_1/J_0$	0.22	0.26	0.28	0.31	0.34	0.37	0.40	0.45
$-\Delta'/J_0$	0.015	0.019	0.023	0.030	0.036	0.042	0.049	0.060

Table A.2.: Conversion from the continuum model with $V_p = 4E_r^p$ to the GAA model: These parameters were derived via the Wegner flow approach. The other parameters from Eq. (6.1) only depend on the primary lattice depth V_p and are listed in Table A.1.

B. Numerical and analytical methods in the Hilbert space fragmentation project

In this appendix we list the most important numerical techniques employed in the project on Hilbert space fragmentation reported in chapter 9 to simulate the imbalance time evolution and dimensions of dynamical fragments. The composition if the code as well as the execution of most simulations were performed by Pablo Sala.

B.1. Time-evolving Block Decimation (TEBD) simulations

As explained in sec. 9.3.1, we employ TEBD simulations to reproduce our experimental imbalance time traces. This is implemented using the open source library *TeNPy* [237] applied to our spinful Fermi-Hubbard model. While the evolution of the exact Hamiltonian (Eq. 9.1) is straightforward, the time evolution of the effective Hamiltonian is defined as [117]

$$\hat{U}(t,t_0) = e^{-i\lambda\hat{S}}e^{-i(t-t_0)\hat{H}_{\text{eff}}}e^{i\lambda\hat{S}} \tag{B.1}$$

with a self-adjoint operator $\hat{S}$ given by

$$\hat{S}_{\text{dip}} = -i\sum_{i,\sigma}\left(1+\frac{U}{\Delta}\left(\hat{n}_{i+1,\bar{\sigma}}-\hat{n}_{i,\bar{\sigma}}\right)\right)\hat{c}^{\dagger}_{i,\sigma}\hat{c}_{i+1,\sigma}+\text{h.c}, \tag{B.2}$$

in the dipole-conserving regime and by

$$\hat{S}_{\text{res}} = -i\sum_{i,\sigma}\left(1-2\hat{n}_{i,\bar{\sigma}}-\frac{2}{3}\hat{n}_{i+1,\bar{\sigma}}+\frac{8}{3}\hat{n}_{i,\bar{\sigma}}\hat{n}_{i+1,\bar{\sigma}}\right)\hat{c}^{\dagger}_{i,\sigma}\hat{c}_{i+1,\sigma}+\text{h.c}, \tag{B.3}$$

in the resonant regime. The small parameter $\lambda = J/\Delta \ll 1$ leads only to approximate conservation laws in the case of finite tilt. In order to still enforce the conservation laws at leading order in perturbation theory, the additional operator $\hat{S}$ has to be taken into account. It is derived via the Schrieffer-Wolff transformation or a high-frequency expansion and is explained in [117, 133]. A direct consequence of this rotation $\hat{S}$ is that the Krylov subspaces $\mathcal{K} = \{|n\rangle\}$ are not fragmented in the number basis S^z, but in a locally dressed version $\tilde{\mathcal{K}} = \{e^{-i\hat{S}}|n\rangle\}$. However, we confirmed numerically that for our case of large tilt the overlap between the original fragment and the dressed version is large such that the admixture of other fragments can be neglected. Hence, our conclusions from chapter 9, which assumed the evolution of a state within a fixed fragment remain unchanged. Another direct consequence of the Schrieffer-Wolff rotation can be seen for example in Fig. 9.4a for the singlon CDW. Although the state is frozen under the evolution with $\hat{H}_{\text{eff}}^{\text{dip}}$ and the fractal dimension $\mathcal{C}_{\psi} = 0$, the numerical imbalance $\bar{\mathcal{I}}_C = 0.88$. The imbalance is measured in the S^z-basis while the fragment is defined in the rotated basis $e^{-i\hat{S}}$. This basis transformation weakly admixes other fragments and thus explains the reduced imbalance.

B.2. Dimensions of analytical fragments

In Figs. 9.4 and 9.5 we showed the mean fractal dimension $\bar{\mathcal{C}}_{n_D}$ obtained from averaging over families of initial states with the same doublon fraction n_D. Here we show the distribution of individual states for completeness. The effective Hamiltonian is treated as an adjacency matrix in the local S_z-basis, the relevant basis choice for the incoherent product states produced in the experiment, yielding the fragmented structure of the full Hilbert space as well as the dynamical fragment of a certain initial state. For this type of simulations we use ED on 13 lattice sites and realize all possible charge distributions starting from a Néel-ordered singlon CDW background and adding additional atoms to form doublons. This yields a fixed number of possible states for a given doublon fraction and their relative fractal dimension $\mathcal{C}_{\psi}$ is plotted in Fig. B.1a for the dipole-conserving regime and Fig. B.1b in the resonant regime $U \simeq 2\Delta$. Note that in the former case we have to enforce doublon number conservation as explained in sec. 9.3.1 to obtain the physically relevant fragments given the diagonal interaction energy. We observe certain fluctuations in the fragment dimension that come from states with strong boundary effects where the doublons are accumulated contiguously at the edge of the system and this effect is even more pronounced in the resonant regime such that some points are not shown in Fig. B.1b and omitted in the computation of the average dimension [234]. After all, these atypical configurations occur due to strong boundary effects in the small system and bear no physical relevance for the states prepared in the actual experiment. Apart from that we infer that the fragment statistics within different symmetry sectors are well-behaved such that the relation we draw between the steady-state imbalance and average fractal dimension is justified.

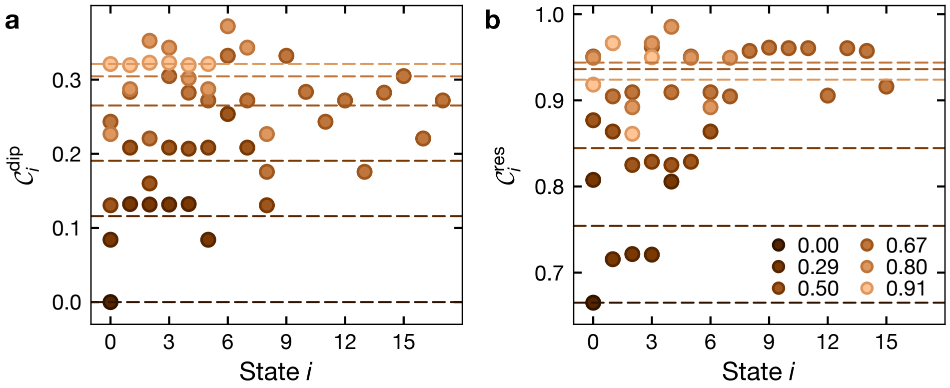

Figure B.1.: Statistics of fractal dimensions: Relative fragment dimension with respect to the full symmetry sector resolved by the concrete state for all initial doublon fractions studied numerically in the main text. The dashed horizontal lines indicate the average value for all states with the same doublon fraction n_D (values given in the legend of panel b). **a** Dipole-conserving regime $\Delta \gg U, J$ **b** Resonance regime $U \simeq 2\Delta$.

Bibliography

[1] L. Boltzmann. "Ueber die Eigenschaften monocyclischer und anderer damit verwandter Systeme." 1885.98 (1885), pp. 68–94 (cit. on p. 1).

[2] R. Nandkishore and D. A. Huse. "Many-Body Localization and Thermalization in Quantum Statistical Mechanics". *Annual Review of Condensed Matter Physics* 6.1 (2015), pp. 15–38 (cit. on pp. 1, 9).

[3] J. M. Deutsch. "Quantum statistical mechanics in a closed system". *Phys. Rev. A* 43 (4 1991), p. 2046 (cit. on pp. 1, 10, 13).

[4] M. Srednicki. "Chaos and quantum thermalization". *Phys. Rev. E* 50 (2 1994), p. 888 (cit. on pp. 1, 10, 13).

[5] M. Rigol, V. Dunjko, and M. Olshanii. "Thermalization and its mechanism for generic isolated quantum systems". *Nature* 452.854 (2008) (cit. on pp. 1, 11).

[6] H. Bethe. "Zur Theorie der Metalle". *Zeitschrift für Physik* 71 (3 1931), pp. 205–226 (cit. on pp. 1, 11).

[7] J. Hubbard. "Electron correlations in narrow energy bands". *Proc. R. Soc. Lond. A* 276 (1963), pp. 238–257 (cit. on pp. 1, 4, 49).

[8] E. H. Lieb and W. Liniger. "Exact Analysis of an Interacting Bose Gas. I. The General Solution and the Ground State". *Phys. Rev.* 130 (4 1963), pp. 1605–1616 (cit. on pp. 1, 11).

[9] A. Klümper. "Integrability of quantum chains: Theory and applications to the spin-1/2 XXZ chain". *Lecture Notes in Physics* 645 (2005) (cit. on pp. 1, 11).

[10] P. W. Anderson. "Localized Magnetic States in Metals". *Phys. Rev.* 124 (1 1961), pp. 41–53 (cit. on p. 1).

[11] P. W. Anderson. "Absence of Diffusion in Certain Random Lattices". *Phys. Rev.* 109 (5 1958), p. 1492 (cit. on pp. 1, 13, 32).

[12] D. M. Basko, I. L. Aleiner, and B. L. Altshuler. "Metal–insulator transition in a weakly interacting many-electron system with localized single-particle states". *Ann. Phys.* 321.5 (2006), p. 1126 (cit. on pp. 1, 2, 17, 33, 91).

[13] V. Oganesyan and D. A. Huse. “Localization of interacting fermions at high temperature”. *Phys. Rev. B* 75 (15 2007), p. 155111 (cit. on pp. 1, 17, 19).

[14] A. Pal and D. A. Huse. “Many-body localization phase transition”. *Phys. Rev. B* 82 (17 2010), p. 174411 (cit. on pp. 1, 18, 24, 34).

[15] D. A. Abanin and Z. Papić. “Recent progress in many-body localization”. *Annalen der Physik* 529.7 (2017), p. 1700169 (cit. on pp. 1, 13, 18).

[16] D. A. Abanin, E. Altman, I. Bloch, and M. Serbyn. “Colloquium: Many-body localization, thermalization, and entanglement”. *Rev. Mod. Phys.* 91 (2 2019), p. 021001 (cit. on pp. 1, 10, 18).

[17] F. Alet and N. Laflorencie. “Many-body localization: An introduction and selected topics”. *Comptes Rendus Physique* 19.6 (2018). Quantum simulation / Simulation quantique, pp. 498–525 (cit. on pp. 1, 13, 18).

[18] T. C. Berkelbach and D. R. Reichman. “Conductivity of disordered quantum lattice models at infinite temperature: Many-body localization”. *Phys. Rev. B* 81 (22 2010), p. 224429 (cit. on pp. 1, 80).

[19] O. S. Barišić and P. Prelovšek. “Conductivity in a disordered one-dimensional system of interacting fermions”. *Phys. Rev. B* 82 (16 2010), p. 161106 (cit. on pp. 1, 80).

[20] F. Setiawan, D.-L. Deng, and J. H. Pixley. “Transport properties across the many-body localization transition in quasiperiodic and random systems”. *Phys. Rev. B* 96 (10 2017), p. 104205 (cit. on pp. 1, 80).

[21] J. H. Bardarson, F. Pollmann, and J. E. Moore. “Unbounded Growth of Entanglement in Models of Many-Body Localization”. *Phys. Rev. Lett.* 109 (1 2012), p. 017202 (cit. on pp. 1, 20).

[22] M. Serbyn, Z. Papić, and D. A. Abanin. “Universal Slow Growth of Entanglement in Interacting Strongly Disordered Systems”. *Phys. Rev. Lett.* 110 (26 2013), p. 260601 (cit. on pp. 2, 20).

[23] D. A. Huse, R. Nandkishore, and V. Oganesyan. “Phenomenology of fully many-body-localized systems”. *Phys. Rev. B* 90 (17 2014), p. 174202 (cit. on pp. 2, 19).

[24] S. Aubry and G. André. “Analyticity breaking and Anderson localization in incommensurate lattices”. *Ann. Israel Phys. Soc.* 3.133 (1980) (cit. on pp. 2, 14, 74, 86).

[25] S. Iyer, V. Oganesyan, G. Refael, and D. A. Huse. “Many-body localization in a quasiperiodic system”. *Phys. Rev. B* 87 (13 2013), p. 134202 (cit. on pp. 2, 15, 86).

[26] J. Billy, V. Josse, Z. Zuo, A. Bernard, B. Hambracht, P. Lugan, D. Clément, L. Sanchez-Palencia, P. Bouyer, and A. Aspect. "Direct observation of Anderson localization of matter waves in a controlled disorder". *Nature* 453 (2008), pp. 891–894 (cit. on pp. 2, 14).

[27] T. Schwartz, G. Bartal, S. Fishman, and M. Segev. "Transport and Anderson localization in disordered two-dimensional photonic lattices". *Nature* 446 (2007), pp. 52–55 (cit. on pp. 2, 14).

[28] G. Roati, C. D'Errico, L. Fallani, M. Fattori, C. Fort, M. Zaccanti, G. Modugno, M. Modugno, and M. Inguscio. "Anderson localization in an non-interacting Bose-Einstein condensate". *Nature* 435 (2008), pp. 895–898 (cit. on pp. 2, 16, 71).

[29] M. Schreiber, S. S. Hodgman, P. Bordia, H. P. Lüschen, M. H. Fischer, R. Vosk, E. Altman, U. Schneider, and I. Bloch. "Observation of many-body localization of interacting fermions in a quasirandom optical lattice". *Science* 349.6250 (2015), p. 842 (cit. on pp. 2, 4, 16, 17, 22, 41, 71, 83–86).

[30] R. Islam, R. Ma, P. M. Preiss, M. E. Tai, A. Lukin, M. Rispoli, and M. Greiner. "Measuring entanglement entropy in a quantum many-body system". *Nature* 528 (2015), pp. 77–83 (cit. on pp. 2, 22).

[31] A. Lukin, M. Rispoli, R. Schittko, M. E. Tai, A. M. Kaufman, S. Choi, V. Khemani, J. Léonard, and M. Greiner. "Probing entanglement in a many-body–localized system". *Science* 364.6437 (2019), pp. 256–260 (cit. on pp. 2, 22).

[32] J. Smith, A. Lee, P. Richerme, B. Neyenhuis, P. W. Hess, P. Hauke, M. Heyl, D. A. Huse, and C. Monroe. "Many-body localization in a quantum simulator with programmable random disorder". *Nat. Phys.* 12 (2016), pp. 907–911 (cit. on pp. 2, 23).

[33] P. Roushan et al. "Spectroscopic signatures of localization with interacting photons in superconducting qubits". *Science* 358.6367 (2017), pp. 1175–1179 (cit. on pp. 2, 23).

[34] K. Xu, J.-J. Chen, Y. Zeng, Y.-R. Zhang, C. Song, W. Liu, Q. Guo, P. Zhang, D. Xu, H. Deng, K. Huang, H. Wang, X. Zhu, D. Zheng, and H. Fan. "Emulating Many-Body Localization with a Superconducting Quantum Processor". *Phys. Rev. Lett.* 120 (5 2018), p. 050507 (cit. on p. 2).

[35] K. X. Wei, C. Ramanathan, and P. Cappellaro. "Exploring Localization in Nuclear Spin Chains". *Phys. Rev. Lett.* 120 (7 2018), p. 070501 (cit. on p. 2).

[36] P. Ponte, Z. Papić, F. Huveneers, and D. A. Abanin. "Many-Body Localization in Periodically Driven Systems". *Phys. Rev. Lett.* 114 (14 2015), p. 140401 (cit. on p. 2).

[37] P. Ponte, A. Chandran, Z. Papić, and D. A. Abanin. “Periodically driven ergodic and many-body localized quantum systems”. *Annals of Physics* 353 (2015), pp. 196–204 (cit. on p. 2).

[38] A. Lazarides, A. Das, and R. Moessner. “Fate of Many-Body Localization Under Periodic Driving”. *Phys. Rev. Lett.* 115 (3 2015), p. 030402 (cit. on p. 2).

[39] D. A. Abanin, W. De Roeck, and F. Huveneers. “Theory of many-body localization in periodically driven systems”. *Annals of Physics* 372 (2016), pp. 1–11 (cit. on p. 2).

[40] P. Bordia, H. Lüschen, U. Schneider, M. Knap, and I. Bloch. “Periodically driving a many-body localized quantum system”. *Nature Physics* 13 (2017), pp. 460–464 (cit. on pp. 2, 83).

[41] D. J. Luitz, N. Laflorencie, and F. Alet. “Extended slow dynamical regime close to the many-body localization transition”. *Phys. Rev. B* 93 (6 2016), p. 060201 (cit. on pp. 2, 24, 34, 90).

[42] K. Agarwal, S. Gopalakrishnan, M. Knap, M. Müller, and E. Demler. “Anomalous Diffusion and Griffiths Effects Near the Many-Body Localization Transition”. *Phys. Rev. Lett.* 114 (16 2015), p. 160401 (cit. on pp. 2, 24).

[43] R. Vosk, D. A. Huse, and E. Altman. “Theory of the Many-Body Localization Transition in One-Dimensional Systems”. *Phys. Rev. X* 5 (3 2015), p. 031032 (cit. on pp. 2, 25, 87, 120).

[44] A. C. Potter, R. Vasseur, and S. A. Parameswaran. “Universal Properties of Many-Body Delocalization Transitions”. *Phys. Rev. X* 5 (3 2015), p. 031033 (cit. on pp. 2, 25, 87).

[45] S. A. Parameswaran, A. C. Potter, and R. Vasseur. “Eigenstate phase transitions and the emergence of universal dynamics in highly excited states”. *Annalen der Physik* 529.7 (2017), p. 1600302 (cit. on pp. 2, 24).

[46] D. J. Luitz and Y. B. Lev. “The ergodic side of the many-body localization transition”. *Annalen der Physik* 529.7 (2017), p. 1600350 (cit. on pp. 2, 24).

[47] K. Agarwal, E. Altman, E. Demler, S. Gopalakrishnan, D. A. Huse, and M. Knap. “Rare-region effects and dynamics near the many-body localization transition”. *Annalen der Physik* 529.7 (2017), p. 1600326 (cit. on pp. 2, 24).

[48] H. P. Lüschen, P. Bordia, S. Scherg, F. Alet, E. Altman, U. Schneider, and I. Bloch. “Observation of Slow Dynamics near the Many-Body Localization Transition in One-Dimensional Quasiperiodic Systems”. *Phys. Rev. Lett.* 119 (26 2017), p. 260401 (cit. on pp. 2, 4, 25, 26, 83–87, 89, 90, 96).

[49] M. Rispoli, A. Lukin, R. Schittko, S. Kim, M. E. Tai, J. Léonard, and M. Greiner. "Quantum critical behavior at the many-body localization transition". *Nature* 573 (2019), pp. 385–389 (cit. on pp. 2, 22, 71).

[50] I.-D. Potirniche, S. Banerjee, and E. Altman. "Exploration of the stability of many-body localization in $d > 1$". *Phys. Rev. B* 99 (20 2019), p. 205149 (cit. on pp. 2, 23).

[51] T. B. Wahl, A. Pal, and S. H. Simon. "Signatures of the many-body localized regime in two dimensions". *Nature Physics* 15 (2019), pp. 164–169 (cit. on pp. 2, 23).

[52] E. Chertkov, B. Villalonga, and B. K. Clark. "Numerical evidence for many-body localization in two and three dimensions". *arXiv:2007.02959* (2020) (cit. on pp. 2, 23).

[53] P. Bordia, H. Lüschen, S. Scherg, S. Gopalakrishnan, M. Knap, U. Schneider, and I. Bloch. "Probing Slow Relaxation and Many-Body Localization in Two-Dimensional Quasiperiodic Systems". *Phys. Rev. X* 7 (4 2017), p. 041047 (cit. on pp. 2, 23).

[54] J.-y. Choi, S. Hild, J. Zeiher, P. Schauß, A. Rubio-Abadal, T. Yefsah, V. Khemani, D. A. Huse, I. Bloch, and C. Gross. "Exploring the many-body localization transition in two dimensions". *Science* 352.6293 (2016), pp. 1547–1552 (cit. on pp. 2, 4, 23).

[55] M. H. Fischer, M. Maksymenko, and E. Altman. "Dynamics of a Many-Body-Localized System Coupled to a Bath". *Phys. Rev. Lett.* 116 (16 2016), p. 160401 (cit. on pp. 2, 3, 26, 27, 90).

[56] R. Nandkishore, S. Gopalakrishnan, and D. A. Huse. "Spectral features of a many-body-localized system weakly coupled to a bath". *Phys. Rev. B* 90 (6 2014), p. 064203 (cit. on pp. 2, 3, 26, 90).

[57] E. Levi, M. Heyl, I. Lesanovsky, and J. P. Garrahan. "Robustness of Many-Body Localization in the Presence of Dissipation". *Phys. Rev. Lett.* 116 (23 2016), p. 237203 (cit. on pp. 2, 3, 26, 27).

[58] R. Nandkishore. "Many-body localization proximity effect". *Phys. Rev. B* 92 (24 2015), p. 245141 (cit. on pp. 2, 3, 26, 81).

[59] R. Nandkishore and S. Gopalakrishnan. "Many body localized systems weakly coupled to baths". *Annalen der Physik* 529.7 (2017), p. 1600181 (cit. on pp. 2, 3, 26).

[60] P. Bordia, H. P. Lüschen, S. S. Hodgman, M. Schreiber, I. Bloch, and U. Schneider. "Coupling Identical one-dimensional Many-Body Localized Systems". *Phys. Rev. Lett.* 116 (14 2016), p. 140401 (cit. on pp. 2–4, 27, 84, 88, 94).

[61] H. P. Lüschen, P. Bordia, S. S. Hodgman, M. Schreiber, S. Sarkar, A. J. Daley, M. H. Fischer, E. Altman, I. Bloch, and U. Schneider. “Signatures of Many-Body Localization in a Controlled Open Quantum System”. *Phys. Rev. X* 7 (1 2017), p. 011034 (cit. on pp. 2, 3, 27, 84, 87, 94).

[62] A. Rubio-Abadal, J.-y. Choi, J. Zeiher, S. Hollerith, J. Rui, I. Bloch, and C. Gross. “Many-Body Delocalization in the Presence of a Quantum Bath”. *Phys. Rev. X* 9 (4 2019), p. 041014 (cit. on pp. 2, 23).

[63] D. J. Luitz, N. Laflorencie, and F. Alet. “Many-body localization edge in the random-field Heisenberg chain”. *Phys. Rev. B* 91 (8 2015), p. 081103 (cit. on pp. 2, 18, 34, 85).

[64] D. J. Luitz. “Long tail distributions near the many-body localization transition”. *Phys. Rev. B* 93 (13 2016), p. 134201 (cit. on pp. 2, 34).

[65] E. Baygan, S. P. Lim, and D. N. Sheng. “Many-body localization and mobility edge in a disordered spin-$\frac{1}{2}$ Heisenberg ladder”. *Phys. Rev. B* 92 (19 2015), p. 195153 (cit. on pp. 2, 34).

[66] E. J. Torres-Herrera and L. F. Santos. “Extended nonergodic states in disordered many-body quantum systems”. *Ann. Phys. (Berlin)* 529.7 (2017), p. 1600284 (cit. on pp. 2, 34).

[67] W. De Roeck, F. Huveneers, M. Müller, and M. Schiulaz. “Absence of many-body mobility edges”. *Phys. Rev. B* 93 (1 2016), p. 014203 (cit. on pp. 2, 79).

[68] P. Brighi, D. A. Abanin, and M. Serbyn. “Stability of mobility edges in disordered interacting systems”. *Phys. Rev. B* 102 (6 2020), p. 060202 (cit. on pp. 2, 80).

[69] N. Y. Yao, C. R. Laumann, J. I. Cirac, M. D. Lukin, and J. E. Moore. “Quasi-Many-Body Localization in Translation-Invariant Systems”. *Phys. Rev. Lett.* 117 (24 2016), p. 240601 (cit. on pp. 2, 28).

[70] A. Smith, J. Knolle, D. L. Kovrizhin, and R. Moessner. “Disorder-Free Localization”. *Phys. Rev. Lett.* 118 (26 2017), p. 266601 (cit. on pp. 2, 28).

[71] A. Smith, J. Knolle, R. Moessner, and D. L. Kovrizhin. “Absence of Ergodicity without Quenched Disorder: From Quantum Disentangled Liquids to Many-Body Localization”. *Phys. Rev. Lett.* 119 (17 2017), p. 176601 (cit. on pp. 2, 28).

[72] L. Barbiero, C. Menotti, A. Recati, and L. Santos. “Out-of-equilibrium states and quasi-many-body localization in polar lattice gases”. *Phys. Rev. B* 92 (18 2015), p. 180406 (cit. on pp. 2, 28).

[73] G. Carleo, F. Becca, Schiró, and M. Fabrizio. “Localization and glassy dynamics of many-body quantum systems”. *Sci. Rep.* 2 (243 2012) (cit. on pp. 2, 28).

[74] M. Schiulaz and M. Müller. “Ideal quantum glass transitions: Many-body localization without quenched disorder”. *AIP Conference Proceedings* 1610.1 (2014), pp. 11–23 (cit. on pp. 2, 28).

[75] M. Schiulaz, A. Silva, and M. Müller. “Dynamics in many-body localized quantum systems without disorder”. *Phys. Rev. B* 91 (18 2015), p. 184202 (cit. on pp. 2, 28).

[76] H. Bernien, S. Schwartz, A. Keesling, H. Levine, A. Omran, H. Pichler, S. Choi, A. S. Zibrov, M. Endres, M. Greiner, V. Vuletić, and M. D. Lukin. “Probing many-body dynamics on a 51-atom quantum simulator”. *Nature* (551 2017), pp. 579–584 (cit. on pp. 3, 38).

[77] C. J. Turner, A. A. Michailidis, D. A. Abanin, M. Serbyn, and Z. Papić. “Quantum scarred eigenstates in a Rydberg atom chain: Entanglement, breakdown of thermalization, and stability to perturbations”. *Phys. Rev. B* 98 (15 2018), p. 155134 (cit. on pp. 3, 38).

[78] C. J. Turner, A. A. Michailidis, D. A. Abanin, M. Serbyn, and Z. Papić. “Weak ergodicity breaking from quantum many-body scars”. *Nat. Phys.* 14 (2018), pp. 745–749 (cit. on pp. 3, 38).

[79] J.-Y. Desaules, A. Hudomal, C. J. Turner, and Z. Papić. “A proposal for realizing quantum scars in the tilted 1D Fermi-Hubbard model”. *arXiv:2102.01675* (2021) (cit. on pp. 3, 39, 127).

[80] H. Zhao, J. Vovrosh, F. Mintert, and J. Knolle. “Quantum Many-Body Scars in Optical Lattices”. *Phys. Rev. Lett.* 124 (16 2020), p. 160604 (cit. on pp. 3, 39).

[81] S. Pai, M. Pretko, and R. M. Nandkishore. “Localization in Fractonic Random Circuits”. *Phys. Rev. X* 9 (2 2019), p. 021003 (cit. on pp. 3, 35, 39, 116).

[82] K. Bull, I. Martin, and Z. Papić. “Systematic Construction of Scarred Many-Body Dynamics in 1D Lattice Models”. *Phys. Rev. Lett.* 123 (3 2019), p. 030601 (cit. on pp. 3, 39).

[83] M. Schecter and T. Iadecola. “Weak Ergodicity Breaking and Quantum Many-Body Scars in Spin-1 *XY* Magnets”. *Phys. Rev. Lett.* 123 (14 2019), p. 147201 (cit. on pp. 3, 39).

[84] C.-J. Lin and O. I. Motrunich. “Exact Quantum Many-Body Scar States in the Rydberg-Blockaded Atom Chain”. *Phys. Rev. Lett.* 122 (17 2019), p. 173401 (cit. on pp. 3, 39).

[85] C. Chen, F. Burnell, and A. Chandran. “How Does a Locally Constrained Quantum System Localize?” *Phys. Rev. Lett.* 121 (8 2018), p. 085701 (cit. on pp. 3, 39).

[86] R. M. Nandkishore and M. Hermele. “Fractons”. *Annual Review of Condensed Matter Physics* 10.1 (2019), pp. 295–313 (cit. on pp. 3, 35).

[87] P. Sala, T. Rakovszky, R. Verresen, M. Knap, and F. Pollmann. "Ergodicity Breaking Arising from Hilbert Space Fragmentation in Dipole-Conserving Hamiltonians". *Phys. Rev. X* 10 (1 2020), p. 011047 (cit. on pp. 3, 35, 37–39, 41, 109, 116, 123, 126).

[88] V. Khemani, M. Hermele, and R. Nandkishore. "Localization from Hilbert space shattering: From theory to physical realizations". *Phys. Rev. B* 101 (17 2020), p. 174204 (cit. on pp. 3, 35–37, 39, 41, 109, 116, 134).

[89] S. R. Taylor, M. Schulz, F. Pollmann, and R. Moessner. "Experimental probes of Stark many-body localization". *Phys. Rev. B* 102 (5 2020), p. 054206 (cit. on pp. 3, 29, 36, 39–41, 116, 119).

[90] S. Moudgalya, A. Prem, R. Nandkishore, N. Regnault, and B. A. Bernevig. "Thermaliization and its absence within Krylov subspaces of constrained a constrained Hamiltonian". *arXiv:1910.14048* (2019) (cit. on pp. 3, 37, 41, 108, 109, 116, 123, 124, 134).

[91] E. V. H. Doggen, I. V. Gornyi, and D. G. Polyakov. "Stark many-body localization: Evidence for Hilbert-space shattering". *Phys. Rev. B* 103 (10 2021), p. L100202 (cit. on pp. 3, 41).

[92] E. H. Rezayi and F. D. M. Haldane. "Laughlin state on stretched and squeezed cylinders and edge excitations in the quantum Hall effect". *Phys. Rev. B* 50 (23 1994), pp. 17199–17207 (cit. on pp. 3, 134).

[93] C. H. Lee, Z. Papić, and R. Thomale. "Geometric Construction of Quantum Hall Clustering Hamiltonians". *Phys. Rev. X* 5 (4 2015), p. 041003 (cit. on pp. 3, 134).

[94] M. Nakamura, Z.-Y. Wang, and E. J. Bergholtz. "Exactly Solvable Fermion Chain Describing a $\nu = 1/3$ Fractional Quantum Hall State". *Phys. Rev. Lett.* 109 (1 2012), p. 016401 (cit. on pp. 3, 36).

[95] M. Schulz, C. A. Hooley, R. Moessner, and F. Pollmann. "Stark Many-Body Localization". *Phys. Rev. Lett.* 122 (4 2019), p. 040606 (cit. on pp. 3, 29, 36, 39, 109, 119).

[96] E. van Nieuwenburg, Y. Baum, and G. Refael. "From Bloch oscillations to many-body localization in clean interacting systems". *Proceedings of the National Academy of Sciences* 116.19 (2019), pp. 9269–9274 (cit. on pp. 3, 29, 36, 39, 42, 119, 134).

[97] F. Meinert, M. J. Mark, E. Kirilov, K. Lauber, P. Weinmann, M. Gröbner, and H.-C. Nägerl. "Interaction-Induced Quantum Phase Revivals and Evidence for the Transition to the Quantum Chaotic Regime in 1D Atomic Bloch Oscillations". *Phys. Rev. Lett.* 112 (19 2014), p. 193003 (cit. on pp. 3, 103).

[98] E. Haller, R. Hart, M. J. Mark, J. G. Danzl, L. Reichsöllner, and H.-C. Nägerl. "Inducing Transport in a Dissipation-Free Lattice with Super Bloch Oscillations". *Phys. Rev. Lett.* 104 (20 2010), p. 200403 (cit. on pp. 3, 103).

[99] E. Guardado-Sanchez, A. Morningstar, B. M. Spar, P. T. Brown, D. A. Huse, and W. S. Bakr. “Subdiffusion and Heat Transport in a Tilted Two-Dimensional Fermi-Hubbard System”. *Phys. Rev. X* 10 (1 2020), p. 011042 (cit. on pp. 3, 4, 104, 134).

[100] I. Dimitrova, N. Jepsen, A. Buyskikh, A. Venegas-Gomez, J. Amato-Grill, A. Daley, and W. Ketterle. “Enhanced Superexchange in a Tilted Mott Insulator”. *Phys. Rev. Lett.* 124 (4 2020), p. 043204 (cit. on pp. 3, 104).

[101] L.-N. Wu and A. Eckardt. “Bath-Induced Decay of Stark Many-Body Localization”. *Phys. Rev. Lett.* 123 (3 2019), p. 030602 (cit. on pp. 3, 119).

[102] C. Chin, R. Grimm, P. Julienne, and E. Tiesinga. “Feshbach resonances in ultracold gases”. *Rev. Mod. Phys.* 82 (2 2010), pp. 1225–1286 (cit. on pp. 3, 50).

[103] G. Gauthier, T. A. Bell, A. B. Stilgoe, H. Rubinsztein-Dunlop, T. W. Neely, and M. Baker. “Dynamic high-resolution optical trapping of ultracold atoms”. *arXiv:2103.10020* (2021) (cit. on p. 3).

[104] I. Bloch, J. Dalibard, and W. Zwerger. “Many-body physics with ultracold gases”. *Rev. Mod. Phys.* 80 (3 2008), p. 885 (cit. on p. 4).

[105] C. Gross and W. S. Bakr. “Quantum gas microscopy for single atom and spin detection”. *arXiv:2010.15407* (2020) (cit. on p. 4).

[106] L. W. Cheuk, M. A. Nichols, M. Okan, T. Gersdorf, V. V. Ramasesh, W. S. Bakr, T. Lompe, and M. W. Zwierlein. “Quantum-Gas Microscope for Fermionic Atoms”. *Phys. Rev. Lett.* 114 (19 2015), p. 193001 (cit. on p. 4).

[107] M. F. Parsons, F. Huber, A. Mazurenko, C. S. Chiu, W. Setiawan, K. Wooley-Brown, S. Blatt, and M. Greiner. “Site-Resolved Imaging of Fermionic ^{6}Li in an Optical Lattice”. *Phys. Rev. Lett.* 114 (21 2015), p. 213002 (cit. on p. 4).

[108] G. J. A. Edge, R. Anderson, D. Jervis, D. C. McKay, R. Day, S. Trotzky, and J. H. Thywissen. “Imaging and addressing of individual fermionic atoms in an optical lattice”. *Phys. Rev. A* 92 (6 2015), p. 063406 (cit. on p. 4).

[109] A. Omran, M. Boll, T. A. Hilker, K. Kleinlein, G. Salomon, I. Bloch, and C. Gross. “Microscopic Observation of Pauli Blocking in Degenerate Fermionic Lattice Gases”. *Phys. Rev. Lett.* 115 (26 2015), p. 263001 (cit. on p. 4).

[110] M. Boll, T. A. Hilker, G. Salomon, A. Omran, J. Nespolo, L. Pollet, I. Bloch, and C. Gross. “Spin- and density-resolved microscopy of antiferromagnetic correlations in Fermi-Hubbard chains”. *Science* 353.6305 (2016), pp. 1257–1260 (cit. on p. 4).

[111] G. Salomon, J. Koepsell, J. Vijayan, T. A. Hilker, J. Nespolo, L. Pollet, I. Bloch, and C. Gross. “Direct observation of incommensurate magnetism in Hubbard chains”. *Nature* 565 (7737 2019), pp. 56–60 (cit. on p. 4).

[112] J. Vijayan, P. Sompet, G. Salomon, J. Koepsell, S. Hirthe, A. Bohrdt, F. Grusdt, I. Bloch, and C. Gross. “Time-resolved observation of spin-charge deconfinement in fermionic Hubbard chains”. *Science* 367.6474 (2020), pp. 186–189 (cit. on p. 4).

[113] A. Mazurenko, C. S. Chiu, G. Ji, M. F. Parsons, M. Kanász-Nagy, R. Schmidt, F. Grusdt, E. Demler, D. Greif, and M. Greiner. “A cold-atom Fermi-Hubbard antiferromagnet”. *Nature* 545 (7655 2017), pp. 462–466 (cit. on p. 4).

[114] P. T. Brown, D. Mitra, E. Guardado-Sanchez, R. Nourafkan, A. Reymbaut, C.-D. Hébert, S. Bergeron, A.-M. S. Tremblay, J. Kokalj, D. A. Huse, P. Schauß, and W. S. Bakr. “Bad metallic transport in a cold atom Fermi-Hubbard system”. *Science* 363.6425 (2019), pp. 379–382 (cit. on pp. 4, 50).

[115] D.-H. Lee. “Routes to High-Temperature Superconductivity: A Lesson from FeSe / SrTiO3”. *Annual Review of Condensed Matter Physics* 9.1 (2018), pp. 261–282 (cit. on p. 4).

[116] P. A. Lee. “From high temperature superconductivity to quantum spin liquid: progress in strong correlation physics”. *Rep. Prog. Phys.* 71 (2007), p. 012501 (cit. on p. 4).

[117] S. Scherg, T. Kohlert, P. Sala, F. Pollmann, B. H. M., I. Bloch, and M. Aidelsburger. “Observing non-ergodicity due to kinetic constraints in tilted Fermi-Hubbard chains”. *arXiv:2010.12965* (2020) (cit. on pp. 4, 47, 56, 59, 60, 102, 105, 107, 108, 110–112, 116, 120, 121, 126, 130, 139).

[118] E. Guardado-Sanchez, B. M. Spar, P. Schauss, R. Belyansky, J. T. Young, P. Bienias, A. V. Gorshkov, T. Iadecola, and W. S. Bakr. “Quench dynamics of a Fermi gas with strong long-range interactions”. *arXiv:2010.05871* (2020) (cit. on p. 4).

[119] H. P. Lüschen, S. Scherg, T. Kohlert, M. Schreiber, P. Bordia, X. Li, S. Das Sarma, and I. Bloch. “Single-Particle Mobility Edge in a One-Dimensional Quasiperiodic Optical Lattice”. *Phys. Rev. Lett.* 120 (16 2018), p. 160404 (cit. on pp. 5, 47, 73, 76, 77, 84, 96).

[120] H. P. Lüschen. “Localization of ultracold atoms in quasi-periodic optical lattices”. PhD thesis. 2018 (cit. on pp. 9, 13, 15, 18, 25, 71, 76, 77).

[121] P. Bordia. “Probing many-body localization with ultracold atoms in optical lattices”. PhD thesis. 2017 (cit. on pp. 9, 13, 18).

[122] J. Lux, J. Müller, A. Mitra, and A. Rosch. “Hydrodynamic long-time tails after a quantum quench”. *Phys. Rev. A* 89 (5 2014), p. 053608 (cit. on p. 9).

[123] N. S. Krylov. *Works on the Foundations of Statistical Physics*. Princeton University Press, 2016 (cit. on p. 9).

[124] J. von Plato. “Boltzmann’s ergodic hypothesis”. *Archive for History of Exact Sciences* 42 (1), pp. 71–89 (cit. on p. 10).

[125] B. S. Shastry. “Exact Integrability of the One-Dimensional Hubbard Model”. *Phys. Rev. Lett.* 56 (23 1986), pp. 2453–2455 (cit. on p. 11).

[126] S. Scherg, T. Kohlert, J. Herbrych, J. Stolpp, P. Bordia, U. Schneider, F. Heidrich-Meisner, I. Bloch, and M. Aidelsburger. “Nonequilibrium Mass Transport in the 1D Fermi-Hubbard Model”. *Phys. Rev. Lett.* 121 (13 2018), p. 130402 (cit. on pp. 11, 47, 60, 63, 64, 112, 114, 118, 128).

[127] D. A. Abanin, E. Altman, I. Bloch, and M. Serbyn. “Colloquium: Many-body localization, thermalization, and entanglement”. *Rev. Mod. Phys.* 91 (2 2019), p. 021001 (cit. on p. 13).

[128] H. Hu, A. Strybulevych, J. H. Page, S. E. Skipetrov, and B. A. van Tiggelen. “Localization of ultrasound in a three-simensional elastic network”. *Nat. Phys.* 4 (2008), pp. 945–948 (cit. on p. 14).

[129] F. Jendrzejewski, A. Bernard, K. Muller, P. Cheinet, V. Josse, M. Piraud, L. Pezze, L. Sanchez-Palencia, A. Aspect, and P. Bouyer. “Three-dimensional localization of ultracold atoms in an optical disordered potential”. *Nat. Phys.* 8.5 (2012), pp. 398–403 (cit. on pp. 14, 33).

[130] W. R. McGehee, S. S. Kondov, W. Xu, J. J. Zirbel, and B. DeMarco. “Three-Dimensional Anderson Localization in Variable Scale Disorder”. *Phys. Rev. Lett.* 111 (14 2013), p. 145303 (cit. on pp. 14, 33).

[131] M. Modugno. “Exponential localization in one-dimensional quasi-periodic optical lattices”. *New Journal of Physics* 11.3 (2009), p. 033023 (cit. on p. 15).

[132] X. Li, X. Li, and S. Das Sarma. “Mobility edges in one-dimensional bichromatic incommensurate potentials”. *Phys. Rev. B* 96 (8 2017), p. 085119 (cit. on pp. 15, 33, 71–73, 77, 85, 137).

[133] S. Scherg. “Probing nonequilibrium dynamics in Fermi-Hubbard chains - from extensively-many to few conserved quantities”. 2021 (cit. on pp. 15, 50, 101–105, 108, 130, 139).

[134] L. Fleishman and P. W. Anderson. “Interactions and the Anderson transition”. *Phys. Rev. B* 21 (6 1980), pp. 2366–2377 (cit. on p. 17).

[135] M. Žnidarič, T. Prosen, and P. Prelovšek. “Many-body localization in the Heisenberg XXZ magnet in a random field”. *Phys. Rev. B* 77 (6 2008), p. 064426 (cit. on pp. 18, 20).

[136] B. Bauer and C. Nayak. “Area laws in a many-body localized state and its implications for topological order”. *Journal of Statistical Mechanics: Theory and Experiment* 2013.09 (2013), P09005 (cit. on p. 18).

[137] M. Serbyn, Z. Papić, and D. A. Abanin. “Local Conservation Laws and the Structure of the Many-Body Localized States”. *Phys. Rev. Lett.* 111 (12 2013), p. 127201 (cit. on pp. 18, 19).

[138] J. A. Kjäll, J. H. Bardarson, and F. Pollmann. “Many-Body Localization in a Disordered Quantum Ising Chain”. *Phys. Rev. Lett.* 113 (10 2014), p. 107204 (cit. on pp. 18, 34).

[139] V. Khemani, S. P. Lim, D. N. Sheng, and D. A. Huse. “Critical Properties of the Many-Body Localization Transition”. *Phys. Rev. X* 7 (2 2017), p. 021013 (cit. on pp. 18, 24).

[140] D. N. Page. “Average entropy of a subsystem”. *Phys. Rev. Lett.* 71 (9 1993), pp. 1291–1294 (cit. on pp. 20, 123).

[141] H. Kim and D. A. Huse. “Ballistic Spreading of Entanglement in a Diffusive Nonintegrable System”. *Phys. Rev. Lett.* 111 (12 2013), p. 127205 (cit. on p. 20).

[142] M. Kiefer-Emmanouilidis, R. Unanyan, M. Fleischhauer, and J. Sirker. “Evidence for Unbounded Growth of the Number Entropy in Many-Body Localized Phases”. *Phys. Rev. Lett.* 124 (24 2020), p. 243601 (cit. on p. 20).

[143] T. Chanda, P. Sierant, and J. Zakrzewski. “Time dynamics with matrix product states: Many-body localization transition of large systems revisited”. *Phys. Rev. B* 101 (3 2020), p. 035148 (cit. on p. 21).

[144] U. Schollwöck. “The density-matrix renormalization group”. *Rev. Mod. Phys.* 77 (1 2005), pp. 259–315 (cit. on p. 21).

[145] U. Schollwöck. “The density-matrix renormalization group in the age of matrix product states”. *Annals of Physics* 326.1 (2011). January 2011 Special Issue, pp. 96–192 (cit. on p. 21).

[146] W. De Roeck and F. Huveneers. “Stability and instability towards delocalization in many-body localization systems”. *Phys. Rev. B* 95 (15 2017), p. 155129 (cit. on pp. 23, 79).

[147] A. Chandran, A. Pal, C. R. Laumann, and A. Scardicchio. “Many-body localization beyond eigenstates in all dimensions”. *Phys. Rev. B* 94 (14 2016), p. 144203 (cit. on p. 23).

[148] R. Singh, R. Moessner, and D. Roy. “Effect of long-range hopping and interactions on entanglement dynamics and many-body localization”. *Phys. Rev. B* 95 (9 2017), p. 094205 (cit. on pp. 23, 88).

[149] F. Arute et al. “Quantum supremacy using a programmable superconducting processor”. *Nature* 574 (7779 2019) (cit. on p. 23).

[150] Q. Guo, C. Chang, Z.-H. Sun, Z. Song, H. Li, Z. Wang, W. Ren, H. Dong, D. Zheng, Y.-R. Zhang, R. Mondaini, H. Fan, and H. Wang. “Observation of energy-resolved many-body localization”. *Nat. Phys.* 17 (2 2021), pp. 234–239 (cit. on p. 23).

[151] B. Chiaro et al. “Direct measurement of non-local interactions in the many-body localized phase”. *axXiv:1910.06024* (2019) (cit. on p. 23).

[152] L. Landau. “On the theory of phase transitions”. *Zh. Eksp. Teor. Fiz.* 7 (1937), pp. 19–32 (cit. on p. 24).

[153] S. Sachdev. “Quantum Phase Transitions”. *Handbook of Magnetism and Advanced Magnetic Materials*. American Cancer Society, 2007 (cit. on p. 24).

[154] M. Žnidarić, A. Scardicchio, and V. K. Varma. “Diffusive and Subdiffusive Spin Transport in the Ergodic Phase of a Many-Body Localizable System”. *Phys. Rev. Lett.* 117 (4 2016), p. 040601 (cit. on p. 24).

[155] R. B. Griffiths. “Nonanalytic Behavior Above the Critical Point in a Random Ising Ferromagnet”. *Phys. Rev. Lett.* 23 (1 1969), pp. 17–19 (cit. on pp. 25, 87).

[156] S. Gopalakrishnan, M. Müller, V. Khemani, M. Knap, E. Demler, and D. A. Huse. “Low-frequency conductivity in many-body localized systems”. *Phys. Rev. B* 92 (10 2015), p. 104202 (cit. on pp. 25, 96).

[157] N. Darkwah Oppong, G. Pasqualetti, O. Bettermann, P. Zechmann, M. Knap, I. Bloch, and S. Fölling. “Probing transport and slow relaxation in the mass-imbalanced Fermi-Hubbard model”. *arXiv:2011.12411* (2020) (cit. on p. 28).

[158] G. H. Wannier. “Dynamics of Band Electrons in Electric and Magnetic Fields”. *Rev. Mod. Phys.* 34 (4 1962), pp. 645–655 (cit. on pp. 28, 101).

[159] G. Semeghini, M. Landini, P. Castilho, S. Roy, G. Spagnolli, A. Trenkwalder, M. Fattori, M. Inguscio, and G. Modugno. “Measurement of the mobility edge for 3D Anderson localization”. *Nat. Phys.* 11.7 (2015), pp. 554–559 (cit. on p. 32).

[160] S. Das Sarma, A. Kobayashi, and R. E. Prange. “Proposed Experimental Realization of Anderson Localization in Random and Incommensurate Artificially Layered Systems”. *Phys. Rev. Lett.* 56 (12 1986), p. 1280 (cit. on p. 33).

[161] S. Das Sarma, S. He, and X. C. Xie. “Mobility Edge in a Model One-Dimensional Potential”. *Phys. Rev. Lett.* 61 (18 1988), p. 2144 (cit. on p. 33).

[162] S. Das Sarma, S. He, and X. C. Xie. “Localization, mobility edges, and metal-insulator transition in a class of one-dimensional slowly varying deterministic potentials”. *Phys. Rev. B* 41 (9 1990), p. 5544 (cit. on p. 33).

[163] D. J. Thouless. “Localization by a Potential with Slowly Varying Period”. *Phys. Rev. Lett.* 61 (18 1988), p. 2141 (cit. on p. 33).

[164] J. Biddle and S. Das Sarma. “Predicted Mobility Edges in One-Dimensional Incommensurate Optical Lattices: An Exactly Solvable Model of Anderson Localization”. *Phys. Rev. Lett.* 104 (7 2010), p. 070601 (cit. on p. 33).

[165] J. Biddle, D. J. Priour, B. Wang, and S. Das Sarma. “Localization in one-dimensional lattices with non-nearest-neighbor hopping: Generalized Anderson and Aubry-André models”. *Phys. Rev. B* 83 (7 2011), p. 075105 (cit. on p. 33).

[166] F. A. An, E. J. Meier, and B. Gadway. “Engineering a Flux-Dependent Mobility Edge in Disordered Zigzag Chains”. *Phys. Rev. X* 8 (3 2018), p. 031045 (cit. on p. 33).

[167] D. A. Huse, R. Nandkishore, V. Oganesyan, A. Pal, and S. L. Sondhi. “Localization-protected quantum order”. *Phys. Rev. B* 88 (1 2013), p. 014206 (cit. on p. 34).

[168] C. R. Laumann, A. Pal, and A. Scardicchio. “Many-Body Mobility Edge in a Mean-Field Quantum Spin Glass”. *Phys. Rev. Lett.* 113 (20 2014), p. 200405 (cit. on p. 34).

[169] S. Nag and A. Garg. “Many-body mobility edges in a one-dimensional system of interacting fermions”. *Phys. Rev. B* 96 (6 2017), p. 060203 (cit. on pp. 35, 85).

[170] R. Modak and S. Mukerjee. “Many-Body Localization in the Presence of a Single-Particle Mobility Edge”. *Phys. Rev. Lett.* 115 (23 2015), p. 230401 (cit. on pp. 35, 82, 84, 85, 88).

[171] X. Li, S. Ganeshan, J. H. Pixley, and S. Das Sarma. “Many-Body Localization and Quantum Nonergodicity in a Model with a Single-Particle Mobility Edge”. *Phys. Rev. Lett.* 115 (18 2015), p. 186601 (cit. on pp. 35, 85).

[172] X. Li, S. Ganeshan, J. H. Pixley, and S. Das Sarma. “Many-Body Localization and Quantum Nonergodicity in a Model with a Single-Particle Mobility Edge”. *Phys. Rev. Lett.* 115 (18 2015), p. 186601 (cit. on pp. 35, 80).

[173] X. Li, J. H. Pixley, D.-L. Deng, S. Ganeshan, and S. Das Sarma. “Quantum nonergodicity and fermion localization in a system with a single-particle mobility edge”. *Phys. Rev. B* 93 (18 2016), p. 184204 (cit. on pp. 35, 80, 81, 84).

[174] S. Vijay, J. Haah, and L. Fu. “Fracton topological order, generalized lattice gauge theory, and duality”. *Phys. Rev. B* 94 (23 2016), p. 235157 (cit. on p. 35).

[175] H. Ma, E. Lake, X. Chen, and M. Hermele. “Fracton topological order via coupled layers”. *Phys. Rev. B* 95 (24 2017), p. 245126 (cit. on p. 35).

[176] J. P. Garrahan. "Aspects of non-equilibrium in classical and quantum systems: Slow relaxation and glasses, dynamical large deviations, quantum non-ergodicity, and open quantum dynamics". *Physica A: Statistical Mechanics and its Applications* 504 (2018). Lecture Notes of the 14th International Summer School on Fundamental Problems in Statistical Physics, pp. 130–154 (cit. on p. 35).

[177] N. Pancotti, G. Giudice, J. I. Cirac, J. P. Garrahan, and M. C. Bañuls. "Quantum East Model: Localization, Nonthermal Eigenstates, and Slow Dynamics". *Phys. Rev. X* 10 (2 2020), p. 021051 (cit. on pp. 35, 127).

[178] E. J. Bergholtz and A. Karlhede. "Quantum Hall system in Tao-Thouless limit". *Phys. Rev. B* 77 (15 2008), p. 155308 (cit. on p. 36).

[179] E. J. Bergholtz, M. Nakamura, and J. Suorsa. "Effective spin chains for fractional quantum Hall states". *Physica E: Low-dimensional Systems and Nanostructures* 43.3 (2011). NanoPHYS 09, pp. 755–760 (cit. on p. 36).

[180] D. A. Abanin, W. De Roeck, W. W. Ho, and F. Huveneers. "Effective Hamiltonians, prethermalization, and slow energy absorption in periodically driven many-body systems". *Phys. Rev. B* 95 (1 2017), p. 014112 (cit. on pp. 36, 41, 120).

[181] D. Abanin, W. De Roeck, W. W. Ho, and F. Huveneers. "A rigorous theory of many-body prethermalization for periodically driven and closed quantum systems". *Communications in Mathematical Physics* 354 (2017), pp. 809–827 (cit. on pp. 36, 41).

[182] M. Serbyn, D. A. Abanin, and Z. Papić. "Quantum many-body scars and weak breaking of ergodicity". *arXiv:2011.09486* (2020) (cit. on pp. 38, 39).

[183] S. Choi, C. J. Turner, H. Pichler, W. W. Ho, A. A. Michailidis, Z. Papić, M. Serbyn, M. D. Lukin, and D. A. Abanin. "Emergent SU(2) Dynamics and Perfect Quantum Many-Body Scars". *Phys. Rev. Lett.* 122 (22 2019), p. 220603 (cit. on p. 39).

[184] R. Yao, T. Chanda, and J. Zakrzewski. "On Stark Many-body localization perturbed by harmonic potential". *arXiv:2103.11699* (2021) (cit. on p. 40).

[185] M. Eckstein, M. Kollar, and P. Werner. "Thermalization after an Interaction Quench in the Hubbard Model". *Phys. Rev. Lett.* 103 (5 2009), p. 056403 (cit. on p. 41).

[186] A. Rubio-Abadal, M. Ippoliti, S. Hollerith, D. Wei, J. Rui, S. L. Sondhi, V. Khemani, C. Gross, and I. Bloch. "Floquet Prethermalization in a Bose-Hubbard System". *Phys. Rev. X* 10 (2 2020), p. 021044 (cit. on p. 41).

[187] T. Rom. "Bosonische und fermionische Quantengase in dreidimensionalen optischen Gittern". PhD thesis. 2009 (cit. on pp. 45, 104).

[188] S. Braun. "Negative absolute temperature and the dynamics of quantum phase transitions". PhD thesis. 2014 (cit. on p. 45).

[189] J. P. Ronzheimer. “Non-equilibrium dynamics of ultracold atoms in optical lattices”. PhD thesis. 2014 (cit. on p. 45).

[190] T. G. Tiecke. “Properties of Potassium”. Appendix A of PhD thesis by Tobias Gerard Tiecke, University of Amsterdam, 2009. 2019 (cit. on p. 46).

[191] M. Lewenstein, A. Sanpera, and V. Ahufinger. *Ultracold Atoms in Optical Lattices - Simulating Quantum Many-Body Systems*. Oxford University Press, 2012 (cit. on p. 49).

[192] F. C. Zhang and T. M. Rice. “Effective Hamiltonian for the superconducting Cu oxides”. *Phys. Rev. B* 37 (7 1988), pp. 3759–3761 (cit. on p. 49).

[193] T. Loftus, C. A. Regal, C. Ticknor, J. L. Bohn, and D. S. Jin. “Resonant Control of Elastic Collisions in an Optically Trapped Fermi Gas of Atoms”. *Phys. Rev. Lett.* 88 (17 2002), p. 173201 (cit. on p. 50).

[194] U. Schneider, L. Hackermüller, J. P. Ronzheimer, S. Will, S. Braun, T. Best, I. Bloch, E. Demler, S. Mandt, D. Rasch, and A. Rosch. “Fermionic transport and out-of-equilibrium dynamics in a homogeneous Hubbard model with ultracold atoms”. *Nat. Phys.* 8.213 (2012) (cit. on p. 50).

[195] U. Schneider. “Interacting fermionic atoms in optical lattices - A quantum simulator for condensed matter physics”. PhD thesis. 2012 (cit. on pp. 51, 113, 114, 128).

[196] C.-H. Wu. “Strongly interacting quantum mixtures of ultracold atoms”. PhD thesis. Massachusetts Institute of Technolgy - Department of Physics, 2013 (cit. on p. 54).

[197] C. Skedrov, M. Menashes, G. Ness, A. Vainbaum, and Y. Sagi. “Absence of heating in a uniform Fermi gas created by periodic driving”. *arXiv:2102.09506* (2021) (cit. on p. 54).

[198] M. W. Zwierlein, Z. Hadzibabic, S. Gupta, and W. Ketterle. “Spectroscopic Insensitivity to Cold Collisions in a Two-State Mixture of Fermions”. *Phys. Rev. Lett.* 91 (25 2003), p. 250404 (cit. on p. 55).

[199] J. Sebby-Strabley, M. Anderlini, P. S. Jessen, and J. V. Porto. “Lattice of double wells for manipulating pairs of cold atoms”. *Phys. Rev. A* 73.033605 (2006) (cit. on p. 60).

[200] S. Fölling, S. Trotzky, P. Cheinet, M. Feld, R. Saers, A. Widera, T. Müller, and I. Bloch. “Direct observation of second-order atom tunnelling”. *Nature* 448 (2007), pp. 1029–1032 (cit. on p. 60).

[201] F. Görg. *Ultracold fermionic atoms in optical superlattices*. 2014 (cit. on p. 60).

[202] A. D. Ludlow, M. M. Boyd, J. Ye, E. Peik, and P. O. Schmidt. “Optical atomic clocks”. *Rev. Mod. Phys.* 87 (2 2015), pp. 637–701 (cit. on p. 61).

[203] A. J. Daley. “Quantum computing and quantum simulation with group-II atoms”. *Quantum Information Processing* 10 (865 2011) (cit. on p. 61).

[204] F. A. An, K. Padavić, E. J. Meier, S. Hegde, S. Ganeshan, J. H. Pixley, S. Vishveshwara, and B. Gadway. “Interactions and Mobility Edges: Observing the Generalized Aubry-André Model”. *Phys. Rev. Lett.* 126 (4 2021), p. 040603 (cit. on p. 71).

[205] F. Wegner. “Flow-equations for Hamiltonians”. *Annalen der Physik* 506.2 (1994), pp. 77–91 (cit. on p. 71).

[206] X. Li and S. Das Sarma. “Mobility edge and intermediate phase in one-dimensional incommensurate lattice potentials”. *Phys. Rev. B* 101 (6 2020), p. 064203 (cit. on p. 73).

[207] R. Nandkishore and A. C. Potter. “Marginal Anderson localization and many-body delocalization”. *Phys. Rev. B* 90 (19 2014), p. 195115 (cit. on p. 79).

[208] T. Kohlert, S. Scherg, X. Li, H. P. Lüschen, S. Das Sarma, I. Bloch, and M. Aidelsburger. “Observation of Many-Body Localization in a One-Dimensional System with a Single-Particle Mobility Edge”. *Phys. Rev. Lett.* 122 (17 2019), p. 170403 (cit. on p. 80).

[209] D.-L. Deng, S. Ganeshan, X. Li, R. Modak, S. Mukerjee, and J. H. Pixley. “Many-body localization in incommensurate models with a mobility edge”. *Annalen der Physik* 529.7 (2017), p. 1600399 (cit. on p. 80).

[210] Y.-T. Hsu, X. Li, D.-L. Deng, and S. Das Sarma. “Machine Learning Many-Body Localization: Search for the Elusive Nonergodic Metal”. *Phys. Rev. Lett.* 121 (24 2018), p. 245701 (cit. on p. 81).

[211] K. Hyatt, J. R. Garrison, A. C. Potter, and B. Bauer. “Many-body localization in the presence of a small bath”. *Phys. Rev. B* 95 (3 2017), p. 035132 (cit. on p. 81).

[212] M. Schecter, T. Iadecola, and S. Das Sarma. “Configuration-controlled many-body localization and the mobility emulsion”. *Phys. Rev. B* 98 (17 2018), p. 174201 (cit. on p. 81).

[213] R. Modak, S. Ghosh, and S. Mukerjee. “Criterion for the occurrence of many-body localization in the presence of a single-particle mobility edge”. *Phys. Rev. B* 97 (10 2018), p. 104204 (cit. on pp. 82, 84, 85, 88).

[214] M. F. Lapa, J. C. Y. Teo, and T. L. Hughes. “Interaction-enabled topological crystalline phases”. *Phys. Rev. B* 93 (11 2016), p. 115131 (cit. on p. 88).

[215] I. V. Gornyi, A. D. Mirlin, M. Müller, and D. G. Polyakov. “Absence of many-body localization in a continuum”. *Annalen der Physik* 529.7 (2017), p. 1600365 (cit. on p. 88).

[216] C. M. Soukoulis and E. N. Economou. “Localization in One-Dimensional Lattices in the Presence of Incommensurate Potentials”. *Phys. Rev. Lett.* 48 (15 1982), pp. 1043–1046 (cit. on p. 89).

[217] I. Mondragon-Shem, A. Pal, T. L. Hughes, and C. R. Laumann. "Many-body mobility edge due to symmetry-constrained dynamics and strong interactions". *Phys. Rev. B* 92 (6 2015), p. 064203 (cit. on p. 91).

[218] P. A. Lee and T. V. Ramakrishnan. "Disordered electronic systems". *Rev. Mod. Phys.* 57 (2 1985), pp. 287–337 (cit. on p. 96).

[219] F. Evers and A. D. Mirlin. "Anderson transitions". *Rev. Mod. Phys.* 80 (4 2008), pp. 1355–1417 (cit. on p. 96).

[220] R. Anderson, F. Wang, P. Xu, V. Venu, S. Trotzky, F. Chevy, and J. H. Thywissen. "Conductivity Spectrum of Ultracold Atoms in an Optical Lattice". *Phys. Rev. Lett.* 122 (15 2019), p. 153602 (cit. on p. 96).

[221] S. Xu, X. Li, Y.-T. Hsu, B. Swingle, and S. Das Sarma. "Butterfly effect in interacting Aubry-Andre model: Thermalization, slow scrambling, and many-body localization". *Phys. Rev. Research* 1 (3 2019), p. 032039 (cit. on p. 97).

[222] R. Vasseur, A. C. Potter, and S. A. Parameswaran. "Quantum Criticality of Hot Random Spin Chains". *Phys. Rev. Lett.* 114 (21 2015), p. 217201 (cit. on p. 97).

[223] I. V. Protopopov, W. W. Ho, and D. A. Abanin. "Effect of SU(2) symmetry on many-body localization and thermalization". *Phys. Rev. B* 96 (4 2017), p. 041122 (cit. on p. 97).

[224] I. V. Protopopov and D. A. Abanin. "Spin-mediated particle transport in the disordered Hubbard model". *Phys. Rev. B* 99 (11 2019), p. 115111 (cit. on p. 97).

[225] P. Prelovšek, O. S. Barišić, and M. Žnidarič. "Absence of full many-body localization in the disordered Hubbard chain". *Phys. Rev. B* 94 (24 2016), p. 241104 (cit. on p. 97).

[226] M. Kozarzewski, P. Prelovšek, and M. Mierzejewski. "Spin Subdiffusion in the Disordered Hubbard Chain". *Phys. Rev. Lett.* 120 (24 2018), p. 246602 (cit. on p. 97).

[227] T. Hartmann, F. Keck, H. J. Korsch, and S. Mossmann. "Dynamics of Bloch oscillations". *New Journal of Physics* 6 (2004), pp. 2–2 (cit. on p. 101).

[228] D. M. Meekhof, C. Monroe, B. E. King, W. M. Itano, and D. J. Wineland. "Generation of Nonclassical Motional States of a Trapped Atom". *Phys. Rev. Lett.* 76 (11 1996), pp. 1796–1799 (cit. on p. 103).

[229] M. Greiner, O. Mandel, T. W. Hänsch, and I. Bloch. "Collapse and revival of the matter wave field of a Bose-Einstein condensate". *Nature* 419 (6902 2002), pp. 51–54 (cit. on p. 103).

[230] M. A. Nichols, L. W. Cheuk, M. Okan, T. R. Hartke, E. Mendez, T. Senthil, E. Khatami, H. Zhang, and M. W. Zwierlein. "Spin transport in a Mott insulator of ultracold fermions". *Science* 363.6425 (2019), pp. 383–387 (cit. on p. 104).

[231] Q. Guo, C. Cheng, H. Li, S. Xu, P. Zhang, Z. Wang, C. Song, W. Liu, W. Ren, H. Dong, R. Mondaini, and H. Wang. "Stark many-body localization on a superconducting quantum processor". *arXiv:2011.13895* (2020) (cit. on p. 107).

[232] W. Morong, F. Liu, P. Becker, S. Collins, L. Feng, A. Kyprianidis, G. Pagano, T. Youo, A. V. Gorshkov, and C. Monroe. "Observation of Stark many-body localization without disorder". *arXiv:2102.07250* (2021) (cit. on p. 107).

[233] "Schrieffer–Wolff transformation for quantum many-body systems". *Annals of Physics* 326.10 (2011), pp. 2793–2826 (cit. on p. 108).

[234] T. Kohlert, S. Scherg, P. Sala, F. Pollmann, B. H. M., I. Bloch, and M. Aidelsburger. "Experimental realization of fragmented models in tilted Fermi-Hubbard chains". *arXiv:2106.15586* (2021) (cit. on pp. 111, 115, 126, 132, 140).

[235] U. Schneider, L. Hackermüller, S. Will, T. Best, I. Bloch, T. A. Costi, R. W. Helmes, D. Rasch, and A. Rosch. "Metallic and Insulating Phases of Repulsively Interacting Fermions in a 3D Optical Lattice". *Science* 322.5907 (2008), p. 1520 (cit. on p. 112).

[236] L. Hackermüller, U. Schneider, M. Moreno-Cardoner, T. Kitagawa, T. Best, S. Will, E. Demler, E. Altman, I. Bloch, and B. Paredes. "Anomalous Expansion of Attractively Interacting Fermionic Atoms in an Optical Lattice". *Science* 327.5973 (2010), pp. 1621–1624 (cit. on p. 112).

[237] J. Hauschild and F. Pollmann. "Efficient numerical simulations with Tensor Networks: Tensor Network Python (TeNPy)". *SciPost Phys. Lect. Notes* (2018). Code available from `https://github.com/tenpy/tenpy`, p. 5 (cit. on pp. 117, 139).

[238] T. Mori, T. Kuwahara, and K. Saito. "Rigorous Bound on Energy Absorption and Generic Relaxation in Periodically Driven Quantum Systems". *Phys. Rev. Lett.* 116 (12 2016), p. 120401 (cit. on p. 120).

[239] F. Meinert, M. J. Mark, E. Kirilov, K. Lauber, P. Weinmann, M. Gröbner, A. J. Daley, and H.-C. Nägerl. "Observation of many-body dynamics in long-range tunneling after a quantum quench". *Science* 344.6189 (2014), pp. 1259–1262 (cit. on p. 120).

[240] D. V. Else, W. W. Ho, and P. T. Dumitrescu. "Long-Lived Interacting Phases of Matter Protected by Multiple Time-Translation Symmetries in Quasiperiodically Driven Systems". *Phys. Rev. X* 10 (2 2020), p. 021032 (cit. on p. 126).

[241] B. H. M., S. Scherg, T. Kohlert, I. Bloch, and M. Aidelsburger. "Benchmarking a novel efficient numerical method for localized 1D Fermi-Hubbard systems on a quantum simulator". *arXiv:2105.06372* (2021) (cit. on pp. 128, 131, 132).

[242] J. Feldmeier, P. Sala, G. De Tomasi, F. Pollmann, and M. Knap. "Anomalous Diffusion in Dipole- and Higher-Moment-Conserving Systems". *Phys. Rev. Lett.* 125 (24 2020), p. 245303 (cit. on p. 134).

[243] A. Gromov, A. Lucas, and R. M. Nandkishore. “Fracton hydrodynamics”. *Phys. Rev. Research* 2 (3 2020), p. 033124 (cit. on p. 134).

[244] S. Moudgalya, B. A. Bernevig, and N. Regnault. “Quantum many-body scars in a Landau level on a thin torus”. *Phys. Rev. B* 102 (19 2020), p. 195150 (cit. on p. 134).

Danksagung

An dieser Stelle möchte ich die Gelegenheit ergreifen und jenen Personen danken, die in den letzten Jahren maßgeblich an der Entstehung dieser Arbeit ihren Anteil hatten. Besonderer Dank gilt natürlich Immanuel Bloch, der mir die Möglichkeit gab, in seiner Gruppe zu forschen und den Geheimnissen von Quanten-Vielteilchensystemen ein Stück näher auf den Grund zu gehen. Weiterhin erhielt ich die Gelegenheit, auf internationale Konferenzen zu reisen und Kollegen aus der wissenschaftlichen Community persönlich kennenzulernen. Dies sind Erfahrungen, die ich gerne in Erinnerung behalten werde. Gleichermaßen bin ich auch Monika Aidelsburger für ihre Betreuung zu Dank verpflichtet. Der stete wissenschaftliche Austausch hat sehr zum Fortschritt des Experiments und meines persönlichen Verständnisses beigetragen und die Publikationen aus dieser Doktorarbeit überhaupt ermöglicht.

Unter meinen direkten Kollegen im Team Fermi 1 muss ich zuallererst Sebastian Scherg für eine unglaublich kurzweilige, interesante und lehrreiche Zeit gemeinsam im Labor danken, wo wir uns, denke ich, hervorragend ergänzt und auch außerhalb des Labors toll verstanden haben. Zwar liefen seine erzieherischen Maßnahmen, mich zu Bier, Schnaps und Kaffee zu animieren, in der Regel ins Leere, aber ich habe dafür inzwischen eine gewisse Toleranz gegenüber Après-Ski-Musik entwickelt. Bharath Hebbe Mashusudhana hat unser Team im Herbst 2018 als Postdoc großartig ergänzt und durch sein herausragendes Physikverständnis unser Team sehr vorangebracht. Die Diskussionen mit ihm waren immer aufschlussreich und sein Zutun hat die Aufgaben stets viel einfacher gemacht. Zu Beginn meiner Promotion hatte ich das Glück, auch mit Pranjal Bordia, Michael Schreiber und Henrik Lüschen zusammenzuarbeiten, die mir viel über das Experiment und zugehörige Physik beigebracht haben. Es war mir stets eine große Freude, mit euch zu arbeiten!

Dass ich in der Gruppe eine sehr angenehme Zeit verleben durfte, liegt auch an den Kollegen aus den anderen Teams an der LMU (Fermi 2, Cäsium, Ytterbium, SQM), mit denen man nicht nur eine schöne Mittagspause und gelegentliche Abende mit Bier oder Waffeln verbringen konnte, sondern sie standen auch immer gerne mit fachlichem Rat oder dringend benötigtem Equipment zur Seite. Besonderer Dank geht hierbei an Christoph Braun, sowie die ehemaligen Doktoranden Karen Wintersperger und Jakob Näger, die mich in den Spaß des Boulderns eingeweiht haben. Danke auch an jene, die ihre kostbare Zeit geopfert haben, um meine Doktorarbeit zur Korrektur zu lesen: Sebastian Scherg, Bharath Hebbe Madhusudhana und Henrik Lüschen.

Auch hatte ich das Vergnügungen, in den Projekten mit hervorragenden Kollegen der theoretischen und numerischen Physik zu kollaborieren. Dazu zählen Sankar Das Sarma und Xiao Li von der University of Maryland und der University of Hong Kong, sowie Frank Pollmann und Pablo Sala von der Technischen Universität München. Die wissenschaftliche Zusammenarbeit war sehr harmonisch und lehrreich.

Hervorheben möchte ich auch Kristina Schuldt und Doreen Seidl für die reibungslose Abwicklung aller administrativen Pflichten. Ganz besonders bin ich Ildiko Kecskesi dankbar, die nicht nur jede verwaltungstechnische Frage in Windeseile klären konnte, sondern auch stets ein offenes Ohr für Themen jenseits des wissenschaftlichen Betriebs hatte. Darüber hinaus möchte ich auch Bodo Hecker erwähnen, der mir in seiner geduldigen Art elektronische Grundkenntnisse vermittelt hat, die wir gewinnbringend im Labor integrieren konnten.

Zu guter letzt will ich auch noch meinem persönlichen Umfeld danken. Dazu zähle ich treue, langjährige Freunde, ohne die die letzten Jahre so nicht möglich gewesen wären. In erster Linie bin ich aber meine Familie zu größtem Dank verpflichtet, da sie mich jederzeit bedingungslos unterstützt hat.